THESIS FOR THE DEGREE OF LICENTIATE OF PHILOSOPHY

Fission: impossible?

Search for fission of ^{230}Ac

MARIA VITTORIA MANAGLIA

Department of Physics
CHALMERS UNIVERSITY OF TECHNOLOGY
Gothenburg, Sweden 2025

Fission: impossible?
Search for fission of ^{230}Ac
Maria Vittoria Managlia

Department of Physics
Chalmers University of Technology
SE-412 96 Gothenburg
Sweden
Telephone +46 (0)31-7721000

Cover: An artistic interpretation by the author of the typical helical trajectories of charged particles in the uniform magnetic field of a solenoidal spectrometer.

Chalmers Reproservice
Gothenburg, Sweden 2025

Fission: impossible?
Search for fission of ^{230}Ac
MARIA VITTORIA MANAGLIA
Department of Physics
Chalmers University of Technology

Abstract

A novel and versatile approach for studying (d,pF) reactions using the ISOLDE Solenoidal Spectrometer (ISS) at CERN is presented. Specifically designed to maximize the detection efficiency for fission fragments in coincidence with a proton from a (d,pF) reaction within the 2 T magnetic field of the ISS, this setup will enable the precise extraction of fission probabilities of neutron-rich nuclei as a function of excitation energy. Furthermore, dedicated γ-ray measurements will provide additional insights into the total energy and multiplicity of γ-rays emitted during the fission process.

Extensive simulations are conducted to optimize the experimental setup, leading to significant improvements in the detection efficiency of fission fragments. A CD-shaped silicon detector is chosen to enhance the detection of the fragments that are strongly forward-peaked in the laboratory frame due to the kinematic boost in inverse kinematics. This design achieves a detection efficiency eight times higher than that of gas-filled fission fragment detectors used in a previous proof-of-principle experiment.

Additionally, the case is made for an innovative off-axis configuration for the beam luminosity monitor, contrary to the standard on-beam approach. This choice minimizes interference with fission fragment trajectories and, through the additional position information provided by the detector, significantly improves the signal-to-background ratio.

The compact and modular design of this experimental setup also facilitates the detection of γ-rays emitted from fission fragments, offering a comprehensive characterization of the fission process. These developments are driven by the upcoming experiment to investigate the fission of ^{230}Ac using a radioactive ^{229}Ac beam, marking the first such measurement for this isotope. Importantly, the versatility of this approach makes it adaptable for studying other isotopes of interest in future experiments.

Keywords: Radioactive Beams, Fission, r-process, Heavy Elements, Actinides, Inverse Kinematics, CERN, ISOLDE, ISS.

Acknowledgements

I want to express my deepest gratitude to my PhD supervisor, Andreas Heinz, for his invaluable guidance, continuous support, and encouragement throughout my research. His insights and expertise have played a crucial role in shaping this work. I am also grateful to my co-supervisor, Thomas Nilsson, and my examiner, Christian Forssén, for their thoughtful advice, constructive feedback, and the time they dedicated to reviewing my work, as well as for the help and time they provided to me during my PhD journey. A heartfelt thank you to Björn Jonson, who enriches our physics discussions with engaging anecdotes, personal stories, and his invaluable years of experience, making them even more enjoyable. I am sincerely grateful to Håkan T. Johansson for his detailed feedback on my thesis, his invaluable advice on software and data acquisition systems, and for broadening my perspective on problem-solving in ways I had never considered. His support and enthusiasm, often accompanied by Winston Churchill's aphorisms, have been a great source of motivation. A special thank you to Hans T. Törnqvist for being an exceptional office mate and for patiently answering my endless questions—whether they were about software, physics, music, movies, or anything in between. I also want to thank Anna Kawęcka—I am truly grateful to share this PhD journey with you. I would like to acknowledge the many students who contributed to this project, with particular appreciation for Björn Johansson. His dedication, hard work, and enthusiasm have been truly remarkable, and I greatly value his commitment throughout this journey. A huge thank you to Matthias Holl, who never hesitated to help whenever I needed it. I truly appreciate it. I am also deeply grateful to the ISS collaboration for their guidance and support in realizing this ambitious project, and to the local staff at CERN for their invaluable assistance.

To my friends—both those I met in the corridors of the physics department and beyond—you have made this experience even more meaningful, and I cherish the moments we have shared. A special thanks to my friends and family in Italy. Despite the distance, I have always felt your unwavering support, which has been invaluable throughout this journey.

Finally, more than anyone, I want to thank Lorenzo—for being the yin to my yang.

This research is supported by the Knut and Alice Wallenberg Foundation Dnr. KAW 2020.0076.

Contents

Chapter 1

Physics motivation

The rapid neutron capture process, or *r-process*, consists of nuclear reactions and decays that involve hundreds of different isotopes, some with completely unmeasured properties, as they have yet to be synthesized in the laboratory. During the r-process, neutrons are rapidly captured, leading to the formation of increasingly heavier nuclei. As these neutron-rich nuclei undergo β-decay, the increase in charge causes them to become more unstable and eventually more likely to undergo fission, splitting into two fragments. In Fig. 1.1 a schematic diagram illustrating the r-process is shown. Nuclear fission limits the mass and charge of nuclei that can be produced during the r-process. The resulting fission fragments may continue to capture neutrons until they either decay via β-decay or undergo further fission. This ongoing phenomenon, known as *fission recycling*, is not well understood and raises two important questions: at which point does the r-process path terminate, and how likely is it that neutron-rich nuclei, which are crucial for the r-process, will undergo fission? Investigating the fission barrier height of neutron-rich nuclei may provide insights into these questions.

Just to provide an example, Fig. 1.2 shows the fission barrier, i.e. the fission probability as a function of the excitation energy, for ^{239}U, obtained from an experiment conducted at Argonne National Laboratory (ANL). The main goal of the work presented in this thesis is to determine, in a similar manner, for the first time the fission barrier height of the neutron-rich ^{230}Ac nucleus.

Understanding the r-process and its connection to fission requires a broader perspective on how heavy elements are formed in the Universe. To grasp the significance of the r-process in this context, it's essential to first explore the origins of these elements and the processes that contribute to their creation.

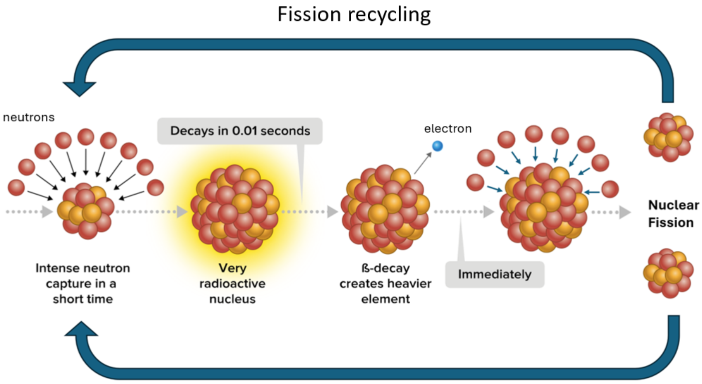

Figure 1.1: Schematic diagram illustrating the rapid neutron-capture process (r-process) and the subsequent fission recycling of the fission fragments. During the r-process, seed nuclei capture neutrons, moving through the neutron-rich region of the nuclear chart. Eventually, as unstable nuclei are produced they might undergo fission producing two fission fragments. These fragments can further capture neutrons, contributing to material recycling and continuing the r-process. This process is critical in synthesizing heavy elements beyond iron in explosive astrophysical environments such as neutron star mergers. Figure adapted from Ref. [1].

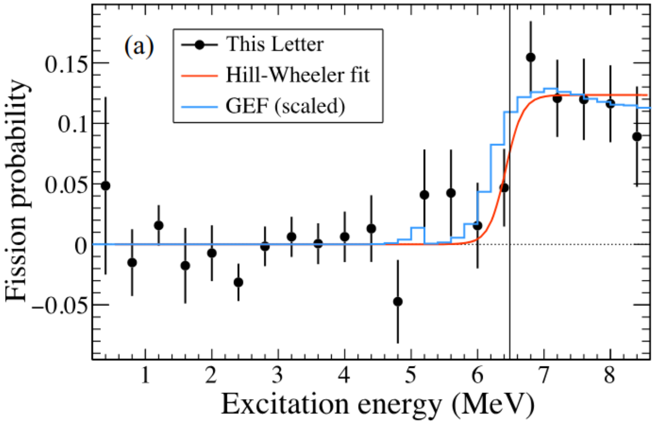

Figure 1.2: Experimental fission probability of ^{239}U compared with the GEF semi-empirical model calculation and an empirical Hill-Wheeler fit. The vertical line indicates the known fission barrier height. Figure adapted from Ref. [2].

1.1 The origins of the heaviest elements in the Universe

Throughout history, civilizations and cultures have been fascinated by the origin and nature of the Universe. Today, the most widely accepted theory explaining its beginning is the Big Bang theory, which argues that the Universe began expanding from a dense and hot state. In the initial moments following the Big Bang, after a brief period of rapid expansion known as *cosmic inflation*, the Universe existed in a state of matter known as *quark-gluon plasma.* In this extreme state, quarks and gluons, the fundamental particles later composing nucleons, were not confined to colorless states and could move freely rather than being bound within composite particles. It was only as the Universe cooled after this phase that neutrons and protons were formed. This period was characterized by a rapid expansion and cooling of the Universe, which facilitated the combination of quarks and gluons into these particles. As the Universe continued to cool, neutrons and protons combined to form nuclei of deuterium, an isotope of hydrogen. Some of these deuterium nuclei subsequently fused to form helium. Further nuclear reactions involving protons, neutrons, and various isotopes of helium led to the production of lithium. These primordial elements were not evenly spread throughout the Universe. Cooler regions of space exhibited clumpier distributions, with denser clouds of gas. As these clumps accumulated more mass, gravity began to attract additional matter. Growing denser and more compact, the cores of these clumps became hotter, reaching temperatures conducive to initiating nuclear fusion, and leading to the formation of the earliest stars. Simultaneously, these clumps merged into larger structures called proto-galaxies, which would evolve through further mergers and interactions into the galaxies we observe today.

Since then, the nuclear reactions in the life and death of stars have produced most of the elements of the Universe. Currently, around 3000 nuclides have been observed, of which only 288 are stable [3]. According to theoretical estimates, thousands of nuclides may still be undiscovered, many of which are extremely unstable and currently impossible to produce. Fig. 1.3 illustrates the periodic table of elements as we know it today and highlights the numerous processes involved in creating the elements found in the Solar System.

As discussed above, hydrogen, helium, and lithium originated from the Big Bang nucleosynthesis, whereas elements heavier than helium are created by means of nuclear reactions occurring in stars and stellar explosions in a process called *stellar nucleosynthesis.* The gravitational collapse acting on burnt-out stars releases a large amount of potential energy, heating the core of the star until it becomes hot enough for thermal energy to counterbalance gravity. High temperatures and pressures inside the stellar core enable the ignition of nuclear fusion of light elements. The fusion process begins with the fusion of hydrogen

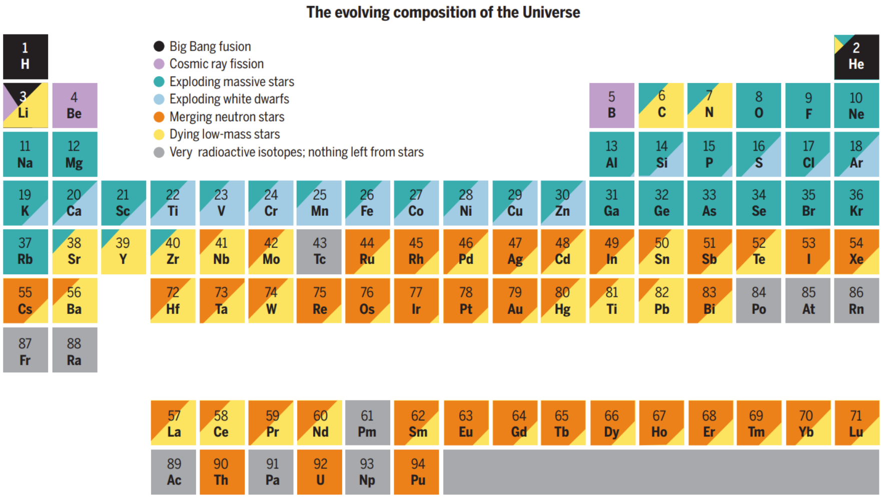

Figure 1.3: Color-coded periodic table illustrating the nucleosynthesis sources of elements in the Solar System. Figure from Ref. [4].

into helium[1]. As the star evolves and hydrogen in the core is exhausted, helium starts being fused into heavier elements like carbon and oxygen in processes such as the triple-α reaction[2]. In massive stars, further fusion stages can produce even heavier elements including neon, magnesium, and silicon, culminating in the formation of an iron core.

In order to understand why the fusion of silicon into iron marks the end of thermonuclear reactions within stars, it is useful to observe how the binding energy per nucleon evolves with the mass number A of nuclei. This quantity represents the average energy with which each nucleon is bound to the nucleus and as shown in Fig. 1.4 exhibits a first peak corresponding to the nucleus of helium (^{4}He) and an absolute maximum corresponding to nickel (^{62}Ni). This implies that the nucleons of ^{62}Ni are indeed the most strongly bound to each other, making ^{62}Ni the most stable nucleus. This has significant implications:

---

[1] The proton-proton (pp) chain and the CNO (Carbon-Nitrogen-Oxygen) cycle are two methods stars use to convert hydrogen into helium through nuclear fusion. The pp chain is prevalent in stars like the Sun with lower core temperatures, while the CNO cycle becomes more significant in hotter, more massive stars. Unlike the pp chain, which consumes all its constituents, the CNO cycle is a catalytic process where four protons fuse, with carbon, nitrogen, and oxygen isotopes acting as catalysts. Each isotope is consumed in one step but regenerated in another. The result is one stable helium nucleus (α), two positrons, and two electron neutrinos.

[2] The triple-α process is a nuclear reaction in which three α particles fuse to form ^{12}C, an essential step in the nucleosynthesis of heavier elements in stars. The reaction can be represented as follows: $3\,^4\mathrm{He} \rightarrow \,^{12}\mathrm{C} + \mathrm{energy}$.

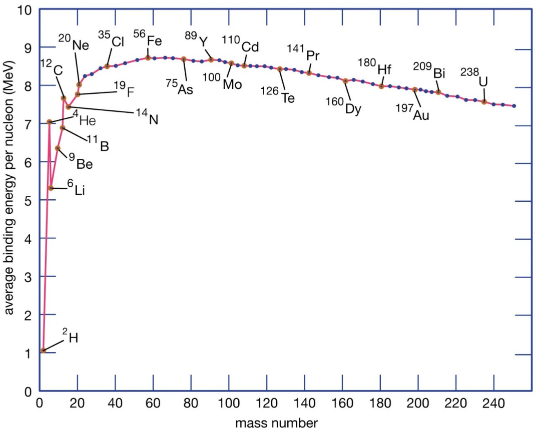

Figure 1.4: The average binding energy per nucleon as a function of the mass number. Figure from Ref. [5].

exoenergetic nuclear reactions involve fusion for nuclei lighter than ^{62}Ni and fission for heavier nuclei. However, ^{62}Ni is not populated in later-stage silicon burning. Instead, the ^{56}Fe peak represents the end point of elements formed through fusion in the cores of stars. Each fusion reaction up to ^{56}Fe produces more tightly bound nuclei, releasing binding energy that counteracts gravitational collapse and sustains the star.

Once a star exhausts its nuclear fuel, it can no longer generate enough fusion energy to counteract gravitational collapse. Consequently, the core starts to collapse, leading to a rapid increase in material density. Eventually, the nucleon-nucleon interaction causes the infalling material to bounce back and launch an expanding shock wave. In cases of very massive stars, this shock wave results in a violent explosion, normally referred to as *core-collapse supernovae.* Alongside other processes, these supernovae enrich the Universe with most of the material that makes up the Solar System. However, the origin of the heavier elements beyond iron and nickel, which are also present in the Solar System, still needs to be discussed.

Heavy elements

Already the first pioneers working on the formation of the elements in the Universe, in 1957, suggested that the vast majority of elements heavier than iron and nickel are created via neutron-capture and $\beta-$decay reactions [6, 7]. Since neutrons do not carry electric charge and are unaffected by the Coulomb repulsion, elements with a high neutron-to-proton ratio can form at significantly lower temperatures than those in stellar cores. However, due to the instability of free neutrons, which have a half-life of 10.2 minutes, their occurrence in nature is rare [8]. Hence, specific astrophysical sites within the Universe must exist where adequate fluxes of neutrons are available. Depending on the intensity of the neutron flux, we can distinguish between the slow neutron capture process, or *s-process*, and the rapid neutron capture process, also known as *r-process*. The s-process typically occurs in the late evolution stages of the AGB stars[3]. It involves neutron capture and β^- decay. Since the neutron flux in AGB stars is typically low, the rate of neutron capture is comparable to the timescale for β^- decay. Therefore, the nucleus has time to undergo β^- decay if it is unstable. Overall, the process is expected to last thousands of years, with decades often elapsing between subsequent neutron captures. In AGB stars, stellar winds, driven by the combined effects of radiation pressure and convection in the outer layers, lift material outward. The cooling of this ejected material allows dust grains to condense, which are then accelerated by radiation pressure, dragging surrounding gas and producing slow, dense winds. These winds strip the star of its outer layers, eventually forming a planetary nebula and leaving a white dwarf as the remnant, ensuring the distribution of the synthesized elements into the interstellar medium.

The s-process alone is however insufficient to explain the abundance of heavy elements found in the Solar System. For instance, in Figure 1.5, the element abundances found in CS 22892-052 (represented by black dots), an extremely metal-poor giant[4] with large relative enhancements of neutron capture elements located in the halo of the Milky Way galaxy, are compared to the abundance distributions predicted by the s- and r-processes (shown in red and blue lines, respectively). As can be seen, the s-process alone cannot account for the abundance of elements such as gold, platinum, thorium, and others. Therefore, these elements must originate from another process, the r-process, which occurs in the presence of a very high neutron flux. In this case the neutron flux is so intense that most nuclei do not have time to undergo β^- decay before another neutron is captured. The duration of the r-process is typically on the order of seconds to minutes. The paths of the r- and s-processes in the nuclear chart are presented in Fig. 1.6 and reflect the difference in the timescale of the two processes. Whereas the s-process is expected to proceed near the β-stability line, the r-process shifts significantly toward the neutron-rich region of the nuclear chart, where many nuclei are unknown. The sequence can extend up to the stability limits of these increasingly neutron-rich nuclei.

---

[3] Asymptotic Giant Branch (AGB) stars are a type of star that represents a late stage in the evolution of low to intermediate-mass stars, typically those with initial masses between about $0.6 - 10$ solar masses ($M_\odot$).

[4] A metal-poor star is a star with a relatively low abundance of elements heavier than helium, collectively referred to as "metals" in astrophysics. The metal content of a star is typically measured by its metallicity, denoted as [Fe/H], which represents the logarithmic ratio of iron (a proxy for overall metallicity) to hydrogen relative to the Sun. Metal-poor stars generally have [Fe/H] values significantly lower than 0 (the solar value), often below -1.

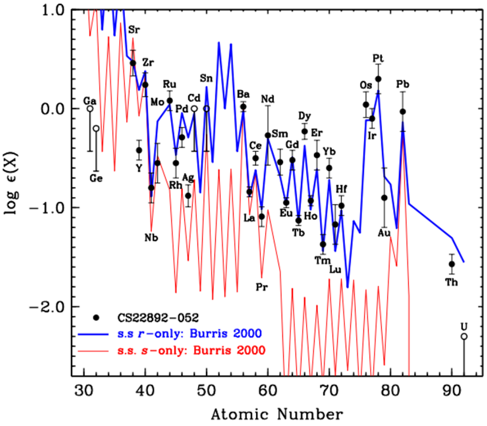

Figure 1.5: Comparison between element abundances in the metal-poor star CS 22892052 (black dots) and scaled Solar System abundance distribution for r-process only in blue and s-process only in red. Figure from Ref. [9].

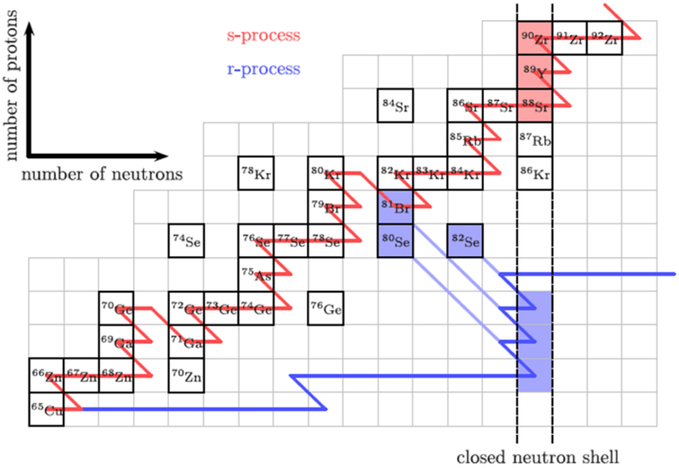

Figure 1.6: A section of the chart of nuclides showing a schematic representation of parts of the s- and r-processes path. Stable isotopes are marked and labeled. The s-process (in red) advances gradually through neutron capture, succeeded by $\beta-$decay. In contrast, the r-process (in blue) advances through numerous consecutive neutron captures, followed by a competition between $\beta-$decay and further neutron capture. Eventually, as the neutron flux diminishes, the unstable isotopes formed will decay through $\beta-$decays into stable isotopes (not depicted). Figure from Ref. [10].

Even though the underlying theory describing the r-process was worked out more than six decades ago, the exact kind of astrophysical site (or sites) where it takes place remained a mystery. Researchers had several hypotheses, such as core-collapse supernovae, neutron star mergers, and certain types of binary star systems, but definitive experimental evidence was lacking. A key piece of evidence would be the discovery of freshly synthesized r-process elements in an astrophysical site.

In 2015, the LIGO interferometers made the groundbreaking detection of gravitational waves from a black hole merger, marking the first direct observation of such waves [11]. Following this success, already in 2017, the LIGO and Virgo interferometers detected gravitational waves from an event, GW170817, which was later identified as a neutron-star merger. Following this detection, many telescopes on Earth were pointed toward the source, leading to the multi-messenger observation of the subsequent kilonova[5], named AT2017gfo. This confirmed signatures of radioactive heavy elements among which later the rapid neutron-capture element strontium ($Z = 38$) was identified [12]. The detection of a neutron-capture element associated with the collision of two extreme-density stars confirms the origin of r-process elements in neutron-star mergers.

1.2 Nuclear fission

Nuclear fission is a process where the nucleus of an atom splits into two or more smaller fragments, typically releasing energy. This phenomenon was first identified in 1938 through the crucial insights of Lise Meitner, with Otto Hahn and Fritz Strassmann also contributing to the discovery. It stands as one of the most dramatic examples of nuclear decay [13].

One of the first successful models describing the fission process was the *Liquid-Drop Model* (LDM), which was initially applied to fission by Lise Meitner. Niels Bohr and Archibald Wheeler later developed and detailed this description further [14]. According to the LDM, the atomic nucleus can be seen macroscopically as a charged liquid drop with the surface tension, caused by the strong nuclear force that holds the nucleus together providing the restoring force, and the Coulomb repulsion among protons driving the system toward fission. They imagined the nucleus driven by these vibrations and deforming through a series of increasingly elongated shapes. Based on these assumptions,

---

[5] A kilonova is a transient astronomical event that occurs when two neutron stars or a neutron star and a black hole merge. These mergers result in a powerful explosion that releases energy in the form of electromagnetic radiation and gravitational waves, typically in the order of a thousand times more energy than a typical nova, hence the prefix "*kilo-*". Kilonovae are characterized by rapidly fading optical and infrared emission over the course of days to weeks. They are believed to be significant sources of heavy elements like gold and platinum, as the extreme conditions of the merger facilitate the rapid production and dispersal of these elements into space.

Bohr and Wheeler calculated the potential energy of the vibrating nucleus as the sum contribution from the surface tension and the Coulomb repulsion. The result was the so-called *potential-energy surface* (PES) which illustrates the potential energy of the system in relation to its shape defined by two parameters: the elongation and the fission-fragment mass asymmetry. In practice, more parameters are needed, typically about 8. In Fig. 1.7 on the left the potential-energy surface for the ^{238}U nucleus is reported.

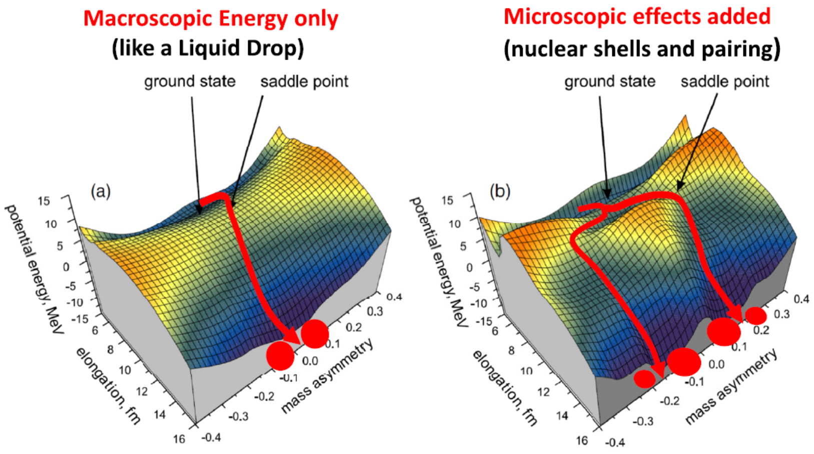

Figure 1.7: Potential-energy surface as a function of elongation and fission-fragment mass asymmetry of the ^{238}U nucleus according to the macroscopic liquid-drop (a) and the macroscopic-microscopic (b) models. The red lines with arrows depict the most likely fission paths, aligning with the lowest energy state of the nucleus. While the LDM approach limits fission to symmetric pathways along a singular 'symmetric' valley, the inclusion of microscopic shell effects gives rise to asymmetric fission valleys. Figure from Ref. [15].

During the fission process, the nucleus elongates along the line of zero mass asymmetry, initially increasing its potential energy. As the nucleus continues to elongate, it eventually reaches a critical point known as the *saddle point*, which represents a barrier that must be overcome for fission to occur. Following this, further elongation leads the nucleus to the *scission point*, where it splits into two fission fragments. The LDM has proven to be a valid model in qualitatively describing the process of fission and why it is an important decay mode of heavy nuclei. However, it fails to explain why it has been observed experimentally that fission of actinide nuclei predominantly results in the creation of two asymmetric fragments[6]. Following the acknowledgment of the quantum nature of the atomic nucleus and the evolution of the shell-model approach in

---

[6] Asymmetric fission refers to a type of nuclear fission in which the nucleus splits into

nuclear physics, a more realistic description of nuclear fission than provided by the LDM was needed. This became possible by combining the LDM with nuclear shell structure, the so-called *macroscopic-microscopic* model. To account for quantum effects arising from individual nucleons and their interactions, "microscopic" shell corrections are incorporated into the description of the fission process. This entails combining the macroscopic potential energy described by the liquid-drop model with the microscopic potential energy arising from shell effects:

$$V_{\text{total}} = V_{\text{macro}}(\text{LDM}) + V_{\text{micro}}(\text{Shells}). \tag{1.1}$$

The LDM suggests that the potential energy increases smoothly with the addition of particles to the nucleus, while quantum mechanics predicts irregular jumps. This discrepancy arises because, in a simplified view, nucleons occupy shells with energy gaps, analogous to electrons in atomic orbitals. Consequently, a "smoothed" energy for the nucleus based on the filling energy levels by the nucleons can be computed. The disparity between these energies constitutes a microscopic shell correction, which is added to the LDM potential energy to incorporate the influence of quantum shell effects. Formally this is achieved using the so-called Strutinsky method [16].

This naturally led to the appearance of asymmetric fission valleys, thus to the asymmetric fission-fragment mass distribution as can be seen on the right in Fig. 1.7. The new approach to calculating the potential energy results in a more complex potential-energy landscape which can differ significantly for nuclei since the microscopic shell effects vary as a function of the neutron and proton numbers. This leads to the emergence of multiple "fission valleys", each with its particular properties including more than one saddle point and the fission-fragment mass distributions.

The fission barrier

It is important to highlight the pivotal role of the excitation energy in the behavior of the fissioning nucleus. As the excitation energy increases, the influence of microscopic shell effects diminishes. This phenomenon leads to the disappearance of distinct valleys representing asymmetric fission pathways on the potential energy surface. Instead, the PES transitions to a smoother surface resembling the LDM. Consequently, the nucleus tends to favor symmetric fission, in agreement with the pure LDM. This emphasizes the necessity of investigating fission reactions across a range of excitation energies to fully understand their dynamics and outcomes.

As already mentioned, the fission process is blocked for most nuclei by the fission barrier. Fission becomes possible in two ways [17]. The first way is known

---

two fragments of significantly different masses. Unlike symmetric fission, where the resulting fragments are nearly equal in mass number, asymmetric fission produces one lighter and one heavier fragment.

as *spontaneous fission*, where the nucleus undergoes fission through quantum tunneling, starting from its ground state in a similar way to the quantum tunneling which leads to α-decay. For nuclei relevant to the r-process, tunneling is not expected to be dominant, because the time-scale for the r-process is shorter than the expected spontaneous fission half-lives. The other way is *induced fission* where an incident particle bombards a target nucleus forming a compound nucleus. This can be achieved using different reaction mechanisms among which there are neutron-induced fission, direct reactions, spallation/fragmentation, and complete fusion just to name a few. In the last case, the projectile fuses completely with the target nucleus resulting in a compound system often referred to as *compound nucleus* (CN). If the excitation energy of this nucleus is sufficiently high — exceeding the fission barrier — the CN is likely to undergo fission as one of the possible de-excitation mechanisms, often accompanied by the emission of neutrons[7]. Typically, stable (or long-lived) light projectiles such as electrons, protons, neutrons, or light ions can collide with a heavy target to produce a fissioning compound nucleus. The key aspect of this approach is that the formed compound nucleus ends up with relatively high excitation energy, well above the fission barrier because the Coulomb barrier between the colliding nuclei prevents the formation of a low-excited fissioning nucleus.

Fission barriers of neutron-rich nuclei are largely unknown, which makes it very hard to test model predictions. In the coming years, advancements in technology, through for example the project this thesis reports on, will enable the measurement of fission barriers for radioactive nuclei that were previously inaccessible. Simultaneously, an increasing amount of observational data from neutron-star mergers will be gathered. This enhanced understanding of the r-process, coupled with new observations, will provide a better foundation for our knowledge of the formation of the heaviest elements in the Universe.

1.3 Thesis outline

This licentiate thesis focuses on probing the fission barrier height of neutron-rich nuclei by measuring single-nucleon transfer (d,pF) reactions within a solenoidal-magnetic field. Chapter 2 introduces the experimental approach of studying the fission of neutron-rich nuclei in inverse kinematics using the solenoidal spectrometer method. Chapter 3 provides a detailed description of the experimental setup optimized for studying (d,pF) reactions within the solenoidal field. The motivation for choosing ^{230}Ac as the candidate nucleus for this study is explained in Chapter 4. Finally, Chapter 5 reports the simulation results for the proposed and accepted IS739 experiment, “Fission of ^{230}Ac”, to be performed at the ISOLDE Solenoidal Spectrometer (ISS) at CERN.

---

[7] If fission occurs without prior neutron emission it is called “first-chance” fission; if one neutron is emitted first, the process is referred to as “second-chance” fission, and so on [18].

Contributions of the author

The work presented in this thesis is part of a collaborative project, with contributions from other members of the group and the ISS collaboration. The project aims to measure the fission barrier height of short-lived isotopes by conducting experiments in inverse kinematics using solenoidal spectrometers, which differ significantly from conventional experiments in terms of kinematics and the experimental approach.

The author joined for this work had no prior experience with such experiments, and the first task undertaken by the author was to understand and derive the transfer reaction kinematics within a solenoidal magnetic field. The author collaborated closely with another PhD student within the group making it a learning experience for both the author and the entire group.

To gain familiarity with the ISOLDE facility environment, the author participated in several experiments (IS659 and IS690) at the ISOLDE Decay Station (IDS) and the Scattering Experiments Chamber (SEC). To gain expertise with the ISS setup, the author also took part in multiple ISS experiments (IS742, IS686, IS587, IS727, IS677, IS710), contributing to shifts, online and near-line data analysis, and preparation.

Building on this experience, the author contributed to the design of a novel experimental setup for studying transfer reactions in inverse kinematics inside solenoidal spectrometers. This design was based on extensive simulations of existing detectors and the exploration of optimization strategies for fission barrier measurements. The author demonstrated that a CD-shaped telescope configuration of silicon detectors was more promising for optimizing the detection efficiency of fission fragments compared to the gas-filled fission fragment detector used is previous experiments at ISS. Following suggestions from collaborators in the U.S. and locally, the author optimized the use of a single off-axis position-sensitive silicon detector as a luminosity monitor by considering a four-element configuration. The performance of this new configuration was simulated and compared with the on-beam luminosity detector currently used at ISS. The author carefully investigated the optimal placement of the new luminosity detector inside the solenoidal magnet, comparing simulated luminosity values with experimental data from previous studies. Simulating past experiments also served as a test for the simulation framework the author helped develop.

A key contribution of the author was the extensive use of the GEF model to evaluate several candidates for fission barrier measurements, ultimately identifying ^{230}Ac as the most suitable option for a first experiment. The author also performed GEF model calculations to estimate the expected fission barrier height of ^{230}Ac and assessed the reaction and beam rates necessary for a successful measurement. With the insight gained, the author played an active role in writing and preparing the $^{229}\mathrm{Ac(d, pF)}$ experiment proposal. Furthermore, the author contributed to optimizing and testing the digital acquisition readout for the $^{229}\mathrm{Ac(d, pF)}$ experiment. Finally, the author participated in a fusion-fission experiment at INFN Legnaro to broaden her experience.

Chapter 2

Probing fission of neutron-rich nuclei

As mentioned in Sec. 1.2, the fission barrier is the energy threshold at which fission becomes one of the possible decay channels. Experimentally, it can be probed by measuring the fission probability as a function of the excitation energy of the system.

In order to study isotopes as close as possible to the r-process path, the most direct approach would be to measure neutron-induced fission of neutron-rich target nuclei in the laboratory. However, this presents numerous experimental challenges, such as low detection efficiencies, low neutron fluxes, and target availability. Since the fission fragments are emitted in 4π, detectors must cover a large solid angle, making it difficult to capture a high fraction of the fragments, thereby reducing the overall detection efficiency. The available neutron beam fluxes are often insufficiently intense, which limits the reaction rates. Moreover, neutron-induced cross-section data for short-lived nuclei are difficult or impossible to measure directly, as this requires producing and manipulating short-lived radioactive targets.

These difficulties can be addressed by using the surrogate reaction technique, suggested by J. Cramer and H. Britt in the 1970s [19]. It consists of an innovative indirect approach that allows the production of a compound nucleus of interest via an alternative (surrogate) experimentally accessible reaction. Typically, the surrogate reaction is selected such that the resulting nucleus has the same mass A and charge Z as the compound nucleus that would result from the desired neutron-induced reaction. The neutron-induced cross section of a nucleus X, $\sigma_{n,i}^{X}$ for the decay channel i can be factorized as:

$$\sigma_{n,i}^{A}(E_n) = \sigma_{\mathrm{CN}}^{\mathrm{cal}}(E_n) \cdot P_i^{\mathrm{exp}}(E_n) \tag{2.1}$$

where P_i^{exp} is the measured decay probability and $\sigma_{\mathrm{CN}}^{\mathrm{cal}}$ is the compound nucleus

(CN) formation cross section for the neutron-induced reaction obtained from optical model calculations.

While surrogate reactions provide valuable insights, it is essential to carefully interpret the results and consider potential differences between the surrogate reaction and actual r-process conditions. This indirect method has recently been adopted for studying various actinide targets, driven by advancements in experimental techniques and the growing interest in nuclei relevant to the r-process [20].

2.1 Inverse kinematics for studying (d,p) reactions

In reaction studies, normally, the straightforward technique is to perform the experiment in *direct kinematics*. This method involves a stable (or long-lived) light projectile incident on heavy target nuclei. However, a change in approach is needed when studying highly unstable neutron-rich nuclei because, for most radioactive isotopes, the half-life is too short to manufacture targets or to use them in an experiment. Therefore, an *inverse kinematics* approach is preferred: short-lived neutron-rich nuclei of interest are used as a beam, directed at a stable light target, such as deuterium.

The (d, p) surrogate reaction is an efficient way to mimic neutron capture which can induce fission as it occurs in the r-process. Here, the neutron transfer from a deuteron to the beam nucleus acts as a proxy for the neutron-induced reaction. As the radioactive nuclei in the beam collide with the deuterium target, the neutron from the deuteron can be transferred to the radioactive nucleus, while the proton is ejected, as shown in Fig. 2.1. If the (d, p) reaction

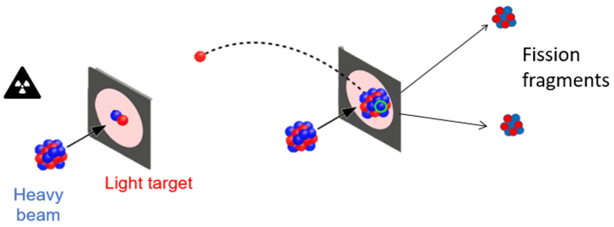

Figure 2.1: Schematic illustration of the (d, p) reaction in inverse kinematics: a radioactive heavy nucleus beam collides with a deuterium target, resulting in neutron (in blue) transfer to the heavy nucleus and the emission of a proton (in red). This process can lead to the fission of the resulting nucleus, emitting two fission fragments in the forward direction.

populates a state at excitation energy above the fission barrier, fission becomes a possible exit channel.

As a result of the reaction, two fission fragments, along with neutrons and possibly γ-rays, are produced and experience a large kinematic boost due to the inverse kinematics of the reaction. Consequently, the fission fragments move in the forward direction with an opening angle depending on the beam energy and the transverse momentum given to the fission fragments, making their detection less challenging[1]. The choice of using deuterium as a target instead of a pure neutron target is based on the inherent challenges and impracticalities associated with handling neutrons. Neutrons are electrically neutral, making them difficult to produce, direct, and confine as a dense, stable target. They cannot be easily manipulated using electromagnetic fields, and forming a concentrated neutron target is nearly impossible due to their lack of charge and short half-life (10.18 min [8]). Conversely, deuterium, composed of one proton and one neutron, is a stable and readily available isotope of hydrogen.

A broad range of beams for fission measurements in inverse kinematics for extensive isotopic chains of pre-actinide beams are available at the ISOL-type radioactive-ion-beam facility ISOLDE at CERN.

2.2 The ISOLDE facility at CERN

The Isotope Separator On-Line DEvice (ISOLDE) facility at CERN (the European Organization for Nuclear Research) in Geneva is a facility dedicated to producing radioactive isotopes [21]. In general, radioactive nuclei produced using the Isotope Separation On-Line (ISOL) method are initially stopped in the production target. After extraction, they are ionized and, for these experiments, then injected into a post-accelerator, where they are accelerated to the final energy.

At ISOLDE, over 1000 isotopes spanning 74 elements (with $Z = 2$ to 89), with half-lives down to milliseconds, have been synthesized at intensities reaching up to 10^{11} atoms per proton pulse [22]. This wide array of isotopes enables a systematic exploration into the atomic and nuclear properties of nuclei significantly deviating from the line of β-stability. The ISOLDE facility has proven to be a fertile environment for research in various fields, including nuclear physics, astrophysics, weak-interaction physics, solid-state physics, and biomedical studies.

---

[1] In direct kinematics, beam-like reaction products are commonly observed, whereas measuring target-like reaction products proves challenging. This difficulty arises because target-like products are often produced with insufficient kinetic energy to escape the target material.

2.2.1 Beam production

What makes CERN truly unique is its accelerator complex shown in Fig. 2.2. It consists of a series of interconnected accelerators used to accelerate and collide particles at high energies for various particle and nuclear physics experiments. In our case, the accelerating process starts in the Linear accelerator 4 (Linac4) where negative hydrogen ions H^- are extracted from a bottle of hydrogen gas and are accelerated to 160 MeV. A stripping foil is used to remove the two electrons from the ions when they are injected from Linac4 into the Proton Synchrotron Booster (PSB), leaving only protons. In the PSB, protons are accelerated to 1.4 GeV before being delivered to ISOLDE which is located nearby. Here, the protons are directed onto a target material, often made of a heavy element like uranium or thorium, with an intensity of up to 2 μA. Nuclear reactions induced by these highly energetic protons, such as fission, spallation, and fragmentation, yield numerous radionuclides across the nuclide chart.

The target material is contained in a tubular tantalum oven, which can be heated to temperatures of typically 2000 °C through resistive heating. This, combined with the porosity of the targets, facilitates the diffusion and extraction of the produced nuclei. As a result, short-lived isotopes can quickly reach the

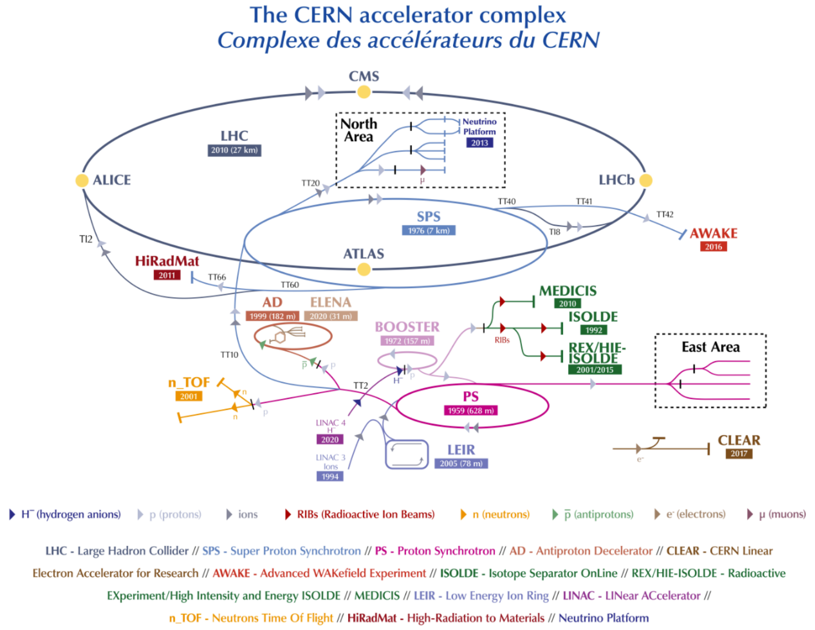

Figure 2.2: Layout of the CERN accelerator complex. Figure from Ref. [23].

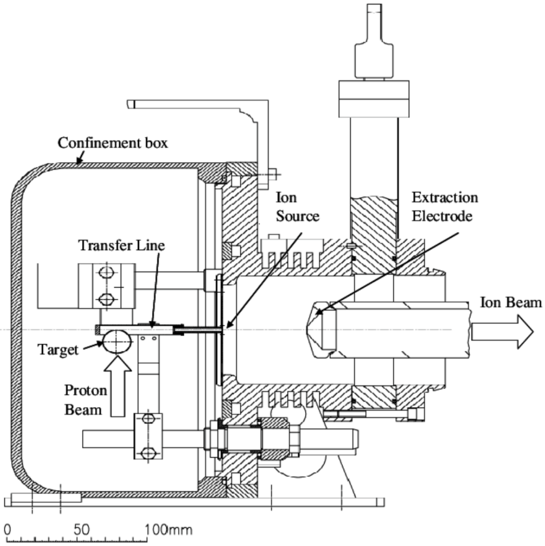

Figure 2.3: Schematic layout of the standard target-ion source unit at ISOLDE. The unit includes a tubular tantalum oven where the target material is resistively heated to facilitate the diffusion and extraction of short-lived isotopes. The proton beam irradiates the target, producing isotopes that diffuse toward the transfer line, which directs them to the ion source. Surface ionization occurs on a hot, high-work-function surface, such as rhenium or tantalum, creating positively charged ions. These ions are then extracted by electrodes for further processing. Figure from Ref. [24].

transfer line and the ion source, where they are singly ionized.

Typically at ISOLDE, atoms are positively ionized using the surface ionization technique, where the released atoms come into contact with a hot surface made of a material with a high work function[2], such as rhenium (Re) or tantalum (Ta). Upon contact with the hot surface, these atoms lose electrons and become positively charged ions. A schematic layout of the standard target-ion source unit used at ISOLDE is shown in Fig. 2.3. However, depending on the specific requirements of the experiments, the ionization process can also be performed by the Resonance Ionization Laser Ion Source (RILIS), which uses laser ablation to selectively ionize specific isotopes from the atomic vapor generated by heating the target material. This technique allows for high-purity ion beams of specific isotopes, essential for precision experiments. Another ion source

---

[2] The work function of a material is conventionally defined as the minimum energy required to extract one electron from its surface. Materials with a high work function require more energy to release electrons from their surface. Consequently, they are less likely to donate electrons to other materials and more likely to accept electrons from other materials. This characteristic makes them effective for surface ionization.

adopted at ISOLDE is the Electron Cyclotron Resonance Ion Source (ECRIS). This plasma ion source is ideal for producing highly charged ions. The plasma is generated from a gas mixture, typically argon (Ar) and xenon (Xe), which is ionized by electrons. These electrons are accelerated between the transfer line and the extraction electrode using an anode voltage of about 130 V. To optimize this ionization process, the electrons are confined within a magnetic field and are heated by microwave radiation. The microwaves resonate with the cyclotron frequency of the electrons, efficiently increasing their energy and enhancing their ability to ionize the gas atoms.

Once atoms are ionized, they are re-accelerated by a $30 - 60$ kV static electric potential. Subsequently, these ionized atoms are separated according to their mass-to-charge ratio in one of the two ISOLDE on-line isotope separator dipole magnets, each equipped with independent target-ion source systems. The first separator, known as the General Purpose Separator (GPS), includes one bending magnet and an electrostatic switchyard that enables the simultaneous extraction of three mass-separated beams. It achieves a mass resolving power of approximately 2400[3]. The second separator is the High-Resolution Separator (HRS), which consists of two bending magnets with an elaborate ion-optical system for higher-order corrections. Its mass resolving power exceeds 5000-7000 [25]. Furthermore, an off-line mass separator is available for tests and calibrations. Both separators are connected to a common beam line system to reach various experimental setups. One intermediate destination is REX-TRAP and REX EBIS, which feed the low-energy (up to 3 MeV/u) REX-ISOLDE beam line or, after charge breeding, the superconducting HIE-ISOLDE (High Intensity and Energy ISOLDE) post accelerator. As anticipated, this setup will eventually enable experiments with ions reaching kinetic energies up to 10 MeV/u [26]. The present limit is 8.38 MeV/u with $A/q = 4$ as achieved in the experiment IS708 in November 2024 [27] .

REX-ISOLDE

After mass separation, the resulting beam requires a series of refinements: cooling, bunching, and charge-breeding, essential for an efficient subsequent post-acceleration.

The $30 - 60$ keV ion beam from ISOLDE is slowed down and continuously injected into the REXTRAP Penning trap. The ions are trapped by a pulsed electrostatic potential alongside a static solenoidal magnetic field. At the same time, the ions are cooled via energy dissipation collisions with a buffer gas, typically Ar or Ne, in the next stage. After a fixed time, which is determined

---

[3] The mass resolving power of a mass separator refers to the ability to separate ions of different masses based on their mass-to-charge ratio. This quantity is defined as $R = \frac{m}{\Delta m}$ where m is the mass of the ion of interest and Δm is the smallest difference in mass that the separator can resolve.

by the required charge breeding time, the stopping electric potential at the exit side of the trap is rapidly lowered and the ion bunch is extracted from the trap. The ions therefore escape the trap in a bunch, with a temporal width of approximately 10 μs to 50 μs per bunch [28]. The ions are accelerated to 60 keV for transport. Before injection into the REX-EBIS (Electron Beam Ion Source), the ions are once again slowed down, or “retarded”, to ground potential. This step ensures that the ions are at the appropriate low kinetic energy for effective manipulation within the EBIS, where 1+ ions are bred to a higher charge state to make subsequent acceleration more efficient. The working operation of REX-EBIS is very similar to the REXTRAP with the difference that in place of the buffer gas, the interaction of ions is done with an electron beam operating in an Ultra High Vacuum (UHV) of at least 10^{-11} mbar. The electron gun delivers a high-intensity beam of highly energetic electrons impinging onto the trapped ions which strips away atomic electrons from the trapped ions. The extracted ions then pass through a mass separator which selects the desired A/q, and have thus entered the linear REX-ISOLDE accelerator [29].

The acceleration of charge-bred ions occurs in steps. First, a Radio Frequency Quadrupole (RFQ) accelerates the beam to 0.3 MeV/u and focuses it using quadrupole electric fields. Next, a buncher re-bunches the beam to help it enter the third component, which is the Interdigital H-type Structure (IHS). The IHS performs acceleration via RF fields parallel and anti-parallel to the beam axis. This drift-tube LINAC accelerates the beam to 1.2 MeV/u in 1.5 m at the same frequency. Finally, 7− and 9−gap cavities are used to accelerate the beam up to 2.2 MeV/u and 3 MeV/u, respectively.

HIE-ISOLDE

HIE-ISOLDE, a new linear accelerator at the ISOLDE facility, represents a significant energy upgrade. Beginning construction in 2015, it initially achieved beam acceleration to 4.5 MeV/u by 2016 and subsequently reached nearly 10 MeV/u upon its completion in 2018. The accelerator features four superconducting cryomodules, each operating at 4.5 K and measuring 2.3 meters in length [30]. These high-energy cryomodules house five superconducting cavities for acceleration and a superconducting solenoid for beam focusing [26]. This design ensures a minimum beam energy of 9.2 MeV/u for $2.5 \leq A/q \leq 4.5$ and allows beams with $A/q = 4$ to achieve 10 MeV/u [31]. For the case presented in this thesis, a charge state of around 52+ is expected for ^{229}Ac, leading to a $A/q \sim 4.5$, based on the best performances of EBIS charge breeding for radioactive actinide beams [32].

HIE-ISOLDE beams are sent to three experimental stations as depicted in Fig. 2.4: an array of high purity germanium detectors known as Miniball, the ISOLDE Solenoid Spectrometer, which uses a former MRI magnet and a third beamline where a large vacuum chamber is used for scattering experiments.

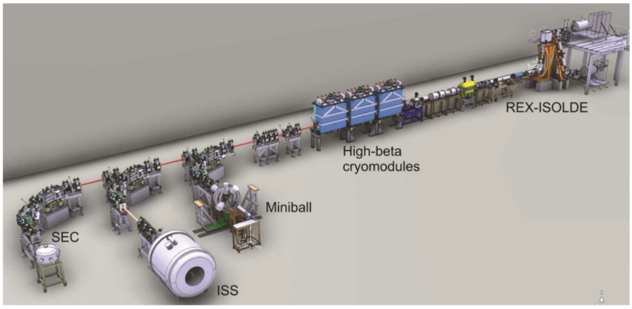

Figure 2.4: Layout of the HIE-linac as it appeared in 2016. On the right, the REX-ISOLDE postaccelerator is visible. Downstream of REX, two high-beta cryomodules are installed and connected to the high-energy beam transport system. The three operational beam lines are linked to Miniball (right), ISS (middle) and SEC (Scattering Experiments Chamber, left). Figure from Ref. [33].

2.3 The solenoidal spectrometer method

In the case of a direct (d,p) transfer reaction, the neutron from the deuteron is transferred to a single-particle state, and the ejected protons emerge with a well-defined kinetic energy determined by the kinematics and the Q-value of the reaction, allowing a direct probe of these states.

While transfer reactions in direct and inverse kinematics are indistinguishable in the center of mass frame, they differ significantly in the laboratory frame. The use of inverse kinematics allows to overcome experimental challenges in studying short-lived isotopes, but its associated kinematics limits the achievable energy resolution in a detector with a given acceptance of laboratory angles. The so-called *kinematic shift* refers to the variation of the ejected proton energy lines, corresponding to different excited states, with the emission angle in the laboratory system, as shown in red in Fig. 2.5. In inverse kinematics, the velocity of the CN is much larger than the corresponding reaction in normal kinematics, resulting in a greater kinematic shift and a worse resolution. Moreover, when considering forward center-of-mass angles, which are typically characterized by higher yields, a *kinematic compression* of the different energy lines is clearly visible.

The combination of these kinematic effects and energy measurements at fixed angles results in limited energy resolution. This is especially pronounced in reactions involving heavy beams, where the resolution can be on the order of several hundred keV [35]. Consequently, resolving individual excited states becomes difficult.

This deterioration of the energy resolution can be mitigated by the use of a solenoidal spectrometer as suggested in Refs. [36–38]. A schematic diagram of a

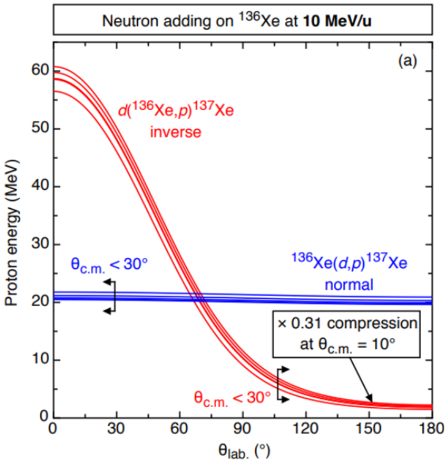

Figure 2.5: Kinematic lines of proton energy versus scattering angle $\theta_{\mathbf{lab}}$ in the laboratory frame for the $d(^{136}\mathrm{Xe}, p)$ reaction at 10 MeV/u following population of several excited states in ^{137}Xe in both normal (blue) and inverse (red) kinematics. Figure from Ref. [34].

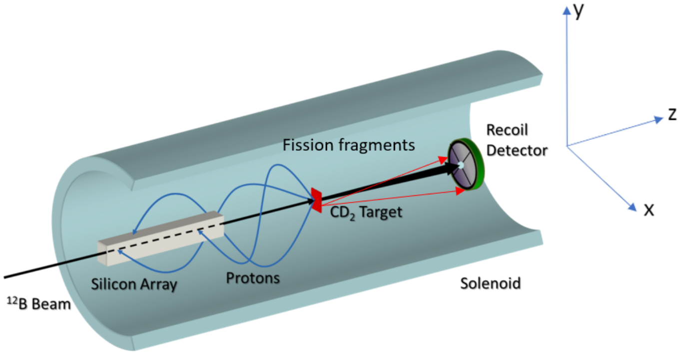

Figure 2.6: Schematic picture of a solenoidal spectrometer. The accelerated beam entering from the left in the superconducting solenoid, the position sensitive silicon detector array in the upstream direction, three typical helical proton trajectories and a recoil after a reaction in the target are indicated. Figure from Ref. [34].

solenoidal spectrometer is illustrated in Fig. 2.6. The idea is that the reaction is performed in the uniform magnetic field of a solenoidal superconducting magnet. The magnetic field is aligned along the beam direction (z coordinate in the laboratory system) causing any ejected charged particle to follow a helical orbit determined by the combination of its perpendicular and parallel momentum components relative to the magnet axis. The parallel momentum component is crucial for transporting the particle either upstream or downstream. The spiraling orbit will eventually intersect the beam axis again at a position z from the target, after a time equal to the cyclotron period T_{cyc} given by:

$$T_{\text{cyc}} = \frac{2m\pi}{Bq} \tag{2.2}$$

where B is the magnetic field, m is the mass of the particle, and q is its charge. The device is therefore dispersive along the axis in terms of the parallel velocity component. Specifically, events populating the same excited state but with different ejectile emission angles will exhibit varying longitudinal velocity components. Consequently, they will return to the axis at different positions z, as illustrated in Fig. 2.7.

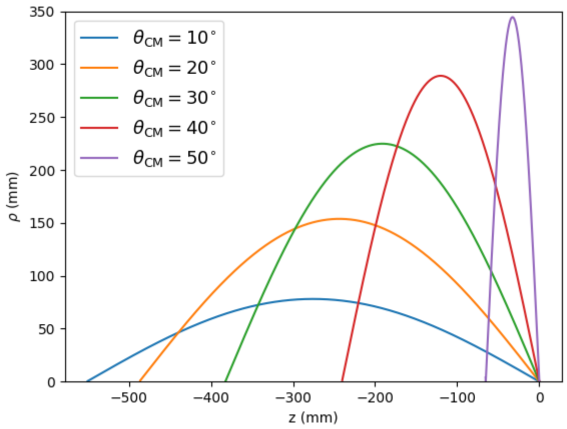

Figure 2.7: Radii ρ of proton trajectories as functions of z for the reaction ^{28}Si(d, p)^{29}Si at 6 MeV/u for various emission angles in the CM. The excitation energy of the compound nucleus is 2 MeV.

Due to particles being detected at a fixed distance from the target rather than at a fixed laboratory angle, the effective excitation energy resolution achievable with the solenoid can be significantly improved compared to a conventional array. By employing a hollow, position-sensitive array of silicon detectors, surrounding the beam axis, it becomes possible to measure both the position of intersect z and the laboratory energy of the particle E_{lab}.

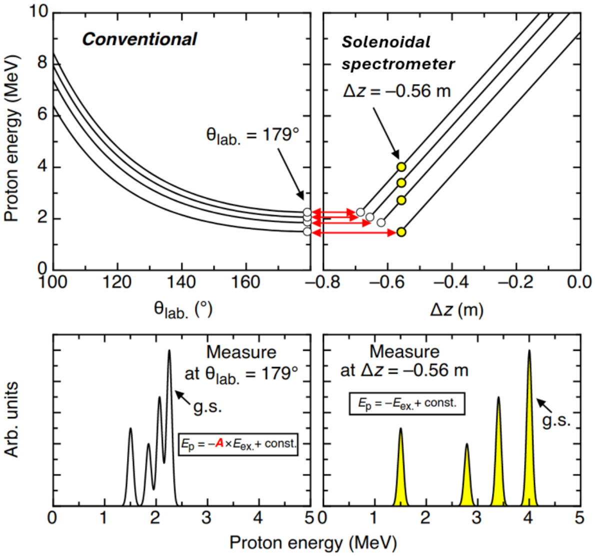

Figure 2.8: Illustration of how a solenoidal field translates kinematic curves from energy versus θ_{lab} into energy versus z for the positive Q-value reaction d(^{136}Xe, p) at 10 MeV/u and 2 T (left). The bottom panels depict corresponding projections of the Q-value for fixed θ_{lab} and z. A notable feature is the absence of kinematic compression when using the solenoidal technique. Figure from Ref. [34].

The equation which embodies the operational concept of the solenoidal spectrometer is:

$$E_{\mathrm{lab}} = E_{\mathrm{CM}} - \frac{mV_{\mathrm{CM}}^2}{2} + \frac{mzV_{\mathrm{CM}}}{T_{\mathrm{cyc}}} \tag{2.3}$$

where V_{CM} is the velocity of the center of mass. The linear relationship between the energy in the CM (E_{CM}) and z (presented in the upper right panel of Fig. 2.8) effectively eliminates the effects of the kinematic compression and shift. Indeed, when detected along the solenoid axis, the difference in energy between particles leaving the residual nucleus from different excited states is equal to the difference between the excitation energies of the states. This feature implies that the effective resolution achieved using a solenoid is significantly better than that of a conventional array. In a conventional setup, particles are detected at fixed laboratory angles, where the accuracy is limited by the beam spot size. With a solenoid, instead, the hit position along the z-axis can be determined with much greater precision. The peaks corresponding to different excited states are now separated by an energy difference equal to the separation in excitation energy, in contrast to the spectrum shown in the bottom right panel in Fig. 2.8. This method also eliminates a large class of potential background processes since only particles with the appropriate magnetic rigidity are transported from the target to the detector.

So far three solenoidal spectrometers have been developed: HELIOS at ANL[4], ISS at CERN, and SOLARIS at FRIB[5]. Even though they all share a similar approach, they are designed to receive different types of beams, making their individual scientific programs unique.

2.3.1 Inverse problem

A solenoidal spectrometer typically provides information about the z coordinate and the deposited energy E of the detected particles, while the cyclotron frequency provides a quantised observable that can suppress ejectiles with unwanted A/q ratios. The primary goal is to extract, from the first two of these measured quantities the excitation energy E_x of the compound nucleus formed in the reaction and the center-of-mass emission angle θ_{cm} of the ejected proton, using a mapping such as:

$$\begin{pmatrix} E \\ z \end{pmatrix} \longrightarrow \begin{pmatrix} E_x \\ \theta_{\mathrm{cm}} \end{pmatrix}. \tag{2.4}$$

In other words, quantities in the laboratory frame need to be transformed into the CM frame. Assuming a 2-body scattering, Fig. 2.9 illustrates the kinematics differences for the same process when viewed in the laboratory frame compared

---

[4] Argonne National Laboratory, Chicago, Illinois.

[5] Facility for Rare Isotope Beams, East Lansing, Michigan.

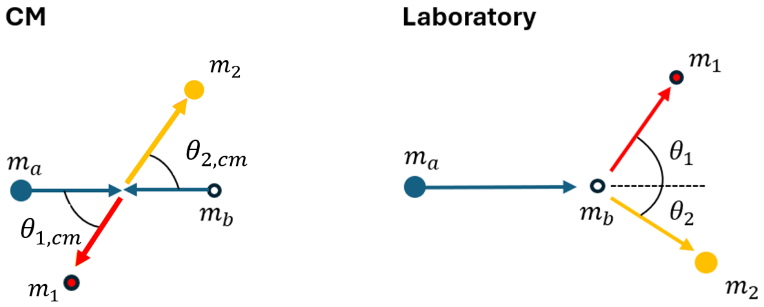

Figure 2.9: Two-body scattering processes as viewed in the laboratory (left) and center-of-mass (right) reference frames. The reacting partners are denoted by **a** and **b**, while **1** and **2** represent the reaction products.

to the CM frame, respectively. In the case of interest, **a** and **b** denote the reacting partners, namely the incoming radioactive heavy ion and the deuterium target. Following the scattering event, the ejected proton, referred to as ejectile **1**, and the recoiling nucleus **2**, emerge.

The measured energy E and the z-coordinate of the detected particles can be expressed as a function of E_x and θ_{cm}[39]:

$$\begin{aligned} E = {} & \frac{\gamma}{2E_t}(M_c^2 + m_1^2 - (m_2 + E_x)^2 \\ & - \beta \cos\theta_{\mathrm{cm}} \sqrt{\left(M_c^2 - (m_1 + m_2 + E_x)^2\right)\left(M_c^2 - (m_1 - m_2 - E_x)^2\right)} \end{aligned} \tag{2.5}$$

and

$$\begin{aligned} z = {} & \frac{1}{\alpha}[\beta(M_c^2 + m_1^2 - (m_2 + E_x)^2) \\ & - \cos\theta_{\mathrm{cm}} \sqrt{\left(M_c^2 - (m_1 + m_2 + E_x)^2\right)\left(M_c^2 - (m_1 - m_2 - E_x)^2\right)}, \end{aligned} \tag{2.6}$$

where $\alpha = \frac{cZB}{2\pi}$, E_t is the total energy of the system in the CM, γ is the Lorentz factor, M_c is the total mass of the system, and m_1 and m_2 are the masses of the scattered particles. It can be shown that the mapping between the measured energy and coordinate and the observable of interest leads to the following equations [39]:

$$\boxed{E_x = -m_2 + \sqrt{M_c^2 + m_1^2 - 2\gamma M_c(E - \alpha\beta z)}} \tag{2.7}$$

and

$$\boxed{\cos\theta_{cm} = \frac{\gamma(E\beta - \alpha z)}{\sqrt{\gamma^2(E-\alpha\beta z)^2 - m_1^2}}.} \tag{2.8}$$

The kinematic lines for the ejected proton in the example reaction $^{28}\mathrm{Si(d,p)}^{29}\mathrm{Si}$ at 6 MeV/u in 2 T are reported graphically in Fig. 2.10.

Eqs. 2.10 and 2.11 only hold in the unrealistic/ideal case of an ejectile detector with vanishing transverse dimensions. In reality, the detector has a finite size, and corrections to the kinematic calculations become necessary due to ejectiles not returning fully to the beam axis but instead are incident on the detector before reaching it. If $\rho \gg a$ (where ρ is the trajectory radius and a is a measure of the detector size) the return hit position is given by the expression:

$$z_{\mathrm{hit}} \approx z_0 \left(1 - \frac{1}{2\pi}\frac{a}{\rho}\right). \tag{2.9}$$

where z_0 is the position on the beam axis where the particle would return in the case of an infinitely small detector. As shown in Fig. 2.11, this affects the kinematical lines of the ejected protons. For further details, refer to Ref. [39].

$$\boxed{E_x = -m_2 + \sqrt{M_c^2 + m_1^2 - 2\gamma M_c(E - \alpha\beta z)}.} \tag{2.10}$$

and

$$\boxed{\cos\theta_{\mathrm{cm}} = \frac{\gamma(E\beta - \alpha z)}{\sqrt{\gamma^2(E-\alpha\beta z)^2 - m_1^2}}.} \tag{2.11}$$

with $\alpha = \frac{cZB}{2\pi}$.

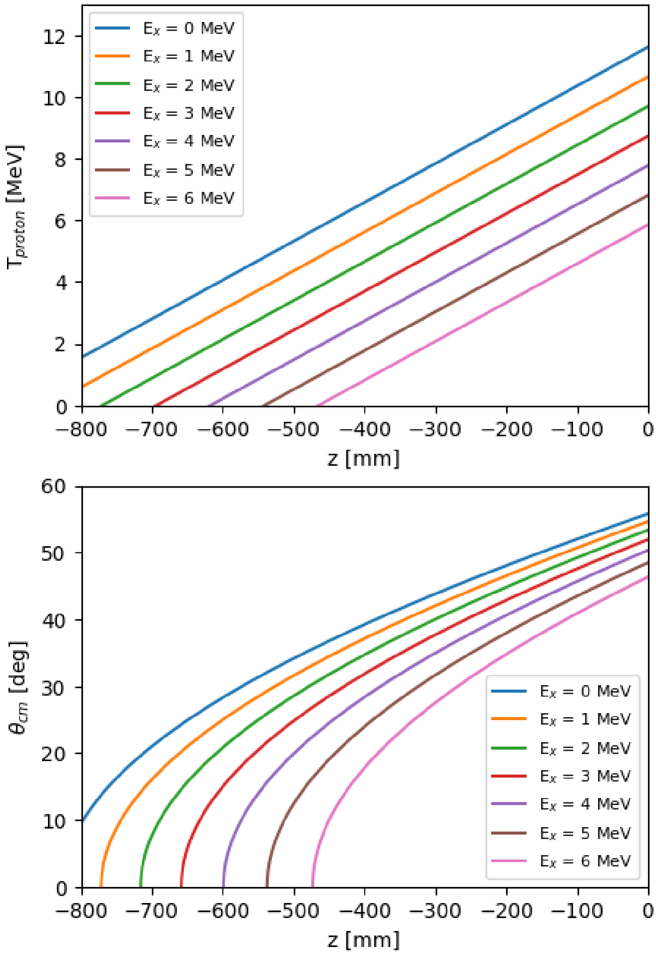

Figure 2.10: Kinematic plots for the $^{28}\mathrm{Si(d,p)}^{29}\mathrm{Si}$ reaction at 6 MeV/u in 2 T. The upper panel displays the energies of protons as a function of z, while the lower panel shows the proton emission angle in the center-of-mass frame, θ_{cm}, as a function of z. Each line represents a fictitious excited state of ^{29}Si, with excitation energies ranging from 0 to 6 MeV in 1 MeV intervals. This plot assumes no transversal dimension of the ejectile detector array.

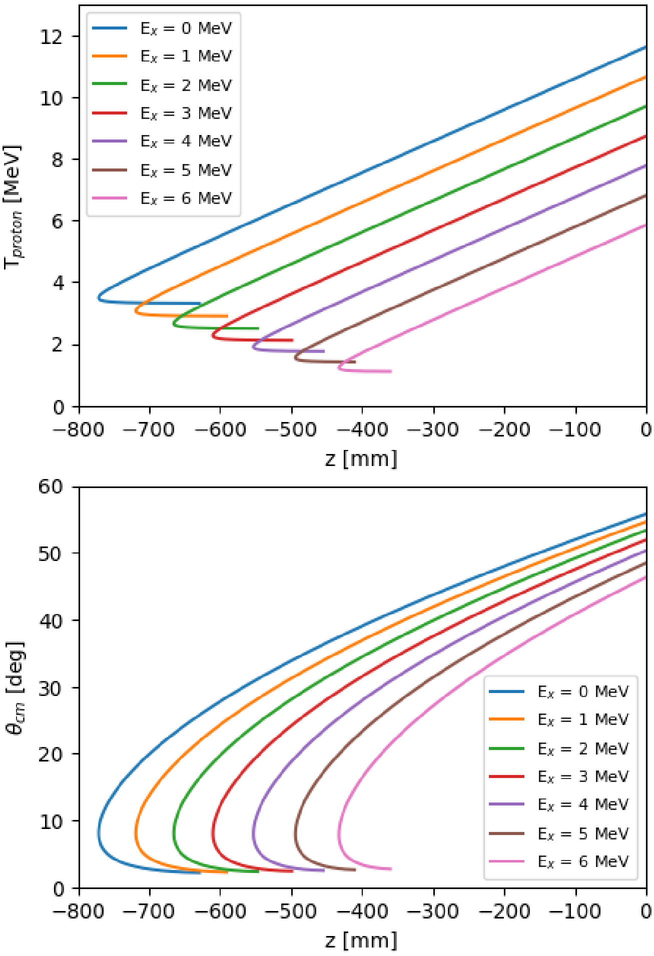

Figure 2.11: Kinematic plots for the ^{28}Si(d, p)^{29}Si reaction at 6 MeV/u in a 2 T magnetic field, with a detector having an axial size of 11.5 mm. The upper panel displays the energies of protons as a function of z, while the lower panel shows the proton emission angle in the center-of-mass frame, θ_{cm}, as a function of z. Each line represents a fictitious excited state of ^{29}Si, with excitation energies ranging from 0 to 6 MeV in 1 MeV intervals.

Chapter 3

Experimental setup

In order to measure fission barriers and cross-sections of neutron-rich nuclei in inverse kinematics at ISOLDE, a new experimental setup consisting of several detectors has been designed and optimized. Each detector operates in the vacuum inside the ISS superconducting solenoid and provides different observables which are combined to extract the fission probability as a function of the excitation energy.

When measuring $(\mathrm{d}, \mathrm{pF})$ reactions, the distinguishing feature that identifies a fission event from everything else is the detection of the backward-ejected protons in *coincidence* with the fission fragments. As already discussed in Sec. 2.3.1, the excitation energy E_{x} of the fissioning nucleus can be determined from the deposited energy and hit position of the emitted proton according to Eq. 2.10. Knowing the number of fission events $N_{d,pF}$ in an excitation energy interval one can calculate the fission probability P_f for the residual nucleus as a function of the excitation energy as:

$$P_f(E_{\mathrm{x}}) = \frac{N_{d,pF}(E_{\mathrm{x}})}{N_{d,p}(E_{\mathrm{x}}) \cdot \epsilon_f}, \tag{3.1}$$

where $N_{d,p}(E_{\mathrm{x}})$ represents the number of (d,p) events, and ϵ_f represents the fission fragment detection efficiency. Additionally, elastically scattered deuterons are detected in the forward direction in order to measure the beam current hitting the target. This is needed to calculate absolute cross-sections. Finally, the total energy and multiplicity of gamma-rays emitted during fission, which are an ingredient for r-process simulations and for a better understanding of angular momenta of fission fragments, are also measured [40]. Fig. 3.1 gives a schematic overview of the detector arrangement. In the following sections, the target and the individual detectors used to detect the aforementioned particles are described in detail, while the simulation results of their responses will be discussed in Chapter 5.

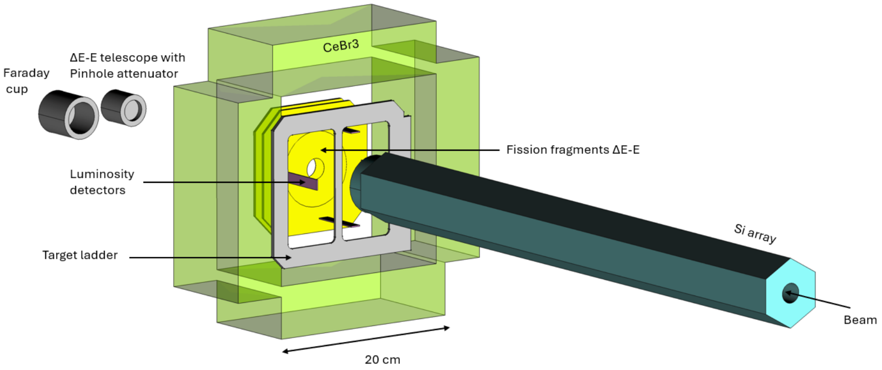

Figure 3.1: Schematic illustration of the detectors surrounding the target inside the vacuum chamber of the ISS magnet. The Faraday cup and the $\Delta\mathrm{E}-\mathrm{E}$ telescope, along with its attenuator, are mounted on a movable support, with only one of these components used at any given time. Except for the beam monitor detectors, all dimensions and positions are to scale and have been optimized through simulations. The hollow upstream silicon array is also shown. The beam enters from the right. Figure from Ref. [41].

3.1 Target

To enable (d, pF) and $(\mathrm{d}, \mathrm{p}\gamma)$ reactions, a deuterated plastic target, CD_2, with a thickness of $0.5-1.0\ \mathrm{mg/cm^2}$ will be used. This thickness represents a trade-off between energy resolution and maximum achievable luminosity: while a greater thickness would increase the interaction rate, it would also degrade the energy resolution. Specifically, a thicker target causes the reaction products to lose more energy as they traverse the material, leading to increased energy straggling and broader peaks in the energy spectra. If the beam intensity on the target is sufficiently high, a $0.5\ \mathrm{mg/cm^2}$ target might be used otherwise.

3.2 Position-sensitive silicon array

As already mentioned, one of the reaction products of the (d, pF) reaction is an ejected proton following helical trajectories due to the presence of a uniform magnetic field inside the solenoid. The protons emitted backwards are detected by a position-sensitive silicon array surrounding the incoming beamline. This array features a hexagonal geometry and consists of 24 Double-Sided Silicon

Strip Detectors (DSSSDs), each with 128 strips of 0.95 mm pitch on the front (p-side) and 11 strips of 2 mm pitch on the back (n-side), as shown in Fig. 3.2. The DSSSDs are organized into three modules of eight detectors each (i.e. two sides of the hexagon) coupled to ASIC readout. This configuration allows the system to achieve a Q-value resolution approaching 20 keV [42]. The hit position along the incoming beam axis, z, is determined from the index of the hit on 128 p-side strips, which are paired across the pairs of silicon wafers within a given module. The x-y position (i.e. the azimuthal angle of the impact point), on the other hand, is determined from the 11 n-side strips, which are read out to individual channels per wafer. The radius of the array from the beam axis to the surface of the detector is 30 mm and its solid angle coverage is 94% in the beam axis direction (related to the proton emission θ angle) and 70% in the azimuthal direction. The length of the active area of the detector is 501.5 mm. Its distance to the target can be changed using a motorized system from a minimum of 14.5 mm [42] depending on the excitation energy range of interest to be covered by the measurement.

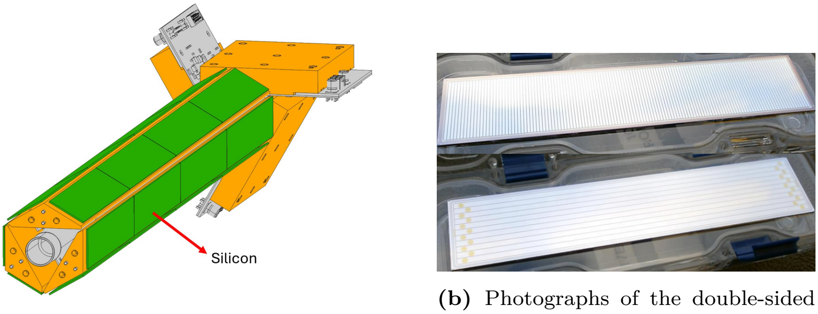

(a) Schematic illustration of the hexagonal-shaped silicon array used for detecting ejected protons. Figure from Ref. [41].

(b) Photographs of the double-sided silicon strip detectors, showing the full junction side in the top photograph and the ohmic side in the bottom photograph.

Figure 3.2: Overview of the silicon array and detectors.

While only protons can reach the array positioned in the backward direction from (d,p) reactions with a CD_2 target, the situation is quite different for the carbon component of the target. A major source of background is believed to originate from Multi-Nucleon Transfer (MNT) reactions with the carbon nuclei in the target, which can produce, among other possible outcomes, light-charged ejectiles (primarily α particles) also in the upstream direction. Fortunately, the cyclotron period T_{cyc} (as defined in Eq. 2.2) of these ejectiles is approximately 65 ns or longer, which is distinct from that of protons, which is about 32 ns. This difference *would* allow us to suppress the non-proton signals if the time difference between hits in the array and the fission fragment detectors is measured with sufficient resolution. Inelastic scattering does not produce reaction products in the backward direction, and the probability of emitting light charged particles in a fusion-evaporation reaction is below 1 %, according to a PACE4 calculation. For more details, please refer to App. A. Finally, an additional contribution to the array singles data beyond (d,p) reactions most likely comes also from deuteron breakup that needs to be taken into account when extracting absolute cross-sections. Background measurements using a pure carbon target of equivalent thickness will be conducted to evaluate and subtract the background.

3.3 ΔE-E silicon telescope

In inverse kinematics, fission fragments from the (d, pF) reaction are boosted in the forward direction, exhibiting an angular distribution that is strongly forward-peaked in the laboratory frame. This results in a cone-shaped emission with an opening angle that depends on the beam energy and the transverse momentum of the fragments (Fig. 3.3).

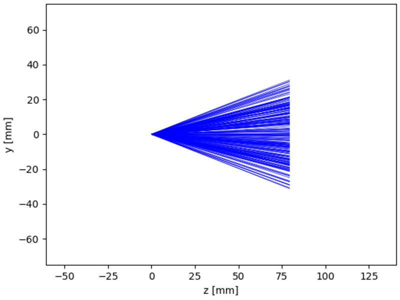

Figure 3.3: In blue, the (y,z) trajectories of fission fragments resulting from ^{229}Ac(d,pF) reactions at 8 MeV/u in a 2 T magnetic field, exhibiting a forward-peaked, cone-shaped distribution.

The use of an annular geometry detector centered on the beam axis provides efficient detection of both fission fragments simultaneously while allowing any unreacted beam to pass through the central hole. The chosen detector consists of two double-sided silicon Micron S3 detectors [43], shown in Fig. 3.4, arranged as two layers in a $\Delta\mathrm{E}-\mathrm{E}$ telescope configuration. The detailed dimensions of this type of detector are reported in Tab. 3.1. The segmentation in rings and sectors enables unambiguous fission event identification by two coincident hits that differ in azimuthal angle by 180° since the fission fragments are emitted back-to-back in the CM frame. A $\Delta\mathrm{E}-\mathrm{E}$ measurement is possible for fragments punching through the $65\,\mu$m thick ΔE detector and also hitting the $1000\,\mu$m thick E detector. Typical fission fragments would deposit about 0.5 GeV in each layer and the pulse-height-defect caused by this would degrade drastically the energy resolution achievable making it impossible to perform isotopic identification of the fragments [44]. However, lighter nuclei, e.g. carbon or deuterium nuclei scattered out of the target can be distinguished if they reach the detectors. Fig. 3.5 shows the placement of the target, the DSSSD array, and the fission fragment detectors within the experimental setup.

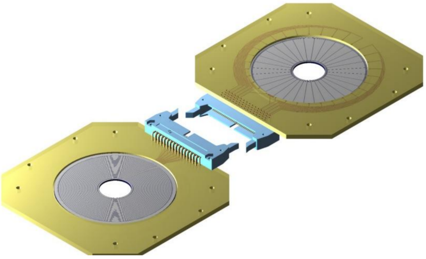

Figure 3.4: The S3 detector and PCB, viewed from the *p*- and *n*-sides, will be used in a $\Delta \mathrm{E} - \mathrm{E}$ telescope configuration. Figure adapted from Ref. [43].

Dimensions	
Chip inner diameter	20 mm
Chip outer diameter	76 mm
Active Si inner diameter	22 mm
Active Si outer diameter	70 mm
Junction elements No.	24 (rings)
Ohmic elements No.	32 (sectors)
Thickness	
ΔE	65 μm
E	1000 μm

Table 3.1: Dimensions of the individual S3 detectors used in the $\Delta \mathrm{E} - \mathrm{E}$ telescope configuration to detect fission fragments. The segmentation into rings and sectors allows for the unambiguous detection of the two fission fragments emitted at azimuthal angles of 180° relative to each other.

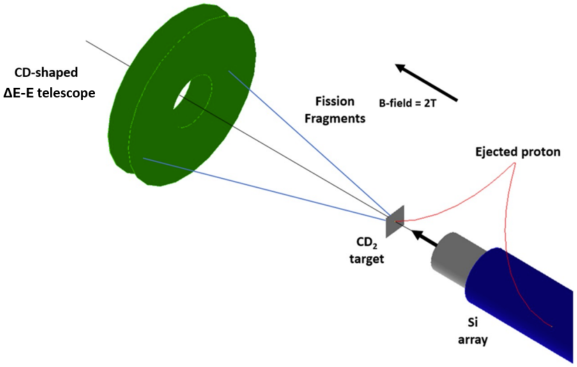

Figure 3.5: Schematic illustration of the experimental setup. The accelerated beam enters from the lower right into the superconducting solenoid, passing through the hollow, position-sensitive silicon detector array located upstream of the target. The typical helical trajectories of protons and the helical arc of fission fragments are shown. The forward-boosted fission fragments are detected by a $\Delta\mathrm{E} - \mathrm{E}$ silicon telescope placed downstream.

3.4 $\mathrm{CeBr_3}$ scintillation array

As already stated, knowing the amount of energy and the multiplicity of γ-rays released during fission can improve models and simulations of the r-process and enhance our understanding of how angular momentum is distributed during the fission process [40].

For this purpose, γ-rays will be detected in coincidence with $(\mathrm{d}, \mathrm{pF})$ reactions using $\mathrm{CeBr_3}$ crystals from the SpecMAT detector, designed by the KU Leuven group. These crystals are read out by silicon photomultipliers and therefore suited for operation in vacuum and in the presence of a strong magnetic field. Thirty-six of these crystals will be mounted in a new mechanical support, arranged in a box-like configuration with two rings, as shown in Fig. 3.6. This geometric configuration has been chosen after simulating several different arrangements, as it optimizes detection efficiency. Each scintillator unit consists of a $48 \times 48 \times 48$ mm^3 $\mathrm{CeBr_3}$ crystal coupled to a SensL J-series 8×8 SiPM array of 6×6 mm^2 single square sensors. The expected photo-peak detection efficiency for γ-rays at 1 MeV is 2.5 % [45]. A 2 mm aluminum shield placed just in front of the γ-ray windows prevents the implantation of charged particles in the active volumes of the detectors.

A complete detector unit is shown in Fig. 3.7 (a). The inner structure of the detector is schematically illustrated in Fig. 3.7 (b).

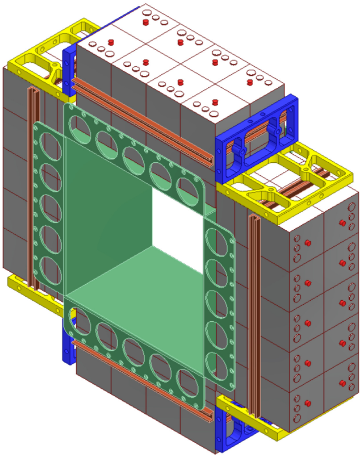

Figure 3.6: Schematic of the new mechanical support for $CeBr_3$ crystals arranged in a box-like configuration with two rings. Single $CeBr_3$ crystals are shown in grey. Figure from Ref. [41].

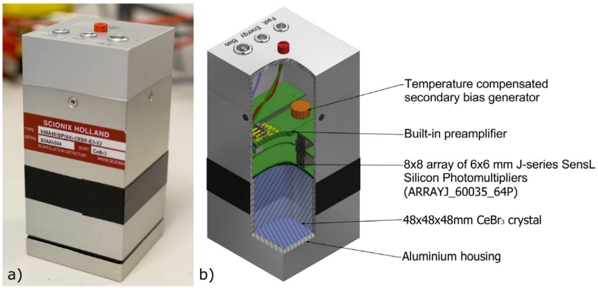

Figure 3.7: A $48 \times 48 \times 48$ mm^3 $CeBr_3$ detector unit: (a) a complete detector and (b) a cutaway view of the detector (CAD illustration). The SiPM array is powered by a temperature-compensated bias generator. The detector operates from a +5 V external bias. Figure from Ref. [45].

3.5 Luminosity monitor

An accurate measurement of the beam luminosity is provided by detecting elastically scattered deuterons by using an off-axis luminosity monitor. This detector consists of four position-sensitive silicon wafers, each with an active area of $50 \times 10\,\mathrm{mm}^2$ (see Fig. 3.8), mounted parallel to the beamline with the active surfaces facing the beam axis. These detectors measure elastically scattered deuterons from the target. They are placed at positions differing by 90° in

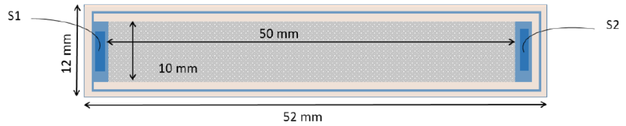

Figure 3.8: Position-sensitive silicon sensor: When a charged particle hits the detector, it deposits energy E. Signals are collected at contacts S1 and S2, which are used to infer the position along the strip through resistive sharing of the signal charge. The figure shows the dimensions of both the board ($12 \times 52\,\mathrm{mm}^2$) and the active area of the silicon wafer ($10 \times 50\,\mathrm{mm}^2$). Figure taken from Ref. [47].

azimuthal angle. This setup compensates for imperfections in the beam tune, such as misalignments, angular deviations, or the finite beam spot size on the target, by measuring scattered deuterons from different angles. This layout is inspired by experience with the HELIOS and SOLARIS spectrometers, where a similar configuration has been successfully employed [46].

Simulation results for optimizing the design and geometry of this luminosity monitor will be discussed in Chapter 5. Box 3.6 presents a practical example of determining the beam luminosity from simulations when compared to experimentally measured values.

3.6 Beam diagnostic detectors

Finally, the two most downstream devices are used for beam diagnostics: a Faraday cup and a $\Delta\mathrm{E}-\mathrm{E}$ detector. The Faraday cup monitors the beam current, while the $\Delta\mathrm{E}-\mathrm{E}$ detector is typically used to test the purity of the beam. However, in our case, the $\Delta\mathrm{E}-\mathrm{E}$ detector will not be able to detect any contaminants, as the beam used in the proposed experiment (^{229}Ac at 8 MeV/u) will not be isotopically resolved. These devices were primarily designed for examining the beam without any obstruction from a target. The $\Delta\mathrm{E}-\mathrm{E}$ detector is composed of two ORTEC silicon surface detectors, each with an active area of 150 mm^2 [48]. The Faraday cup can also be used to monitor the target integrity during the experiment, as heavy beams can degrade the target.

Luminosity Monitor Yields

Accurate beam intensity measurements are crucial for determining absolute quantities, such as cross-sections. Rutherford scattering is widely used for this purpose due to its well-established theoretical framework and known cross-section, making it a reliable method. One of the main advantages is that it allows intensity measurements without altering the beam by using inevitable background events. Additionally, it can be analyzed for individual target species and works effectively over a wide range of scattering angles, especially at low beam energies. Luminosity detectors measure elastically scattered events, allowing to determine the product of the beam particle rate and the target thickness.

Experiment

For a given reaction involving a beam of intensity I_0 (ions/s) incident on a target containing N_t (atoms/cm^2) nuclei per unit area, the number of scattered particles J (count/s) is given by:

$$J = I_0 N_t \sigma, \tag{3.2}$$

where σ is the total cross-section. When considering a detector of finite size covering a solid angle $\Delta\Omega$, the differential cross-section, $\frac{d\sigma}{d\Omega}(\theta, \phi)$, is more useful. It represents the likelihood of particles being scattered in a specific direction, characterized by the polar and azimuthal angles θ and ϕ.
The experiment luminosity, in units of b^{-1}, can thus be experimentally determined as:

$$I_0 N_t = \frac{Y}{\frac{d\sigma}{d\Omega} \cdot \Delta\Omega \cdot \varepsilon_\pi \varepsilon_\delta}, \tag{3.3}$$

when the absolute efficiency of the detector ε_δ, the beam purity ε_π, and Y, the yield measured by the detector, are all known. A more accurate value is obtained by using e.g. DWBA models to calculate the differential cross section instead of the pure Rutherford estimate. This product is the only quantity that can be easily experimentally determined, as it is difficult to disentangle I_0 and N_t when performing an experiment. The quantity $\frac{d\sigma}{d\Omega} \cdot \Delta\Omega = \sigma_{\text{det}}$ is the cross section for scattering into the detector.

Simulations

The main advantage of performing simulations is that they provide access to a wealth of information typically unavailable in experiments, allowing for valuable insights into the simulated experiment. Typically, the simulation framework will provide the total number of simulated events, N_{simul}, representing the originally elastically scattered deuterons, the number of recorded hits in the simulated detector volume, N_{det}, and the cross-section, σ_{int}, integrated over the sampled angular range. It thereby gives the crucial connection between σ_{int} and σ_{det} where the former comes from the physics model (Rutherford, DWBA etc.) and the latter also takes efficiencies and detector geometry (placement and shape) into account through $\frac{N_{\text{simul}}}{N_{\text{det}}}$. Thus, the corresponding luminosity can be related to the cross-section as follows:

$$(I_0 N_{\text{t}})_1 = \frac{N_{\text{simul}}}{\sigma_{\text{int}} \cdot N_{\text{det}}}. \tag{3.4}$$

As with Eq. 3.3, Eq. 3.4 allows us to calculate the experiment luminosity in b^{-1}, though with a subtle but important difference. While the former equation provides the luminosity needed to obtain the actual yield Y recorded by the detector, the latter indicates the experiment luminosity required to achieve a single hit in the detector volume, as explicitly indicated by the subscript $(\ )_1$. It is worth noting that the calculated quantity is independent of the target properties (thickness, density etc.), as all the relevant target information is encapsulated in N_{t}.

Practical example (IS621 experiment)

The IS621 experiment, reported in Ref. [49], probed single-particle states in ^{29}Mg using the d(^{28}Mg,p)^{29}Mg transfer reaction. In that experiment, the ELUM detector introduced in Chapter 5 was used as a luminosity monitor, positioned 125.7 mm downstream from the target. The target thicknesses, recorded counts, beam purity (ϵ_π), and detection efficiency (ϵ_δ) for the experiment are listed in Tab. 1.2.

Target (μg/cm^2)	Counts	Beam Purity (ϵ_π)	Detection eff. (ϵ_δ)
80	2929 ± 59	0.92	0.5
120	1440 ± 42	0.92	0.5

Table 3.2: Experimental counts and parameters for different target thicknesses in IS621.

Only two quadrants of the ELUM were used to ensure that any loss of counts from deuterons hitting the support structures was minimized. The beam purity ϵ_π was determined using a ΔE-E beam diagnostic detector. The experiment luminosity values obtained were:

Target thickness (μg/cm^2)	$I_0 N_t \pm$ stat. $\pm$ sys. (mb^{-1})
80	$743 \pm 15 \pm 76$
120	$365 \pm 11 \pm 41$

Table 3.3: Luminosity calculated for experiment IS621, as reported in Ref. [49]. The statistical error arises from uncertainties in yield extraction, while the systematic error is influenced by the optical model dependence.

A simulation performed in this work of the same experiment is summarized in Tab. 3.4.

N_{simul}	10^5
θ_{lab} [deg]	$[70, 82]$
ϕ [deg]	$[-180, 180]$
σ_{int} [b]	0.3223

$$\xrightarrow{\text{gives}} \quad N_{\text{det}} = 2576.$$

Table 3.4: Simulation input parameters and resulting detected counts.

By inserting these values in Eq. 3.5, we get an experiment luminosity per scattered particle of:

$$\boxed{(I_0 N_{\text{t}})_1 = 0.12\ mb^{-1}}$$

Please note that the integrated cross section here was calculated assuming pure Rutherford scattering; effects of DWBA (Distorted Wave Born Approximation) optical potentials on the differential cross section have not been taken into account, but the difference is less than 8% at the angles used.

If the value obtained is now multiplied by the number of counts detected in the IS621 experiment (Tab. 3.2), the resulting experimental luminosity values are:

$$\begin{aligned} I_0 N_t &= (I_0 N_T)_1 \cdot 2929 = 351 \text{ mb}^{-1}, \\ I_0 N_t &= (I_0 N_T)_1 \cdot 1440 = 173 \text{ mb}^{-1}. \end{aligned} \tag{3.5}$$

Note that these values show a difference compared to those obtained experimentally in Tab. 3.3, which is in line with the simulation setup, where the full ELUM geometry is considered.

Chapter 4

Fission of ^{230}Ac

The r-process path spans regions of the nuclear chart far from the valley of β-stability. Due to the extreme neutron excess and the technical challenges of producing and isolating such exotic nuclei, beams of most of the isotopes involved are currently unavailable.

The work presented in this thesis aims to establish a new experimental method for the systematic study of fission of neutron-rich nuclei. This method involves using radioactive beams in inverse kinematics within a solenoidal spectrometer, initially applied to less exotic nuclei. However, it can later be extended to more neutron-rich nuclei, closer to the r-process path, as experimental beam production advances. The data thus obtained can be used to test theoretical models for nuclei within experimental reach, refine these models, and extrapolate properties of nuclei that are not yet accessible. This process will enhance the predictive power of these models for isotopes that remain beyond current experimental capabilities, such as those crucial to the r-process.

The reaction proposed as the first measurement of this novel approach is $^{229}\mathrm{Ac(d, pF)}$ at 8 MeV/u.

Before discussing the reasons for selecting ^{230}Ac as the first nucleus of interest for this study, it is necessary to introduce the model adopted to predict its fission properties.

4.1 The GEF model

The semi-empirical “GEneral description of Fission observables” (GEF) model code predicts observables for fissioning nuclei via spontaneous fission, neutron-induced fission, and, more generally, for the fission of a compound nucleus from any entrance channel with specified excitation energy and angular momentum. It offers a consistent description of a wide range of experimental observables, including the properties of fission fragments at scission — such as mass, charge, excitation energy, and angular momentum — as well as the fission fragment kinetic energies. Additionally, GEF models the de-excitation of the fission fragments, providing the prompt-neutron and prompt-gamma multiplicities for each fragment, along with the corresponding prompt-neutron and prompt-gamma energies and angles. All of this information is provided by the code on an event-by-event basis, making it useful as an event generator for simulation purposes. GEF can describe a wide range of isotopes, from polonium (Po) to seaborgium (Sg), at excitation energies up to about 100 MeV, including multi-chance fission, and provides predictions even for nuclei where no experimental data is available [50].

4.1.1 Basic ideas of the GEF model

GEF relies primarily on physics concepts of a more general nature rather than on microscopic calculations. This approach is chosen to reduce the high computational demands and to make the code suitable for the calculation of many nuclear systems. For more detailed information, please refer to the official documentation in Ref. [50].

Fission Barriers

One of the key ingredients of the GEF model is the height of the fission barrier, which strongly influences the fission decay-width. GEF estimates fission barriers by combining the macroscopic liquid drop model with empirical shell corrections that account for effects such as nucleon pairing and shell structure, as outlined by the microscopic-macroscopic approach [51]. However, according to the topographic theorem [52], only the shell correction energy at the ground state is considered, while the overall shape of the potential energy surface on the path to scission is primarily determined by the macroscopic fission barrier. Shell corrections at the saddle point are not considered for the fission barrier height, as they have minimal impact on the nuclear binding energy and, consequently, the saddle-point mass. Therefore, the fission barrier height B_f can be approximated with good accuracy as:

$$B_{\mathrm{f}} \approx B_{\mathrm{f}}^{\mathrm{macro}} - \delta U_{\mathrm{gs}}. \tag{4.1}$$

Here, $B_{\mathrm{f}}^{\mathrm{macro}}$ represents the macroscopic barrier, and δU_{gs} is the shell correction energy at the ground state. The basic idea behind this approach is illustrated in Fig. 4.1.

Fission channels

Quantitative predictions of fission-fragment yields are determined by the potential energy surface between the fission barrier and the scission point as a function

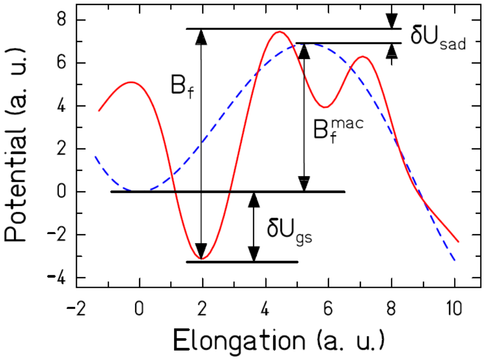

Figure 4.1: Schematic illustration of the potential energy along the fission path relative to the macroscopic ground-state energy for a nucleus deformed in its ground state. The spherical shape is located at zero elongation. The macroscopic potential is shown by the dashed blue line, while the full potential, including the shell effect, is represented by the solid red line. δU_{sad} denotes the shell corrections at the saddle, whereas δU_{gs} represents the shell correction energy at the ground state. Figure from Ref. [50].

of the mass-asymmetry degree of freedom. As discussed in the previous section, GEF models the potential energy surface using a microscopic-macroscopic approach.

The inclusion of microscopic shell corrections accounts for the increased stability of certain nuclei and certain shapes by lowering the potential energy surface, thereby producing energy minima in specific deformation configurations. As the number of available nuclear levels increases exponentially with the excitation energy, the lowering of potential regions leads to a higher level density for a given excitation energy. The higher the level density in a particular region of the potential energy surface, the higher the probability for the nucleus to follow a fission path through that channel. Fig. 4.2 shows the transition from symmetric to asymmetric fission for three fissioning nuclei. The potential as function of the asymmetry of the fission fragments is plotted. The interplay between the macroscopic potential, favoring symmetric fission and a shell effect at $Z = 55$ is illustrated. For increasing nuclear charge of the fissioning nucleus, the symmetric splitting moves closer to the position of the shell, fixed at $Z = 55$. In radium ($Z_{\mathrm{CN}} = 86$), the potential is lowest at mass symmetry, leading to single-humped mass distributions, in thorium ($Z_{\mathrm{CN}} = 90$), the potential is nearly equal at symmetry and near $Z = 55$, resulting in triple-humped mass distributions. In plutonium ($Z_{\mathrm{CN}} = 94$), the potential is lowest near $Z = 55$, favoring double-humped mass distributions.

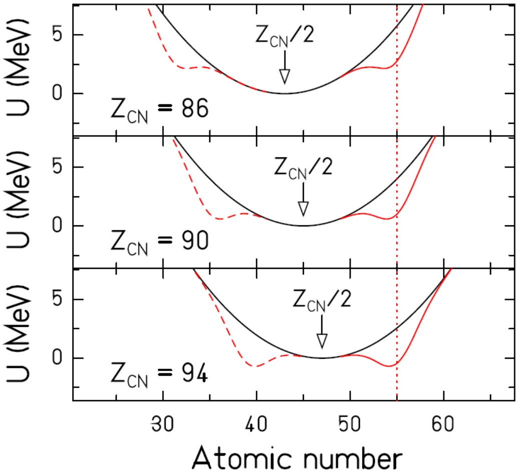

Figure 4.2: Schematic illustration of the potential energy along the fission path for mass-asymmetric shape distortions. The black curve represents the macroscopic potential, which is minimized at symmetry, while the red curve includes the additional binding effect from an assumed shell at $Z = 55$ in the heavy fragment. Figure from Ref. [50].

Finally, the concept of quantum oscillators is used to address the charge polarization[1], which influences the charge yields [54]. Adjustment of the predictions from this formalism to benchmark experimental mass and charge distributions across a wide region of the nuclear chart demonstrated the need for four fission channels: the symmetric SL channel and three asymmetric channels (standard S1 and S2, and very asymmetric SA[2]). This empirical adjustment procedure establishes the values of the model parameters related to fragment (A, Z) yields.

Energy sorting

As mentioned above, the early manifestation of fragment shells on a fission path suggests that the fragments acquire their individual characteristics already in the vicinity of the fission barrier. Thus, even well before the scission point, the fissioning system can be considered to consist of two well-defined nuclei joined by a neck. Before scission, the available intrinsic excitation energy E_x must be distributed between the fragments.

In GEF, the partition of excitation energy is determined using statistical mechanics. It is assumed that the system formed by the two nuclei reaches statistical equilibrium, where all energetically possible configurations have an equal probability of being populated. Consequently, the excitation energy partition is governed by a probability distribution, which is the product of the level densities of the individual fragments. The average excitation energy of the light fragment, denoted as $< E_L >$, at thermal equilibrium can be calculated using the following expression:

$$< E_L >= \frac{\int_0^{E_\mathrm{x}} E_L \rho_L(E_L) \rho_H(E_\mathrm{x} - E_L) dE_L}{\int_0^{E_\mathrm{x}} \rho_L(E_L) \rho_H(E_\mathrm{x} - E_L) dE_L}, \tag{4.2}$$

with ρ_L and ρ_H denoting the level densities of the light and heavy fragments, respectively.

Deviations in the nuclear level density from a non-interacting Fermi gas model occur when pairing correlations are significant. As the nucleus gains excitation energy, Cooper pairs begin to break, leading to an increase in the

---

[1] The charge polarization is the deviation from the Unchanged Charge Distribution (UCD) assumption in which the fragments keep the neutron-proton ratio of the fissioning parent nucleus [53].

[2] The various fission modes correspond to distinct valleys in the potential-energy landscape. Three main modes are typically identified: *super long* (SL), *standard 1* (S1), and *standard 2* (S2). The SL mode is characterized by symmetric yields and low total kinetic energy (TKE), which can be attributed to a significant deformation of both fission fragments at the scission configuration. The standard modes, S1 and S2, exhibit asymmetric mass distributions, with the average masses of the heavy fragments centered around 134 and 140, respectively. In contrast, the super asymmetric (SA) mode involves an even more pronounced mass asymmetry, where the two fission fragments differ significantly in size [50].

heat capacity of the nucleus and causing the level density to rise sharply. This increase is well approximated by an exponential trend with respect to excitation energy and suggests that the nucleus behaves like a system with a constant temperature within this pairing correlation regime, even as additional energy is added. Thus, the fissioning nucleus can be treated as a di-nuclear system between saddle and scission consisting of two coupled microscopic thermostats. Since the logarithmic slope of the level densities in the constant-temperature regime is proportional to $A^{2/3}$, the most probable configurations are those where the available excitation energy is concentrated in the heavy fragment. In other words, excitation-energy sorting occurs, with thermal energy being transferred from the light fragment to the heavy fragment [55, 56].

4.2 Identification of a candidate nucleus in ^{230}Ac

The GEF model predictions of fission probability distributions and neutron separation energies for different neutron-rich nuclei in the actinides region ($89 < Z < 103$) were examined to identify potential candidate nuclei to be studied. A list of these nuclei of interest is provided in Tab. 4.1.

Isotope	$\mathrm{S_n}$ **[MeV]**	Fission barrier [MeV]	$\mathrm{P_f}$ **first chance** [%]
^{237}Pa	5.9	5.4	11.0
^{238}Pa	4.7	4.5	11.0
^{235}Th	4.7	6.3	7.0
^{236}Th	5.8	6.3	4.5
^{229}Ac	6.3	9.9	3.5
^{230}Ac	4.9	7.0	3.0
^{231}Ac	6.2	7.1	2.3
^{228}Ra	6.3	8.0	0.4
^{229}Ra	4.5	8.1	0.3
^{230}Ra	6.3	8.1	0.2

Table 4.1: Predicted neutron separation energy S_n, fission barrier and first chance fission probability P_f, according to the GEF model.

Pa and Th isotopes would be very interesting to study due to their higher fission probabilities. However, currently, ISOLDE cannot deliver beams of these elements because it fails to extract them from the primary uranium target, owing to their higher refractory[3] nature compared to the target material. Therefore, ^{230}Ac has been selected, based not only on the predicted fission barrier shown in

---

[3] The term “refractory” refers to the property of a material that makes it resistant to heat and chemical wear, meaning that refractory elements are difficult to extract to their high melting points and strong chemical bonds.

Fig. 4.3, but also on the available beam intensities and production capabilities of the facility.

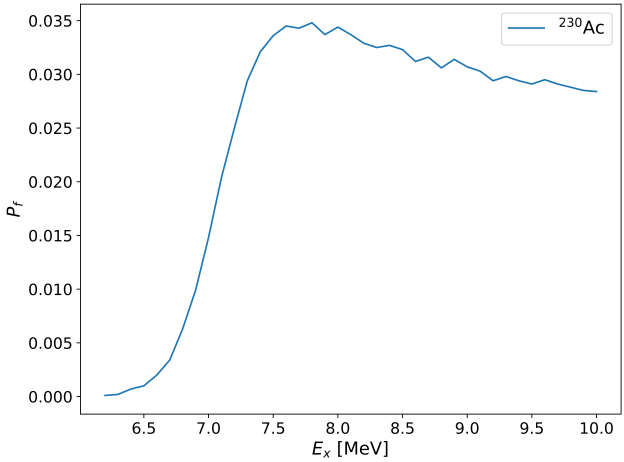

Figure 4.3: GEF prediction of fission probability as a function of excitation energy for ^{230}Ac.

The ^{230}Ac compound nucleus is produced from a ^{229}Ac beam, which can be extracted in molecular form as ^{229}AcFF^{+} from either thorium carbide (ThCx) or uranium carbide (UCx) targets with CF4 gas injection. This process leads to almost negligible Ra and Fr contamination of the beam [57].

Based on a previous proof-of-principle experiment using the HELIOS solenoidal spectrometer at ANL for the direct measurement of the fission barrier height of ^{239}U [2], and scaled to the present case of study, it is estimated that to achieve sufficiently high statistics for probing the fission barrier height of ^{230}Ac, a beam of ^{229}Ac with an energy of ≥ 8 MeV/u and an intensity of 1.3×10^5 particles per second (pps) on the ISS target is required. This needs an extraction rate of 1.3×10^7 pps, assuming an efficiency of approximately 1% from the initial low-energy stage to the high-energy beam accelerator lines. According to experts at ISOLDE, this is achievable [58]. All the scaling performed in order to estimate these numbers are described in the Fact-Box on page 50.

The choice to study ^{230}Ac is additionally motivated by the fact that its fission properties at low excitation energies have not been investigated before.

Two inconclusive β-delayed fission events have been observed using a mica-fission track detector exposed to a Ra source, which was produced via multinucleon transfer reactions and dissipative fragmentation induced by 60, MeV/u, ^{18}O ion irradiation of ^{232}Th targets [59]. These observations led to an estimation of the fission barrier height for ^{230}Ac as lying somewhere between 5.7 MeV and

6.8 MeV. On the other hand, a second experiment focused on studying heavy-ion induced fission at high excitation energies, resulted in an estimated fission barrier height of 5.37 MeV [60].

The experiment proposed in this work is planned based on the assumption that the fission barrier height of ^{230}Ac is as predicted by the GEF model, namely 7.01 MeV.

Scaling factor and beam rates

Beam rates required to probe the fission barrier of ^{230}Ac can be estimated based on data from a previous experiment conducted at ANL. In that experiment, a ^{238}U beam with an energy of 8.6 MeV/u and an average intensity of 10^6 particles per second (pps) was employed over seven days [2]. This empirical approach to estimating beam rates has been adopted because theoretical methods, such as DWBA calculations, rely on assumptions that are less reliable due to the limited knowledge of the structure of ^{230}Ac at the excitation energies of interest.

Following a similar methodology, determining the fission barrier height of ^{230}Ac requires obtaining 100 counts above the barrier per energy bin of 0.2 MeV (see Fig. 2 in Ref. [2]). However, whereas the fission probability P_f is 20 % for ^{239}U, it drops to a predicted value of 3 % for ^{230}Ac. Therefore, beam rate estimates for ^{230}Ac were accordingly scaled by weighting the beam intensity of the previous experiment with the relative fission probabilities.

Compared to the previous experiment, a gain of a factor of 16 per incident ion is expected due to the following improvements:

- Detection system: Replacing the gaseous fission fragment detectors with CD-shaped DSSDs (see Section 5.3). This provides a factor of 8 gain due to the larger angular coverage of the DSSDs.
- Target thickness: Using a CD_2 target twice as thick (1 mg/cm^2 instead of 500 μg/cm^2). This contributes an additional factor of 2 gain.

Under these improved conditions, the estimated beam intensity required to unambiguously determine the fission barrier heights of the two isotopes is as follows:

	Isotope	P_f (%)	**Target (μg/cm^2)**	**Est. req. beam int. (pps)**
ANL	^{239}U	20	500	10^6
ISS (scaled)	^{239}U	20	1000	$1/16 \cdot 10^6 = 6.3 \cdot 10^4$
ISS (scaled)	^{229}Ac	3	1000	$20/3 \cdot 1/16 \cdot 10^6 = 4.2 \cdot 10^5$

Table 4.2: Estimated beam intensity required to determine the fission barrier heights of ^{239}U and ^{229}Ac, assuming the use of a CD-shaped detection system for fission fragments and a 1000 μg/cm^2 target, compared to the reference experiment performed at ANL using a gaseous fission fragment detection system.

Finally, the scaling performed to estimate the required statistics for conclusively measuring the fission barrier height of ^{230}Ac is illustrated in the following flow diagram.

Protons

Generally, protons are on average delivered by the PSB in bunches every 2.4 s. The typical proton beam intensity values are:

$$\begin{aligned} & 3.0 \cdot 10^{13} \text{ ppp (protons per pulse)}, \\ = \ & 4.8 \cdot 10^{-6} \text{ C/pulse (Coulomb per pulse)}, \\ = \ & 2.0 \cdot 10^{-6} \text{ C/s}. \end{aligned}$$

Beam production yield

The intensity of the ^{229}Ac beam has previously been measured after the separator at ISOLDE using a Faraday cup and beam wire grids, and the result is ([57]):

$$10^{7} \ 1/\mu\text{C} \ = \ 2 \cdot 10^{7} \text{ pps}.$$

Beam intensity on experimental target

Assuming a transmission efficiency of 1 % from the ISOLDE separator through HIE ISOLDE, the beam intensity on the secondary target is expected to be:

$$2 \cdot 10^{5} \text{ pps}.$$

According to [57], even higher yields can be obtained if the beam-production target is heated to higher temperatures (above 2000 °C).

Chapter 5

Simulation results

In this section, the simulation framework is briefly described, followed by the simulation results for the position-sensitive silicon array, the fission fragment telescope, and the beam luminosity monitor, presented in the same order as in Chapter 3. It will be shown how the fission fragment detection efficiency can be increased by almost a factor 10, and how the luminosity determination becomes more selective through the use of position sensitive detectors. Finally, the simulated detector response to α emission from sources typically used at ISS is discussed.

5.1 Simulation framework: `Geant4` with `ggland`

The program `ggland` [61] is a command-line "wrapper" for the `GEANT3` [62] and `GEANT4` [63] physics simulation libraries. `ggland` has been developed to simplify performing simulations required for physics analysis in small nuclear physics experiments. Most of the meaningful configuration options can be modified directly from the command line. It provides:

- various methods to declare simple detectors with easily adjustable sizes;
- a versatile particle "gun" for generating particles for simulations;
- tools for the collection, pre-processing, and reduction of the plentiful output energy-deposit information generated by simulations of particle interactions with matter for use in analysis.

`ggland` delivers both "clusterized" information (time, energy, and position) and digitized information. The clusterized information is obtained by merging all energy deposits from the Monte Carlo simulation within regions of 1 cm and 0.066 ns, summed quadratically.

Particle generation in `ggland` is handled using "guns" and involves two steps. First, command-line options are parsed along with event-independent preparations. Second, each event is randomized, and the generated particles are "fired". For each generated particle, two parameters must be specified: the particle type and its kinetic energy. Additionally, particle types and momenta can be provided via input files. Furthermore, `ggland` supports the generation of multiple particles through two main approaches. In phase-space generation, particles share the available kinetic energy. Alternatively, a decay-scheme-like set of levels can be used, where each gun feeds subsequent guns, simulating a chain of decays. These two approaches can also be combined, allowing phase-space generators to both feed and be fed by a sequence of levels.

5.2 Detection of target-like protons

As discussed at the beginning of Chapter 3, determining the fission barrier height of ^{230}Ac requires probing its fission probability as a function of excitation energy. The latter can be derived from the deposited energy and the hit positions of protons which are ejected in the backward direction. The solenoidal field binds them onto the upstream position-sensitive silicon array. Protons are emitted following the (d,p) reaction, where the neutron transferred to the target nucleus populates single-particle doorway states, leading to the formation of a compound nucleus.

The GEF model estimates the fission barrier for ^{230}Ac to be 7.01 MeV. To experimentally determine this value unambiguously, backward ejected protons from (d,p) reactions that populate excited states in the range of $6-10$ MeV in ^{230}Ac need to be detected. The excitation energy range covered by the measurement depends on several factors, including the strength of the magnetic field, the length of the silicon array, and its distance to the target. Since the number of available nuclear levels increases exponentially with excitation energy, identifying the exact nuclear level populated during the formation of the compound nucleus is difficult. However, the model code `PTOLEMY`[1] [64] can be used to calculate the angular distributions in the CM system of the ejected protons when different single-particle orbitals of the compound nucleus are populated, as illustrated in Fig. 5.1. A single-particle orbital is identified by n and j, the principal quantum number and the total angular momentum quantum number, respectively. It can be observed that protons, in the CM, are predominantly emitted in the forward direction for all states of the compound nucleus.

---

[1] `PTOLEMY` is a program designed for computing nuclear elastic and direct-reaction cross sections. It performs optical model fits to elastic-scattering data at one or more energies and for various combinations of projectiles and targets. Additionally, it conducts collective model Distorted Wave Born Approximation (DWBA) calculations for excitation processes and finite-range DWBA calculations for nucleon-transfer reactions.

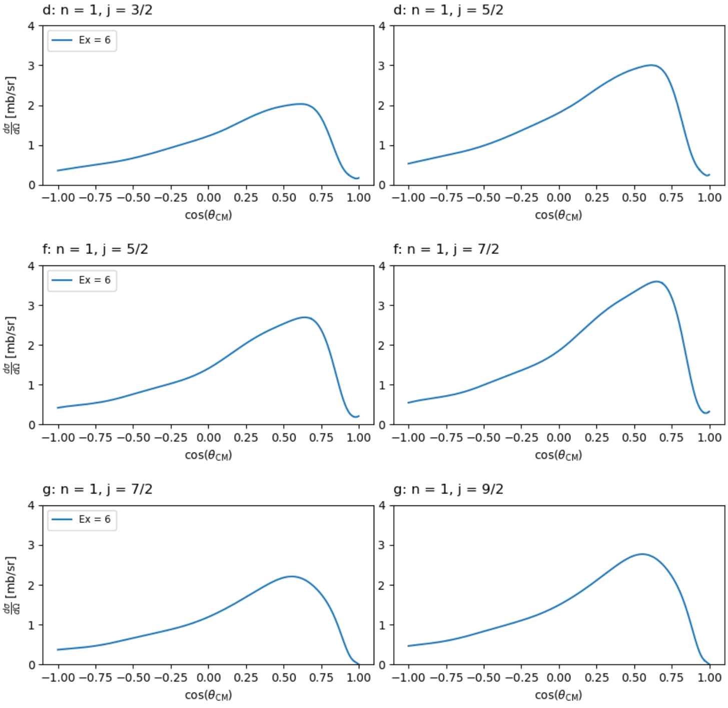

Figure 5.1: Cross sections for ejected protons as functions of emission angle in the CM frame are presented for different single-particle orbitals of the ^{230}Ac compound nucleus, populated at an excitation energy of 6 MeV, as predicted by the `PTOLEMY` code. The principal quantum number n and the total angular momentum quantum number j identify single-particle states. The orbital name (e.g. s, p, d, f etc.) is determined by the orbital angular momentum l, where $l = 0$ corresponds to s, $l = 1$ to p, $l = 2$ to d, and so on. Since the angular distribution in the CM frame is independent of excitation energy, only the case with an excitation energy of 6 MeV is shown.

Referring to Fig. 2.9, in (d,p) reactions in inverse kinematics, the proton emission at forward angles in the CM frame corresponds to a small momentum transfer, indicating that the proton retains much of the deuteron momentum. This forward emission implies that the proton is ejected in a direction similar to the initial motion of the deuteron, indicating that the reaction occurs with minimal deflection. Fig. 5.1 reports only the proton angular distributions for a few single-particle levels of the CN; for a more comprehensive overview, please refer to Appendix B.

In inverse kinematics, transforming from the CM frame to the laboratory frame results in protons emitted at the most forward angles in the CM frame

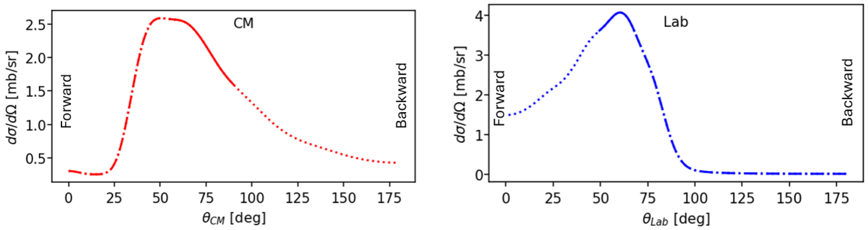

(a)

(b)

Figure 5.2: Angular distributions of emitted protons from the ^{230}Ac compound nucleus at 9 MeV excitation energy. Panel (a) shows the distribution in the CM frame, while panel (b) depicts the corresponding laboratory frame distribution, illustrating the transformation of forward and backward angles. The kinematic boost results in a nonlinear transformation between the CM and Lab frames as illustrated by the different line styles.

which appear at the most backward angles in the laboratory frame. Conversely, protons emitted in the backward direction in the CM frame are primarily focused in the forward direction in the laboratory frame, meaning at angles smaller than 90°, as illustrated by the different dashed lines in Fig. 5.2. The same angular distributions shown previously, are now transformed to the laboratory frame and presented in Fig. 5.3. Due to the kinematic boost, the transformation between the CM and the laboratory frames is not linear.

The higher the excitation energy of the compound nucleus is, the lower the energy of the ejected protons becomes, seen in Fig. 5.4. If the proton energy is lower, its momentum is also reduced, particularly the component of momentum in the direction parallel but opposite to the beam. This reduction causes the proton to complete a helical orbit in the magnetic field before traveling far along the z-axis. Therefore, in order to detect protons emitted during the formation of a compound nucleus with higher excitation energy, the silicon array should be positioned as close as possible to the target. Fig. 5.5 shows a typical simulated correlation between the proton energy E_p deposited in the silicon array and the z position of the hit in the laboratory frame.

Two types of protons can be distinguished: *single-turn protons*, which make up the majority of those emitted and complete only one helical orbit before hitting the array, and *multi-turn protons*, which are emitted at larger angles and typically have lower energy. As the name *multi-turn protons* suggests, these particles have a shorter helical pitch and complete several circular orbits before hitting the silicon array. The number of hits, or impacts of protons on the silicon array, varies with the distance between the silicon array and the target,

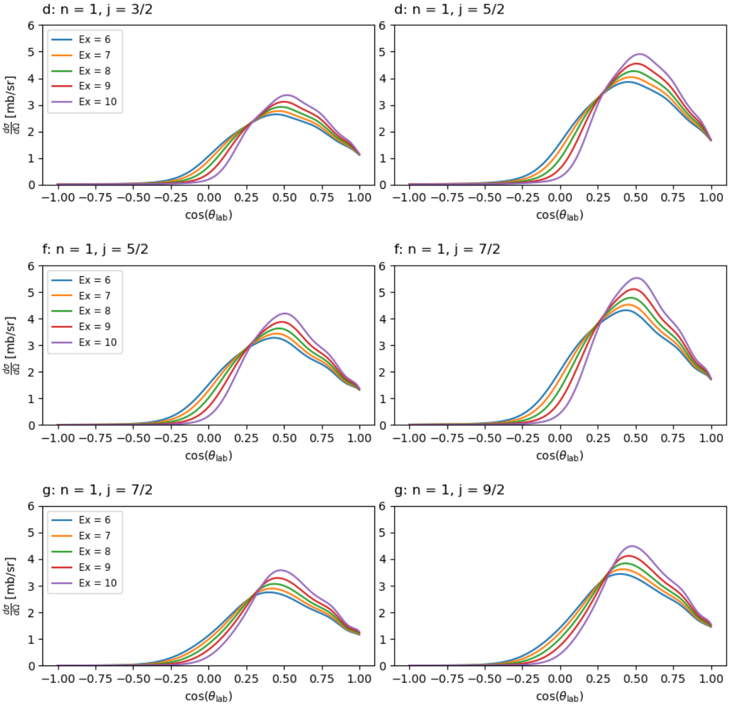

Figure 5.3: `PTOLEMY`-generated cross sections for proton emission as a function of the scattering angle in the laboratory reference system for different single-particle orbitals populated in ^{230}Ac with a (d,p) reaction with excitation energies ranging from 6 to 10 MeV.

depending on whether single-turn or multi-turn protons are considered, see Fig. 5.6. As expected, the number of single-turn protons emitted for nuclei with higher excitation energies (e.g. 10 MeV) increases as the silicon array is moved closer to the target, as illustated in the bottom panel of Fig. 5.6. The same cannot be said for multi-turn protons of the same kind, whose number decreases as the silicon array is moved closer to the target, since their trajectories are increasingly intercepted by the finite axial dimensions of the array.

Tab. 5.1 reports the percentage of detected protons and the ratio of multi-turn protons to the total detected.

As discussed in Chapter 3, the primary source of background in the silicon array is believed to be α particles as a result of multi-nucleon transfer reactions with the carbon nuclei in the target. The cyclotron period, defined in Eq. 2.2, depends solely on the mass-to-charge ratio and the magnetic field strength,

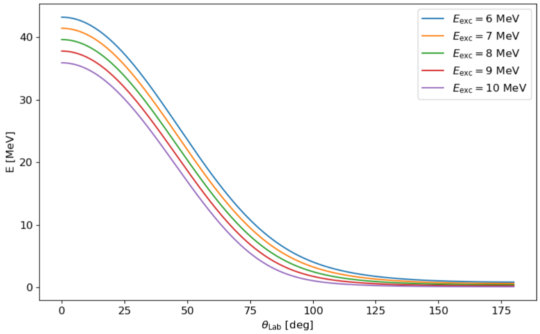

Figure 5.4: Energy as a function of the emission angle in the laboratory frame for protons emitted during the formation of the ^{230}Ac with different excitation energies E_{exc}.

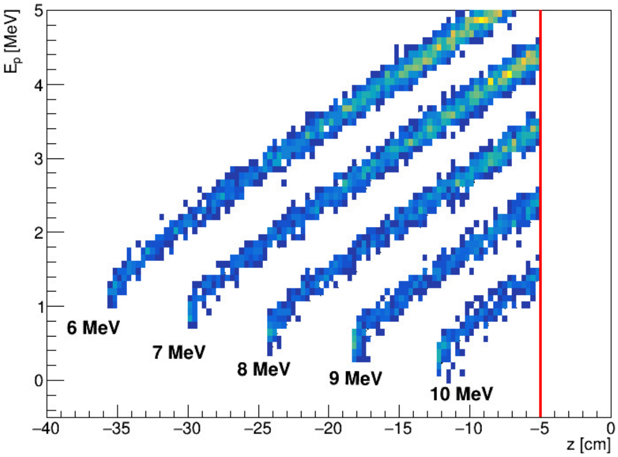

Figure 5.5: Simulated ejectile energies E_p against the positions of proton hits on the array, z, in the laboratory frame considering a silicon array positioned 5 cm from the target and a magnetic field of 2 T, as illustrated by the solid red line. The different diagonals in the plot represent different excitation energies of the formed CN.

independent of the energy or direction of the particle. This would allow for particle identification by measuring the time of flight. A simulated representative time-of-flight spectrum is reported in Fig. 5.7. The first peak near 33 ns corresponds to protons that intercept the detector array at the end of one cyclotron orbit. The second peak, near 66 ns, corresponds to protons execut-

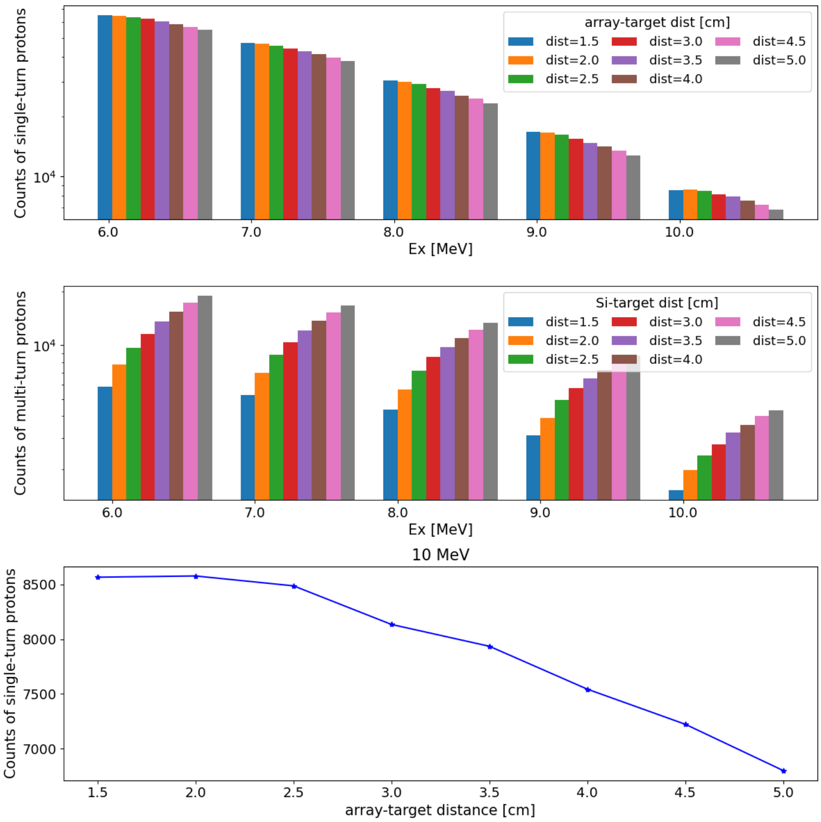

Figure 5.6: Counts distribution of detected single-turn protons (top panel) and multi-turn protons (middle panel) as a function of the distance between the silicon array and the target for various excitation energies of the compound nucleus. The bottom panel highlights the increase in single-turn proton counts at higher CN excitation energies (e.g. 10 MeV) as the silicon array is positioned closer to the target.

ing two cyclotron orbits and particles with a mass-to-charge ratio of $A/q = 2$, namely α particles. In this simulation, a time resolution of 9.1 ns FWHM was considered, which proved sufficient to identify the reaction products of interest. This resolution matches that achieved with the HELIOS silicon-detector array at ANL [65]. The significantly lower time resolution of the silicon array at ISS prevents clear particle identification; therefore, background measurements using a pure carbon target of equivalent thickness will have to be employed to subtract any remaining background as shown in the Fact-Box on page 63.

Fig. 5.7 shows that, even with good time resolution, it is impossible to disentangle two-turn protons from one-turn α particles. As a result, only single-

E_{exc}:	6 MeV		7 MeV		8 MeV		9 MeV		10 MeV	
Distance	Det %	Ratio	Det %	Ratio	Det %	Ratio	Det %	Ratio	Det %	Ratio
2 cm	7.3	0.107	5.4	0.130	3.6	0.158	2.1	0.190	1.0	0.187
3 cm	7.4	0.157	5.5	0.190	3.6	0.235	2.1	0.270	1.1	0.255
4 cm	7.4	0.208	5.5	0.249	3.7	0.300	2.2	0.339	1.1	0.320
5 cm	7.4	0.257	5.5	0.306	3.7	0.364	2.1	0.407	1.1	0.388

Table 5.1: Percentage of detected protons and ratio of multi-turn protons to total detected protons, evaluated at various excitation energies of the compound nucleus and different distances between the silicon array and the target.

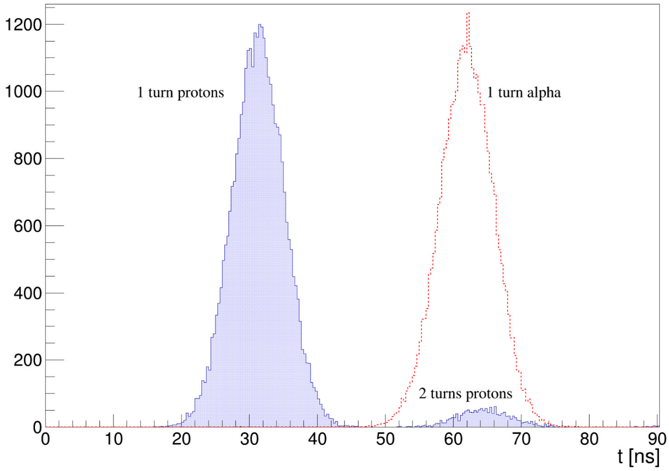

Figure 5.7: Simulated representative time-of-flight spectrum of protons detected in the DSSSDs sensor with an assumed 9.1 ns FWHM resolution (as obtained at HELIOS [2]). Two peaks around 33 ns and 66 ns corresponding to single-orbit protons and α particles as well as double-cycle protons can be distinguished.

turn protons will be considered, which will consequently reduce the statistics. Positioning the silicon array as close as possible to the target is advantageous, as it not only increases the detection of protons from a compound nucleus produced at 10 MeV but, as shown in Tab. 5.1, also lowers the ratio of multi-turn protons to the total number of detected protons. However, due to technical limitations, the minimum achievable distance from the target is about 2 cm. Assuming a magnetic field of 2 T, the optimal longitudinal range for the DSSSDs extends from 20 to 521.5 mm upstream of the target.

Multi-turn protons can be physically removed by placing a cylindrical obstruction, known as a multi-turn "silencer", at the end of the silicon array. This component ensures that protons with smaller pitch in their helical orbits collide with the silencer before reaching the active part of the detector.

However, this method is ineffective against single-turn α particles. The diameter of the silencer is approximately 16 mm, while its length is customizable. A schematic representation of the multi-turn silencer is shown in Fig. 5.8.

If multi-turn protons are blocked so that only single-turn protons reach the array, the expected distribution would resemble the one presented in Fig. 5.9. In this case, the array is positioned 2 cm from the target, and the figure illustrates how the range along the $z-$axis varies for protons emitted together with different excitation energies of the compound nucleus.

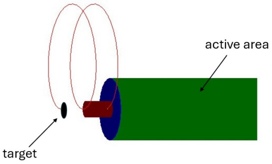

Figure 5.8: Schematic illustration of the multi-turn proton silencer placed at the very end of the silicon array.

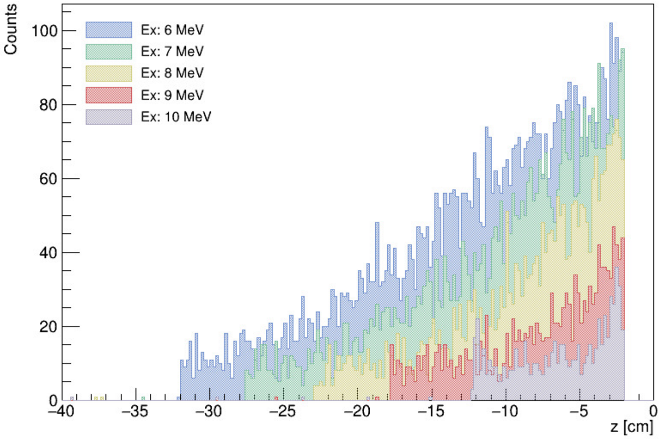

Figure 5.9: Expected distribution of protons detected by the array when multi-turn protons are blocked. The array is positioned 2 cm from the target.

Finally, Fig. 5.10 presents a typical reconstructed excitation-energy spectrum. This spectrum is derived from simulated deposited energy and hit positions in the silicon array, capturing ejected protons produced in the ^{229}Ac(d,p) reaction with an incoming beam energy of 8 MeV/u. The excitation energy, assuming distinct doorway-state energies at 6, 7, 8, 9, and 10 MeV, is extracted according to Eq. 2.10.

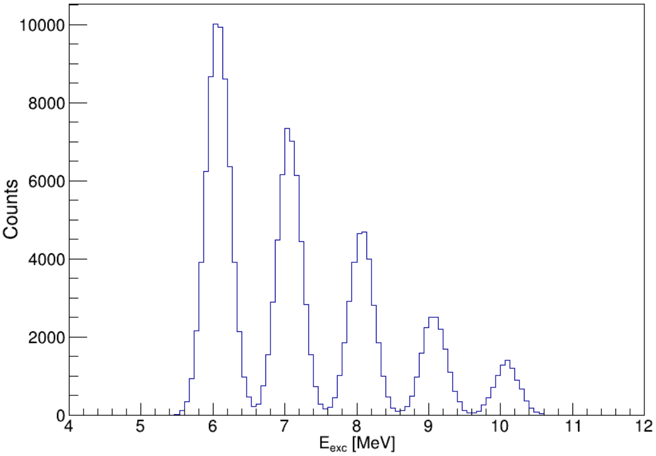

Figure 5.10: Reconstructed excitation energy spectrum of the compound nucleus extracted from the simulated deposited energy of protons in the position-sensitive silicon array, as given by Eq. 2.10. The protons are emitted assuming the ^{229}Ac(d,p) reaction with an incoming beam energy of 8 MeV/u.

Background subtraction and required statistics

To address background signals indistinguishable by timing resolution, measurements with a pure carbon (C) target are needed, as was done in the proof-of-principle ^{238}U experiment [2]. The carbon spectra, containing contributions such as protons resulting from interactions with the carbon, were scaled to match those from the CD$_2$ target in the region below the ground state ($E_x < 0$ MeV) and then subtracted, as shown in Fig. 5.11.

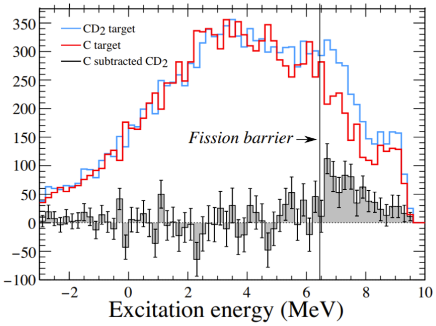

Figure 5.11: Excitation energy spectra of ^{239}U gated on the detection of one or two fission fragments. Spectra for data acquired with both the CD$_2$ and the C target as well as their difference (grey) are illustrated. Figure from [2].

The absolute values of the two spectra determine the size of the error bars in the subtracted data. Carbon data must be scaled so that the contributions from both the CD$_2$ and C datasets are balanced. Analyzing the figure, it is reasonable to assume that, in the bin above the fission barrier for the different runs, the event counts are as follows:

$$\text{CD}_2 : 300 \text{ events},$$
$$\text{C} : 200 \text{ events},$$
$$\text{Fission} = \text{CD}_2 - \text{C} = 100,$$
$$\text{Relative error} = \frac{\sqrt{300+200}}{100} = 0.224.$$

In this experiment, no timing discrimination was used for background reduction. Now, suppose 50 % of the background is due to α particles and 50 % due to protons, and a timing cut can be applied. Since α particles and protons have different cyclotron times, half of the background would be removed. Under such conditions, the relative error reduces to:

$$\begin{aligned}\mathrm{CD_2} &: 200 \text{ events},\\ \mathrm{C} &: 100 \text{ events},\\ \text{Fission} &= \mathrm{CD_2} - \mathrm{C} = 100,\\ \text{Relative error} &= \frac{\sqrt{200+100}}{100} = 0.173.\end{aligned}$$

By comparing these two scenarios, we estimate the additional statistics required to achieve the same relative error of 0.173 as in the case with timing discrimination:

$$\frac{0.173}{0.224} = 0.7723 = f. \tag{5.1}$$

The statistics multiplication factor, m, is then calculated as:

$$m = \frac{1}{f^2} = 1.67. \tag{5.2}$$

This calculation indicates that 1.67 times more statistics are needed to achieve the same relative error with and without the timing cut.

5.3 Detection of fission fragments in inverse kinematics

In Chapter 4, the ^{229}Ac(d,pF) reaction at 8 MeV/u was chosen as the test case for the first direct measurement of the fission barrier height in inverse kinematics using the novel approach described in Chapter 3. The ^{230}Ac compound nucleus, formed in the reaction, will travel forward with an energy approximately matching that of the beam. If fission occurs, the resulting fragments will be emitted in the forward direction within a cone, with an opening angle depending on the beam energy and the transverse momentum of each fragment.

Fig. 5.12 shows the post-scission and post-neutron mass and charge distribution of fission fragments from ^{230}Ac, as calculated by the GEF model. Asymmetric fission is predicted, with fragment charges in the range $30 \leq Z \leq 60$ and masses between $80 \leq A \leq 150$. In inverse kinematics, the conservation of momentum, together with the mass difference between the light and heavy fragments, results in their emission at different opening angles in the laboratory frame, as shown in Fig. 5.13. This leads to the formation of two distinct rings in the intensity distribution for fission fragments detected downstream on an

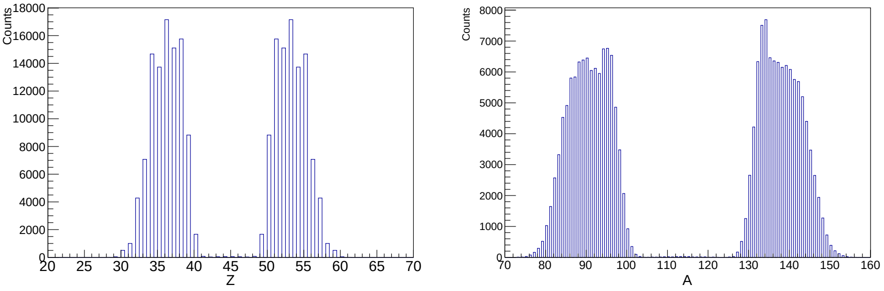

(a) **(b)**

Figure 5.12: Charge (panel a) and post-neutron mass (panel b) distributions of the fission fragments from 10^5 simulated events using the GEF model for ^{230}Ac at an excitation energy of $E_{\mathrm{exc}} = 7$ MeV above the ground state.

$x - y$ plane, illustrated in Fig. 5.14.

In the proof-of-principle ^{238}U fission experiment at ANL, asymmetric fission fragments were detected using a set of four detection arms positioned 1 m downstream of the target, with two arms at 15° and two at 10° to maximize the acceptance of light and heavy fragments. Each arm consisted of a position-sensitive Multi-Wire Proportional Counter (MWPC) followed by an axially segmented Fission Fragment Identification (FIFI) Bragg detector. On an event-by-event basis, the Bragg detector provided the total and specific energy loss of any detected fragment, while the MWPCs recorded their position at the entrance of the Bragg detectors. Fig. 5.15 illustrates the experimental setup used. Fig. 5.16 presents the simulated acceptance for detecting fission fragments with the aforementioned FIFI detectors considering the ^{238}U(d,pF) reaction at 8.6 MeV/u.

Although the intrinsic efficiency of each detection arm was close to 100 %, due to their limited size the geometric efficiency for detecting the fission fragments was limited: approximately $\sim$ 10 % for the detection of at least one fission fragment and about $\sim$ 1 % for the coincident detection of light and heavy fragments [2].

As previously discussed, the most effective method for detecting emitted fission fragments, given their kinematics, is to use a CD-shaped detector centered along the beam axis. This design includes a hole that allows the unreacted beam to pass through. By adjusting the distance of the detector from the target, the solid angle it covers can be optimized to maximize detection efficiency for both fission fragments. In these simulations, a Micron DSSD S3 model is considered, featuring an inner radius of 11 mm and an outer radius of 35 mm [43]. In Fig. 5.17, the geometric efficiency curves for detecting only the light fragment,

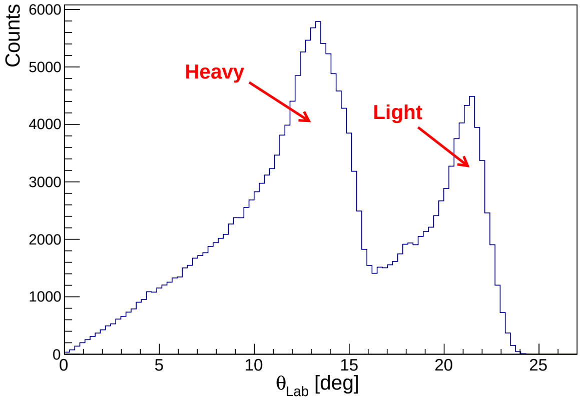

Figure 5.13: Angular distributions of fission fragments from ^{230}Ac simulated by GEF boosted with an incoming beam energy of 8 MeV/u. The two distinct peaks at approximately 13° and 21° correspond to heavy and light fission fragments, respectively. In these simulations, a beam spot with vanishing dimensions in the $x-y$ plane is considered.

the heavy fragment, or both in coincidence are presented as a function of the distance of the detector from the target. Considering an incoming ^{229}Ac beam at 8 MeV/u, at a distance of 8 cm downstream from the target, the efficiency in detecting the light fragment is 92%, whereas for the heavy fragment it is 82%. The most significant result, however, is the efficiency for coincident detection of both fragments which lies around 80%, confirming that this detection system achieves a much improved detection efficiency. A distance of 8 cm has been selected as the optimal position for placing the fission fragment detector. Coincident detection of the two fission fragments is achievable by utilizing a detector segmented into rings and sectors, which allows for precise measurements of their azimuthal angle differences. For fission events, this angular difference is expected to be 180° because the fragments are emitted back-to-back in the CM, resulting in opposing transverse momenta. Fig. 5.18 illustrates the correlation in the azimuthal angles at which the light and heavy fission fragments are emitted.

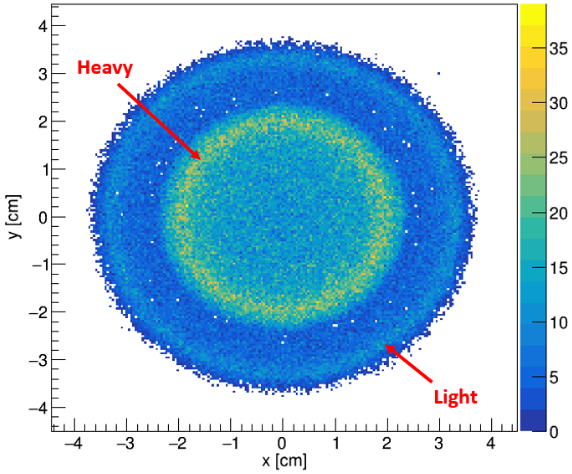

Figure 5.14: Simulated intensity distribution of fission fragments on the $x - y$ plane 10 cm downstream from the target, depicting the two distinct rings corresponding to heavy and light fragments resulting from the fission of ^{230}Ac with $E_{exc} = 7$ MeV above the ground state. In these simulations, a beam spot with vanishing dimensions in the $x - y$ plane is considered.

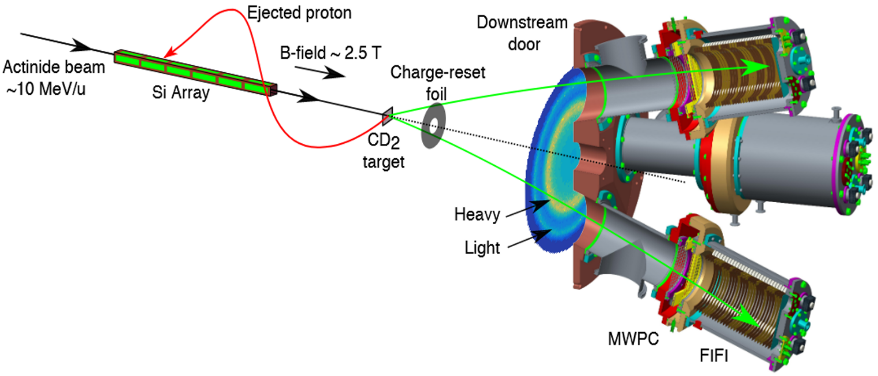

Figure 5.15: Illustration of the experimental arrangement within the HELIOS solenoidal magnet, depicting the trajectories of protons and fission fragments from a single (d,pF) event. A cross-section of the FIFI detectors mounted on the rear door of the magnet is presented, with three of the four detectors visible. The simulated distribution of fission fragments is also included. Figure from Ref. [66].

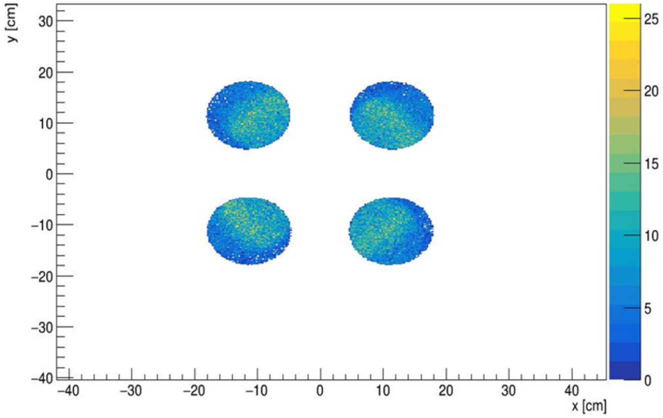

Figure 5.16: Simulated $x - y$ acceptance for detecting fission fragments with the FIFI detectors (see Fig. 5.15) in the ^{238}U(d,pF) reaction at 8.6 MeV/u. The acceptance is limited by the active areas of the detectors.

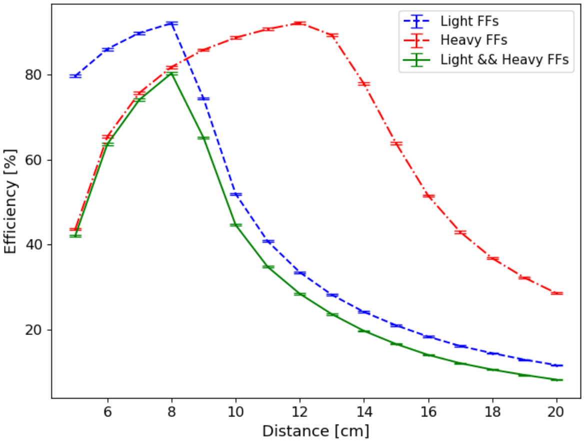

Figure 5.17: Geometric efficiency curves for detecting fission fragments as a function of the distance between the detector and the target. The solid green line represents the efficiency of coincident detection of both light and heavy fragments. The red dot-dashed line indicates the efficiency for detecting only the heavy fragment, while the dashed blue line represents the efficiency for detecting only the light fragment. These simulations assume a fissioning ^{230}Ac nucleus with $E_{\mathrm{exc}} = 7$ MeV. Error bars represent the statistical uncertainty of the Monte Carlo model.

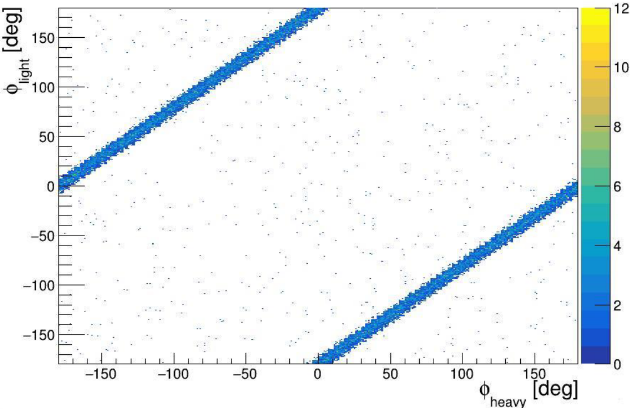

Figure 5.18: Correlation between the azimuthal angles of emitted light and heavy fission fragments, showing the expected 180° angle difference that arises from their back-to-back emission in the CM frame.

5.4 Beam intensity measurement inside solenoidal spectrometers

When determining fission probabilities, a normalization of the number of measured fission events is needed to obtain absolute cross-sections. This can be done only when the number of incoming beam ions that hit the target, and the area density of target nuclei, are known. At ISS, in order to measure the incoming beam intensity elastically scattered deuterons from the target are measured. This task is usually carried out by the so-called luminosity detectors which are devices conceived specifically to measure the rate of collisions between the beam ions and the target.

Typical differential cross-sections and energy distributions of such scattered deuterons are reported in Fig. 5.19. These distributions were obtained using the FRESCO [67] and LISE++ [68] programs for an incoming ^{229}Ac beam at 8 MeV/u on a CD_2 target with a thickness of 1 mg/cm^2. Due to the inverse kinematics of the reaction, very few scattered deuterons are emitted at forward angles close to 0°, where particles exhibit their maximum kinetic energy, approximately 31 MeV. The majority of scattered deuterons are emitted at angles near 90° with significantly lower energies (approaching 0 MeV), preventing most from escaping the target and making their detection impossible. Therefore, adjustments to the luminosity detector configuration are necessary to ensure the detection of a sufficient number of deuterons with enough energy to be measured.

Because of momentum conservation, deuterons cannot be scattered at back-

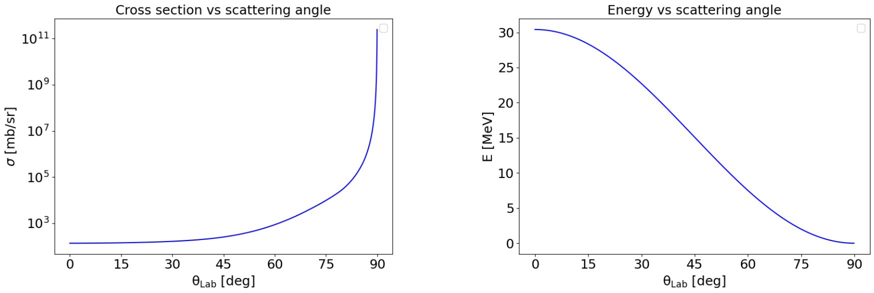

(a) **(b)**

Figure 5.19: (a) Differential cross-section as a function of scattering angle in the laboratory frame for elastically scattered deuterons from an incoming beam of ^{229}Ac at 8 MeV/u provided by FRESCO. (b) Energy as a function of scattering angle in the laboratory frame. Most deuterons are scattered at angles where their energies are very small.

ward angles in inverse kinematics. Therefore, the luminosity detector must be positioned downstream of the target.

At ISS, elastically scattered deuterons from the target are usually detected with a luminosity detector mounted on the beam axis commonly referred to as the ELUM[2]. It consists of a double-sided silicon detector (Micron Semiconductor S1) placed on the beam axis downstream from the target (Fig. 5.20). It has an annular shape and is shielded by a 12.8 mm thick aluminum annulus and an aluminum tube passing through the center of the annulus. Therefore, particles can only reach the detector by passing around the blocker.

This is required to prevent unwanted particles, which are not needed or even disturb the measurement of the beam current, from reaching the detector and to select only a limited and well-defined range of scattering angles of the emitted deuterons. The distance between the ELUM detector and the target can be changed to optimize the acceptance for deuterons emitted at different angles. Just to provide an example, Fig. 5.21 displays simulations of the ELUM response for experiment IS675 aimed at measuring the $\mathrm{d}(^{61}\mathrm{Zn},\mathrm{d})^{62}\mathrm{Zn}$ transfer reaction with an incoming beam energy of 7.5 MeV/u. In this case the open distance between the detector and the shield was set to 13.42 mm, whereas the target-S1 distance was 268 mm resulting in an acceptance for scattered deuterons with trajectories in the angular range $73.33° \leq \theta_{\mathrm{lab}} \leq 75.14°$ for single-turn trajectories and $77.9° \leq \theta_{\mathrm{lab}} \leq 80.5°$ for double-turn trajectories. For these simulations, a dead layer of 0.5 μm in the luminosity detector has been considered along with the primary source of background in the ELUM,

---

[2] This acronym stands for "Elastic LUminosity Monitor".

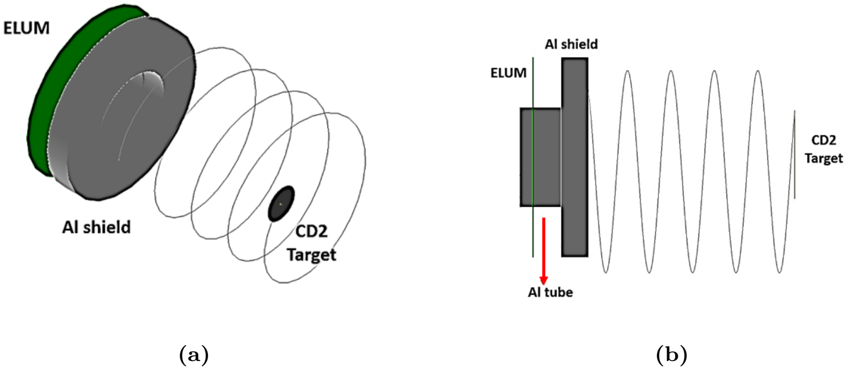

Figure 5.20: Schematic of the currently used ELUM annular detector at ISS for the detection of elastically scattered deuterons. The direct path between the target and the detector is shielded such that only deuterons scattered in a specific angular range can hit it after traveling helix-shaped trajectories. Note that the trajectory depicted in the figure does not meet the requirements for hitting the ELUM detector.

which specifically stems from the scattering of ^{12}C present in the CD_2 target.

Given that the position of the peaks in the ELUM spectra depends on the scattering angle and that the cross-section for carbon emission as a function of the scattering angle mainly affects the height of the peaks rather than their position, the plain Rutherford cross-section has been considered in the simulations, as it can be easily simulated by `ggland`[3]. The simulation results turn out to be in good agreement with the experimental data.

While this setup has been widely used in numerous experiments at ISS at CERN and HELIOS at ANL to effectively determine the beam luminosity, it is not ideal for experiments investigating the fission barrier height of short-lived nuclei in inverse kinematics. The boost of the reaction products in the positive z direction causes both fission fragments to move forward, with an opening angle that depends on the beam energy and the transverse momentum of the fission fragments. For instance, in the case of ^{229}Ac + d with an incoming energy of 8 MeV/u, the maximum aperture of the cone is $\sim 22.6°$. Assuming that the fission fragment detector is placed 14 cm from the target, it is evident that the aforementioned ELUM configuration, with its shielding, would block a significant portion of the fission fragments from reaching the silicon CD-shaped[4]

---

[3] In practice, the Rutherford cross-section formula has to be adapted for inverse kinematics, taking into account the finite masses of both, the beam and the target.

[4] A Compact Disc (CD) is an optical disc, normally disc-shaped, that was developed in 1982 for storing and playing digital audio but was later adapted for general data storage as well, with a typical capacity of about 700 MB.

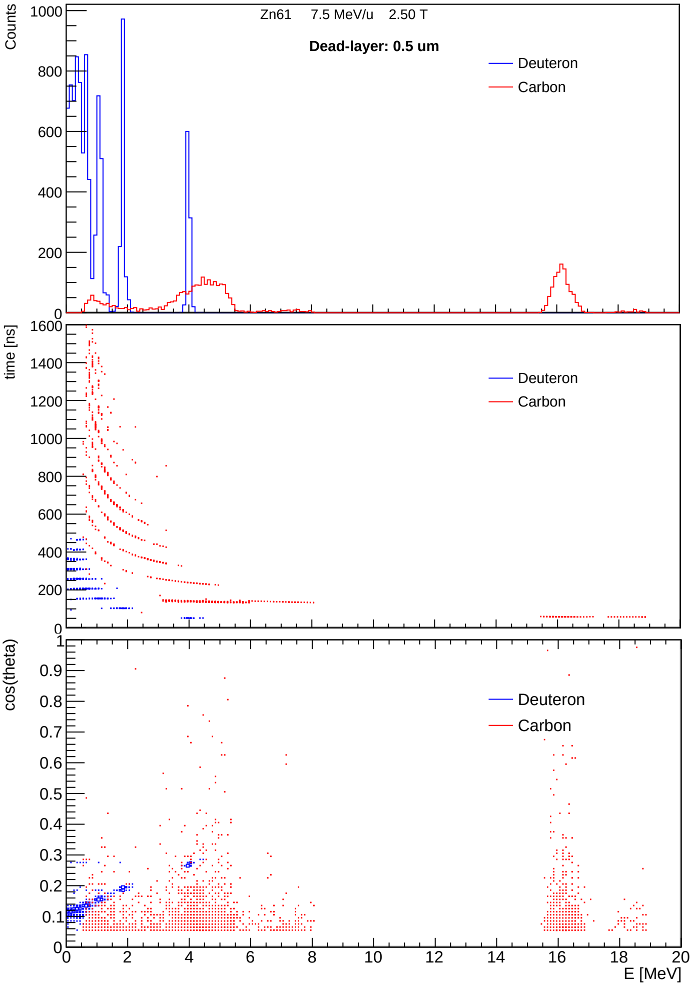

Figure 5.21: Expected number of counts for the ELUM luminosity detector for the IS675 experiment for an incoming beam with luminosity 3 b^{-1}. The blue histogram represents the yield from elastically scattered deuterons, while the red histogram shows the yield from undesired background reactions due to elastically scattered carbon in the target. The upper plot displays the energy spectra for deuterons and carbon, the middle plot shows the correlation between simulated time-of-flight and energy deposited in the detector, and the lower plot illustrates the angular coverage for deuterons and carbon as a function of deposited energy.

$\Delta E - E$ detector, as shown in Fig. 5.22.

To address this issue, the initial solution considered was to switch the positions of the ELUM beam monitor and the fission fragments detector, as depicted in Fig. 5.23, which would entail placing the $\Delta E - E$ telescope in front of the ELUM detector.

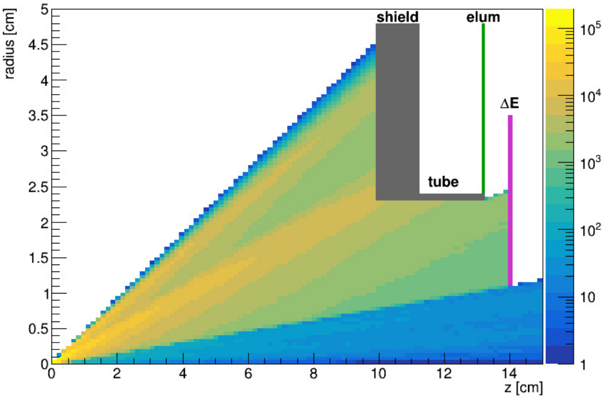

Figure 5.22: Fission fragments trajectories resulting from the ^{229}Ac(d,pF) reaction at 8 MeV/u in a 2 T magnetic field. The color gradient illustrates how the shielding (in grey) of the ELUM detector (in green) prevents most of both heavy and light fission fragment trajectories from reaching the ΔE-E telescope detector. Only the ΔE layer is shown (in magenta).

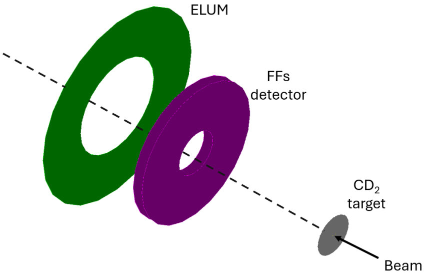

Figure 5.23: Schematic view of an alternative setup. Here the fission fragment detector drawn in magenta acts as an active shield for the ELUM detector in green.

Although this approach effectively addresses the issue to avoid blocking the fission fragment trajectories, it does not perform as well in terms of signal-to-background ratio, as illustrated in Fig. 5.24. The standard ELUM setup lacks measurement of position (e.g. radial), and the peaks of detected deuterons are obscured by lower-energy background events.

These considerations highlight the need for an innovative approach to measuring beam intensities within solenoidal spectrometers, optimized for studies of fission barriers in inverse kinematics. A suggestion for an off-beam-axis monitor detector made of position-sensitive silicon plates has been independently proposed by B. Kay at ANL and A. Kawęcka, locally. In the following section, the performance of this new luminosity detector setup, referred to as LUME, will be investigated for both fission studies and other experiments. As will be demonstrated, this approach promises improved results in terms of detection efficiency and signal-to-background ratio.

5.5 LUME: new luminosity detectors

To determine the optimal configuration of the LUME detector for measuring elastically scattered deuterons, different geometries of four position-sensitive silicon diode strips, each with an active area of $50 \times 10\,\mathrm{mm}^2$, were investigated. The operational principle of Position-Sensitive Detectors (PSD) is illustrated in the Fact-Box on page 79.

In each configuration, the silicon sensors are positioned parallel to the solenoid axis and are spaced 90° apart around the beam axis ($z-$axis). The key difference between the configurations lies in the rotation of the normal of the silicon strips with respect to the $z-$axis, defined by the ϕ angle. One example of these configurations is schematically drawn in Fig. 5.25.

Not only does the orientation of the silicon sensors affect the efficiency, but the position of the detectors also plays a significant role. Therefore, simulations were performed, varying the distances of the plates from both the target and the beam axis, to determine the optimal placement for detecting the majority of scattered deuterons. Also, the rotation around both the local $z-$axis and around $x-$axis were varied.

The detection efficiency ϵ is expressed in terms of the number of detected deuterons per incoming ion and it is calculated as follows:

$$\epsilon = \frac{N_{\mathrm{det}}}{N_{\mathrm{simul}} \cdot \eta} \tag{5.3}$$

where $\mathrm{N}_{\mathrm{det}}$ is the number of deuterons detected in any one of the four silicon detectors, and $\mathrm{N}_{\mathrm{simul}}$ is the total number of simulated events (10^6). The multiplication factor η represents the number of incoming ions required to produce a single event, specifically one elastically scattered deuteron from the target. This quantity takes into account the beam intensity I per event (expressed in $1/cm^2 \cdot mol$), the target thickness ρ (in g/cm^2), the molecular mass of the target

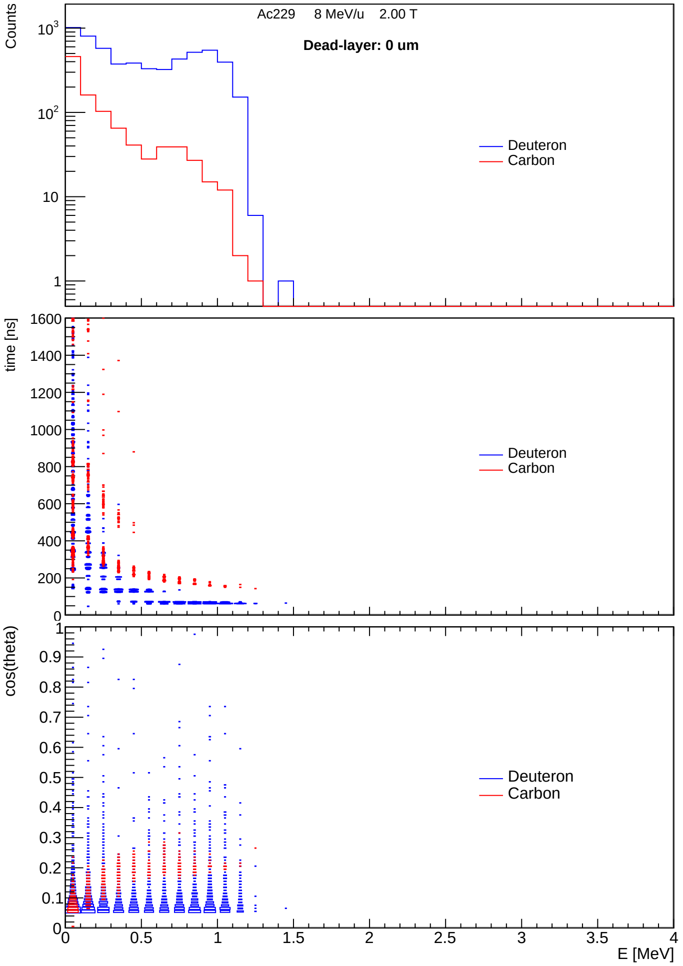

Figure 5.24: Simulated yields for the ELUM luminosity detector in an alternative geometry, where the fission fragment telescope acts as an active shield for the ELUM detector. The blue histogram represents the yield from elastically scattered deuterons, while the red histogram shows the yield from undesired background reactions caused by elastically scattered carbon in the target. From the energy spectra (upper plot), the time-of-flight and energy correlation (middle plot), and the angular coverage as a function of energy (lower plot), it is clear that the carbon yields lie directly underneath the deuteron distribution, making it impossible to achieve a clear separation. For these simulations, an incoming beam of ^{229}Ac is assumed to impinge on a CD_2 target at 8 MeV/u, with no dead-layer considered in the luminosity detector.

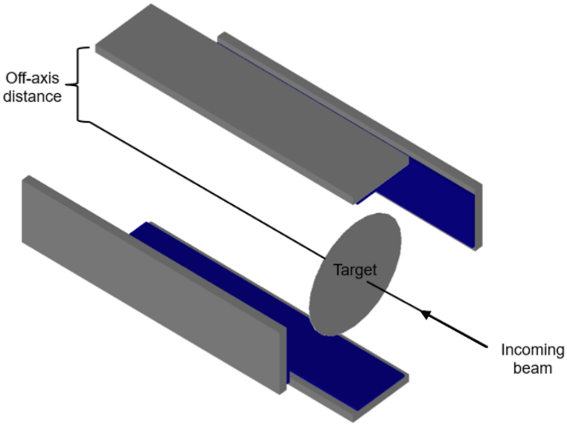

Figure 5.25: One of the configurations simulated for the LUME detector. The four silicon sensors sit parallel to the superconducting solenoid axis with the active area surface facing the beam axis while each sensor is rotated by $\phi = 90^\circ$ relative to the beam axis. The PCB layers, on which the silicon plates are mounted, and the target disk are drawn in grey.

$\mathrm{M}_{\mathrm{tar}}$ (g/mol) and the target atoms per molecule N:

$$\eta = \frac{I \cdot \mathrm{M}_{\mathrm{target}}}{\rho \cdot N \cdot \sigma_{\mathrm{int}}}. \tag{5.4}$$

Here σ_{int} represents the integrated Rutherford cross-section, in b, over the sampled angular range. The contour plot in Fig. 5.26 illustrates how the detection efficiency of scattered deuterons varies with different distances from the target and the beam axis of the four silicon detectors of the LUME monitor. It is clear that the closer the silicon plates are to the beam axis and the target, the higher the efficiency in detecting deuterons. However, there are technical limitations, such as the presence of the target support, which constrain the minimum distance at which the sensors can be positioned.

It is expected that the background in the luminosity detector originates from signals from elastically scattered carbon. Therefore, to optimize the design of LUME, it is essential not only to maximize the detection efficiency of the detector for scattered deuterons but also to improve its signal-to-background ratio. For example, Fig. 5.27 illustrates the distribution of elastically scattered carbon and deuterons in the laboratory frame in a $x - z$ plane. These simulated distributions consider different incident beams on a CD_2 target at various beam

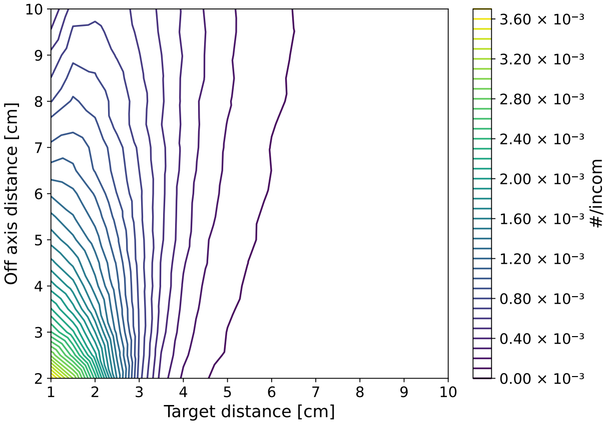

Figure 5.26: Contour plot illustrating how the detection efficiency (calculated as the number of detected deuterons per incoming ion and unit (μg/cm^2) target thickness, described in Eqs. 5.3 and 5.4) of elastically scattered deuterons varies with the target and off-axis distances for the LUME detector. These simulations assume a 0.5 MeV energy threshold.

energies, reflecting the different beam-target combinations considered in experiments actually conducted at ISS.

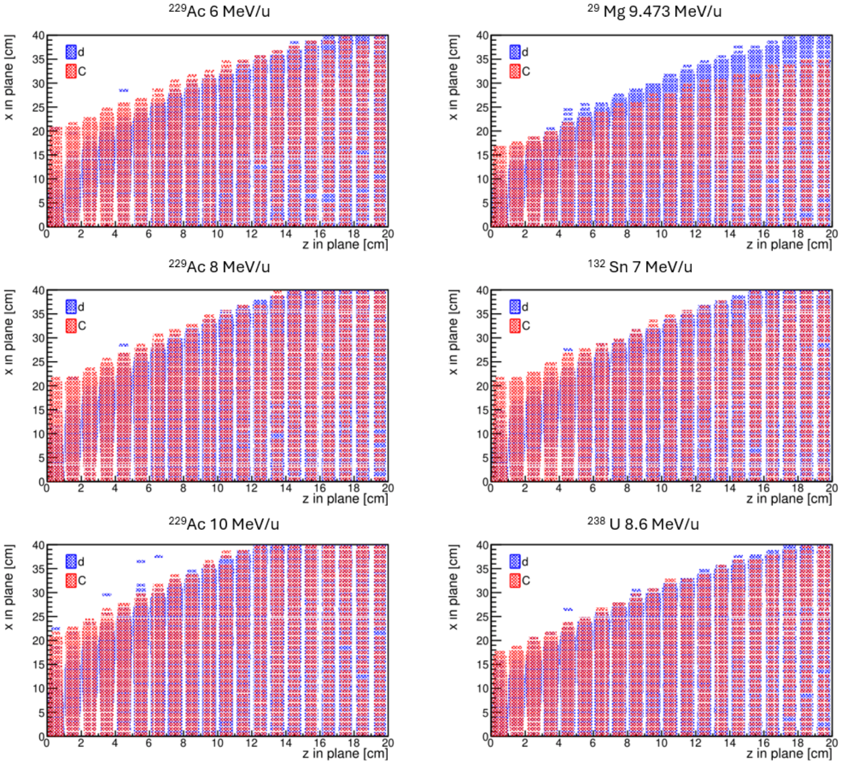

Figure 5.27: Distribution of elastically scattered carbon and deuterons from a CD_2 target in the $x-z$ plane in the laboratory frame. The particles have followed various trajectories after emission at random angles (azimuthally uniform and polar distribution according to Rutherford cross section). The first column displays the same beam at different energies, while the second column illustrates different beams at varying energies. The results highlight the differences in hit distributions for the varying beam conditions.

Position-Sensitive Detectors with resistive readout

In the Position Sensitive Detectors used for LUME, the position determination relies on charge division along a resistive layer. When a charged particle interacts with the silicon, it excites electron-hole pairs releasing charge that moves across the resistive layer to the electrodes. The amplitude of the signals collected at each electrode is proportional to the amount of charge reaching it, which in turn depends on the position of the interaction along the detector. Each PSD generates three signals: the total energy output from a contact on the back side of the detector, E, and two signals, X_A and X_B, from contacts on the front side at the two far ends of the strip, as depicted in Fig. 5.28.

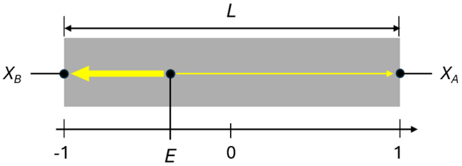

Figure 5.28: Schematic of a Position Sensitive Detector (PSD). A charged particle interacts with the silicon, generating a charge that spreads across the resistive layer. The signals collected at the back contact (total energy signal E) and the front contacts at each end of the strip (X_B and X_A) are used to determine the position of the interaction along the detector.

The hit position u along the strip of the PSD can be calculated as follows:

$$u = \frac{X_B - X_A}{E}, \qquad u \in [-1, 1]. \tag{5.5}$$

Nominally, $\mathrm{E} = \mathrm{X_A} + \mathrm{X_B}$. When a particle hits the center of the PSD, the signals X_B and X_A have equal amplitudes. However, if the particle hits very close to one edge of the strip — for example, near edge B — then the X_B signal will have a higher amplitude, while the corresponding X_A signal will be smaller. Depending on the electronic settings, X_A could in this case fall below the energy threshold, resulting in an incomplete hit.

As defined in Eq. 5.5, $u \in (-1, 1)$, however, the absolute hit position on the strip can be calculated with respect to the target distance as:

$$z = \frac{L}{2} u + d_{\mathrm{target}}, \tag{5.6}$$

where L is the length of the PSD, and d_{target} is the distance between the center of the active area of the silicon wafer and the target.

5.5.1 Optimizing the target distance

To determine the optimal placement distance for the position-sensitive detector (PSD), the LUME detection efficiency variation was investigated as a function of target distance, while keeping the beam axis distance fixed. The resulting efficiency curves, shown in Fig. 5.29, correspond to beam axis distances of 4 cm and 7.5 cm.

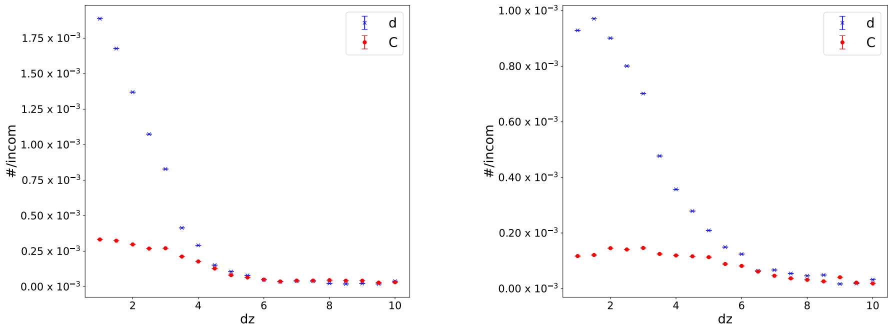

(a) Off-axis distance = 4 cm.

(b) Off-axis distance = 7.5 cm.

Figure 5.29: Efficiency curve for deuteron (in blue) and carbon (in red) detection by the silicon position-sensitive sensor in the LUME detector as a function of target distance (dz), with two fixed distances from the beam axis.

An important clarification regarding these simulations is that the term "target distance" refers to the distance from the center of the PSD to the target. Given that the detector measures 50 mm in length, a target distance of less than 25 mm indicates that the PSD encompasses a range in the $z-$direction that extends behind the target. As a result, a portion of the detector would not be utilized, since deuterons are not emitted at scattering angles greater than 90°. It is worth noting that the detection efficiency is higher at distances shorter than 2.5 cm. This might seem counterintuitive, as a smaller portion of the detector extends beyond the target position at a distance of 2.5 cm, suggesting that a greater fraction of the detecting area would be available for detecting scattered deuterons in the forward direction. However, the explanation is simple:

At a target distance of 2.5 cm, one edge of the PSD aligns directly above the target, where most low-energy deuterons are emitted. As a result, signals induced on the opposite edge may fall below the threshold, which is set at 0.5 MeV in this case.

As expected, increasing the distance from the beam axis leads to a general decrease in detection efficiency, as shown in the right-hand plot where the beam axis distance is 7.5 cm, compared to the efficiency at 4 cm shown in the left plot. However, for a beam axis distance of 7.5 cm, the efficiency with the detector positioned 1 cm along the forward direction is actually lower than at 2 cm. This phenomenon can be attributed to the fact that low-energy deuterons are predominantly emitted at angles close to 90°. As the detector moves further from the beam axis, the radius of the helical trajectories of these deuterons may fall short of reaching the detector, and thus do not influence the difference.

Last but not least, there is another geometrical constraint that needs to be considered. It is essential to ensure that the arrangement of the LUME setup does not interfere with the trajectories of fission fragments moving in the forward direction. Since the ideal distance from the target to place the S3-based $\Delta E - E$ telescope for detecting fission fragments is 8 cm, there is limited flexibility in adjusting the target distance. Taking into account the target support and the mechanical risks associated with getting too close, one of the few viable options is to position the LUME PSDs at 4.2 cm from the target, measured from the detector center. Target distances greater than the placement of the fission fragment telescope are not considered, as the ΔE-E telescope would shadow the luminosity detector.

5.5.2 Optimizing the off-axis distance

Given the limited flexibility in adjusting the target distance, the next step is to determine the optimal positioning of the PSDs relative to the beam axis. Figure 5.30 shows efficiency curves for detecting deuterons and carbon at various distances from the beam axis, with the target distance fixed at 4.2 cm. Notably, for distances greater than 7 cm, the deuteron efficiency curve exhibits a plateau and a more pronounced separation from the carbon distribution. Choosing a position within this plateau region is advisable, as efficiency variations are expected to be minimal even if the PSDs are not perfectly aligned. A beam axis distance of 7.5 cm is therefore selected based on these considerations.

5.5.3 Evaluating possible detector inclination

One last degree of freedom to consider is the potential rotation of the silicon detectors at a certain angle relative to the beam axis and the plane perpendicular to the beam axis. Assuming a target distance of 4.2 cm and an off-axis distance of 7.5 cm, Fig. 5.31 demonstrates that maintaining no rotation around the x and z axes is the optimal configuration. This geometry not only maximizes deuteron detection efficiency but also increases the separation from the carbon distribution, as it will be shown later in this chapter. Furthermore, a near-zero rotation avoids the steeper regions of the efficiency distribution, thereby reducing sensitivity to potential detector misalignments. The error bars shown represent statistical uncertainties only, which in this case, are smaller than the marker size.

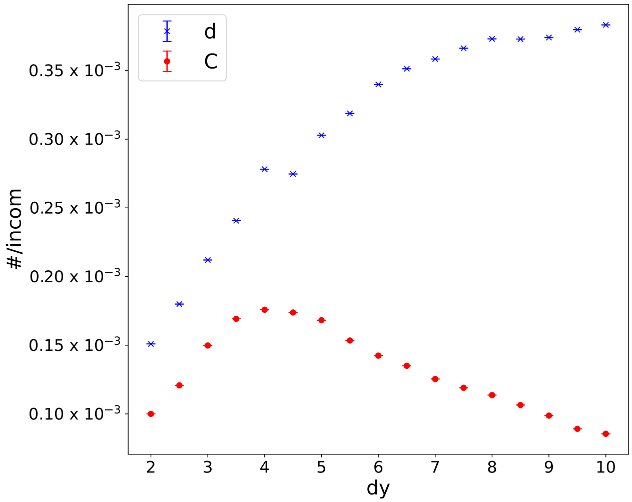

Figure 5.30: Efficiency curves for deuteron (blue) and carbon (red) detection as a function of distance from the beam axis (dy), with the target position fixed at 4.2 cm. For off-axis distances beyond 7 cm, the deuteron curve shows a plateau and the carbon curve decreases, indicating a stable region for PSD placement with minimal sensitivity to alignment variations.

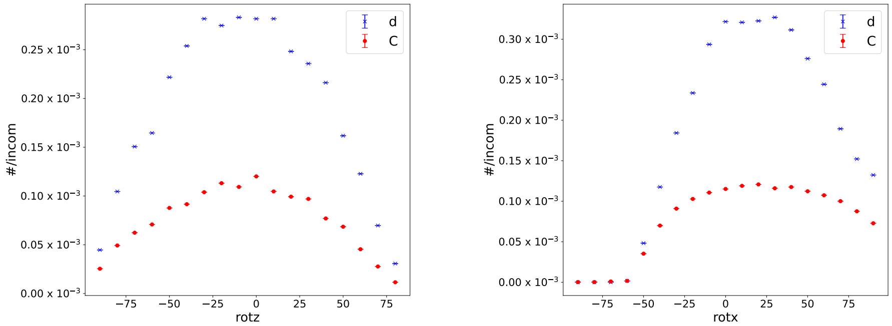

(a) Rotation around the beam axis (rotz).

(b) Rotation around the $x-$axis (rotx).

Figure 5.31: Efficiency curves for deuteron (in blue) and carbon (in red) detection by the silicon position-sensitive sensor in the LUME detector are shown for rotated detectors. Panel **a** illustrates the variation with an inclination with respect to the beam axis (rotz), while the panel **b** shows the effect of rotation (rotx) around the $x-$axis, with the PSDs positioned 7.5 cm from the beam axis and centered 4.5 cm from the target.

A rotation around the $y-$axis was excluded from these simulations to reduce the degrees of freedom and minimize the risk of misalignment, which would complicate the calibration. Mechanically, such a setup would also be challenging to assemble with precise alignment. Moreover, introducing a rotation around the $y-$axis would add an additional degree of uncertainty in reconstructing the particle hit position in the laboratory frame from the hit information provided by the detector, as the detector axis would no longer remain parallel to the beam axis. In Fig. 5.32, the meaning of rotations around the x, y, and z axes is illustrated.

(a) Front view: rotation around the $z-$axis. The beam enters the plane.

(b) Side view: rotation around the $x-$axis.

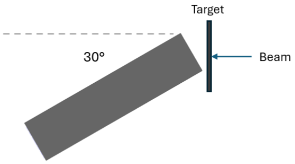

(c) Top view: rotation around the $y-$axis.

Figure 5.32: Schematic illustration of the three different rotations around the z, x, and y axes, in order. The beam direction is indicated, and only one of the four PSDs is shown in these examples.

In summary, based on the discussion above, the optimal configuration for the LUME monitor is to position the PSDs 7.5 cm from the beam axis, with their centers located 4.5 cm from the target. The active sides of the plates face the beam axis and are aligned parallel to it. The four plates are rotated 90° around the beam axis relative to each other, each facing the beam axis. Given this geometry, the simulated response of LUME is shown in Fig. 5.33, for a beam of ^{229}Ac at 8 MeV/u and a CD_2 target of 1 mg/cm^2 thickness. The signal-to-background ratio is significantly improved compared to the current configuration. The deuterium line is clearly distinguishable from the carbon

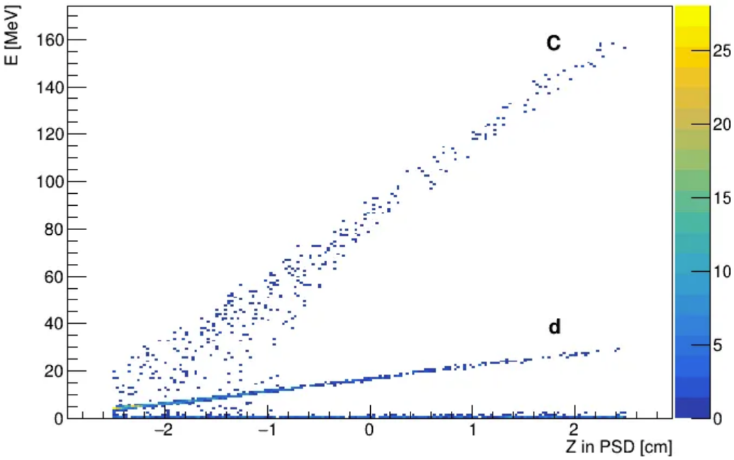

Figure 5.33: Simulated energy deposition and hit positions in the LUME setup, with the PSDs positioned 7.5 cm from the beam axis and their centers located 4.5 cm from the target. The active sides of the plates face the beam axis and are aligned parallel to it. The deuteron line is clearly distinguishable from the carbon line. The counts at very low energies originate from multi-turn carbon and deuteron hits.

line. The smearing of the lower-energy carbon line is due to greater energy loss of the lower-energy carbon nuclei within the target. This effect could be mitigated by reducing the target thickness, provided that experimental conditions (such as reaction rate and beam intensity) allow it.

5.6 Alpha sources simulations

This section presents the simulations of detector responses to the spectra emitted by the four α-emitters commonly used at ISS, which are listed in Section 5.6 below.

Source	Half-life (y)	Energy (keV)
^{148}Gd	86.9	3183
^{241}Am	432.6	5486, 5443, 5388
^{239}Pu	$2.4 \cdot 10^4$	5157, 5144, 5105
^{244}Cm	18.112	5805, 5763, 5664

Table 5.2: List of α-emitters commonly used at ISS and their key properties.

In the simulations presented here, all sources are assumed to have the same activity and to emit isotropically. All detectors are also assumed to be in their optimal positions and configurations, as discussed in the previous sections. Figure 5.34 shows the energy spectra of the four source guns considered.

As shown in Fig. 5.35, the four α lines are distinctly visible in simulations of the typical PSD responses for both the silicon array (panel a) and the LUME detector (panel b). In these simulations, the silicon array is assumed, as a first

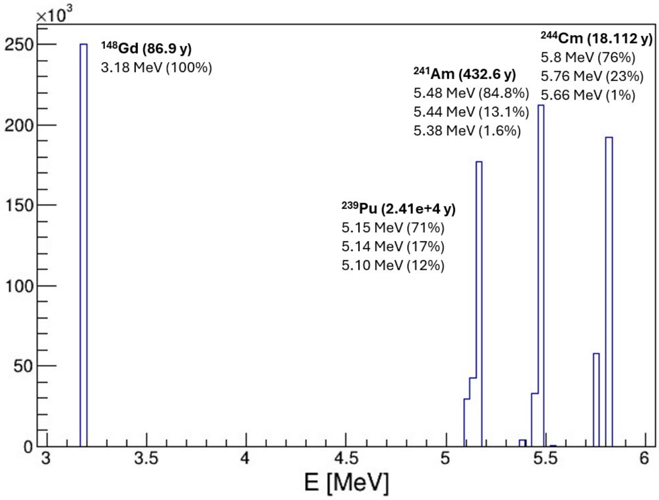

Figure 5.34: Energy spectrum of the four α-particle guns as generated by `ggland`, assumed in the simulations. For each source, the α-particle energies and their corresponding half-life are indicated. For simulation purposes, all four sources are assumed to have the same activity.

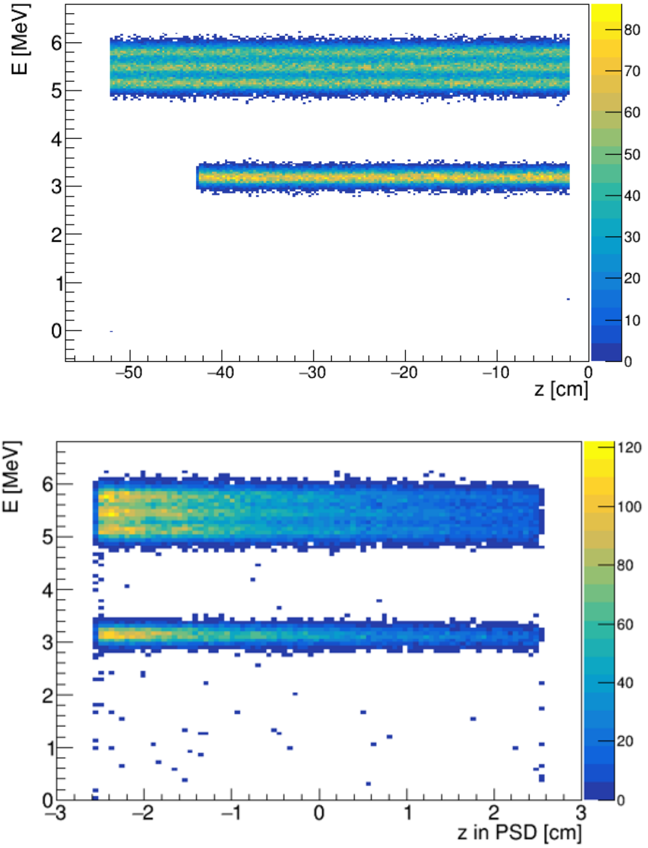

Figure 5.35: Simulation of typical PSD responses showing the four α lines for both the silicon array (panel a) and the LUME detector (panel b) assuming a resolution of 10 % of the deposited energy. The lower energy α particles from ^{148}Gd, observed in panel (a), can only travel a shorter distance along the $z-$axis and do not reach the far end of the silicon array, in contrast to the higher energy α particles.

approximation, to be a single cylindrical test volume with the same dimensions as the ISS silicon array. The only noticeable difference lies in the behavior of the silicon array. Specifically, the α particles from ^{148}Gd, due to their lower energy relative to the others, can only travel a shorter distance along the $z-$axis and do not reach the far end of the silicon array.

For the silicon array, an energy resolution of 10% of the deposited energy has been assumed. The PSD energy spectrum is shown in Fig. 5.36.

An energy resolution of 3.5% and a dead layer of 0.05 μm have been con-

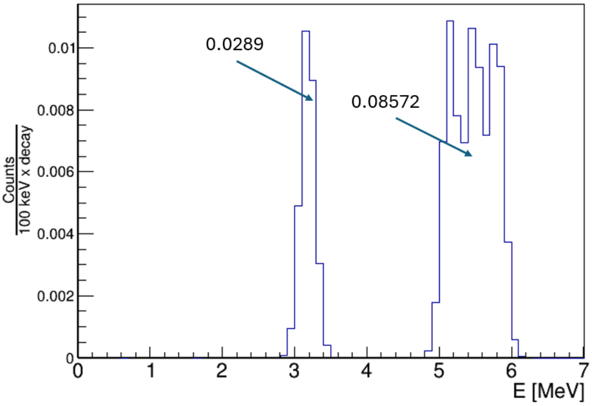

Figure 5.36: Simulated energy spectrum showing the distribution of energy for the detected α particles in the silicon array, assuming a resolution of 10 % of the deposited energy.

sidered for the CD-shaped DSSD. Fig. 5.37 presents its expected reconstructed energy spectra: the left panel shows the deposited energy, while the right panel displays the energy as a function of the ring index. As seen, the three highest-energy α particle lines are not fully resolved.

Fig. 5.38, on the other hand, shows the radial distribution and a contour plot in the (x, y) plane of the α particles hitting the ΔE layer of the fission fragment telescope. The same pattern would also be observed when examining the deposited energy as a function of the sector index.

The simulations of α-energy spectra for various detectors were performed to evaluate their response and energy resolution under conditions similar to those expected in the experiment. These simulations allow us to ensure the proper calibration of the detectors, which is critical for accurate data analysis. Specifically, using α sources with well-known energies provides a reliable means to establish a precise energy scale. The choice to use four α sources simultaneously stems from the need to have a sufficient number of calibration points across the energy range of interest. This approach ensures a more robust and accurate calibration, reducing uncertainties in the energy scale.

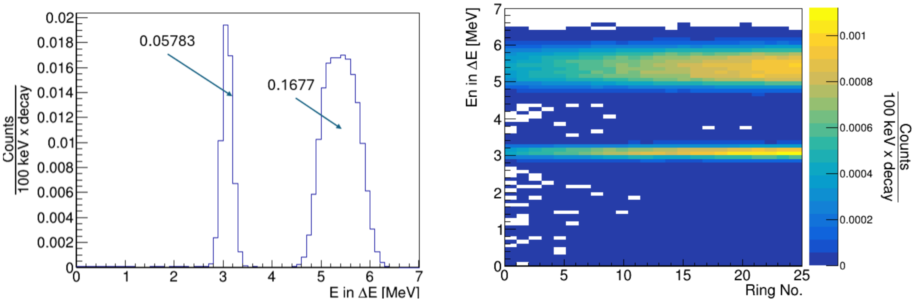

Figure 5.37: Simulated energy spectra for the CD-shape DSSD. In this case, an energy resolution of 3.5 % and a dead layer of 0.05 μm have been considered. The left panel shows the deposited energy, while the right panel presents the energy deposited per ring index. The three highest-energy α particle lines are observed but are not fully resolved in the spectrum.

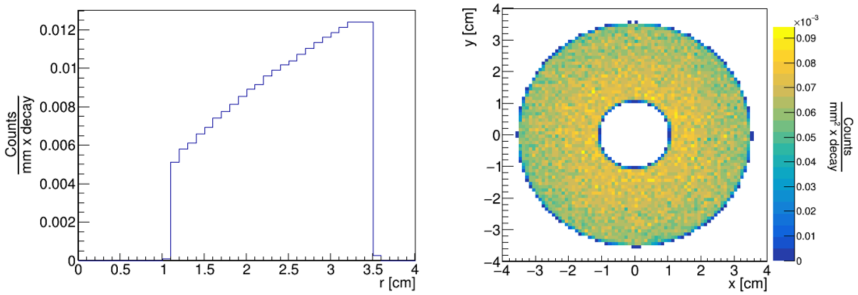

Figure 5.38: Left panel: Radial distribution of α particles on the CD-shaped DSSD. Right panel: Contour plot in the (x, y) plane of the α particles hitting the ΔE layer of the fission fragment telescope. The distribution is more homogeneous compared to that of the fission fragments shown in Fig. 5.14.

Chapter 6

Conclusion and outlook

The origin of the heaviest elements in the Universe remains one of the most intriguing questions in science. Recent observations of gravitational waves and electromagnetic radiation from neutron-star mergers have provided an unprecedented opportunity to address this question. However, understanding the astrophysical r-process, which is responsible for the creation of these elements, requires detailed knowledge of the underlying nuclear processes.

This thesis focused on the critical role of nuclear fission in the r-process, which constrains the formation of even heavier elements. Nuclear fission is an inherently complex process, posing a challenge for both experimental investigations and theoretical frameworks. This complexity arises primarily from the fact that its observables, such as the fission barrier, are heavily influenced by the intricate interplay between microscopic nuclear structure effects and the macroscopic properties of cold nuclear matter. While a substantial amount of data on unstable nuclei on the proton-rich side of the valley of beta stability is available in the literature, the same cannot be said for neutron-rich fissile nuclei. Only thanks to recent advances in the production of radioactive beams and spectrometer design the measurement of fission barrier heights in inverse kinematics becomes possible, thereby opening the doors to the study of previously inaccessible radioactive nuclei.

A novel approach for studying (d,pF) reactions using the ISOLDE Solenoidal Spectrometer at CERN was presented. Specifically designed to enhance the detection efficiency for fission fragments in coincidence with a proton from a (d,pF) reaction in the 2 T field of ISS, this approach allows for the extraction of fission probabilities of neutron-rich nuclei as a function of their excitation energy. Additionally, a dedicated measurement of γ-rays offers further insights into the total energy and multiplicity of γ-rays emitted during the fission process.

In Chapter 2, surrogate (d,p) reactions performed in inverse kinematics were introduced as an approach to investigate neutron-induced fission occurring in extreme astrophysical scenarios, such as neutron star mergers. The solenoidal spectrometer approach was presented as a solution to the experimental challenges associated with the inverse kinematics technique, including the kinematic compression and the kinematic shift. The innovative and compact experimental setup designed for the solenoidal spectrometer was described in detail in Chapter 3.

Chapter 4 outlined the motivations for selecting ^{230}Ac as candidate for a first measurement. This isotope was chosen based on its predicted fission barrier height, as well as the available beam intensities and the production capabilities of the facility.

In Chapter 5, detailed simulations of the detector responses were presented, with a particular focus on the position-sensitive silicon array for detecting backward-emitted protons, the off-axis silicon luminosity monitor, and the double-sided silicon strip detector system for fission fragment detection. Simulations have shown that a CD-shaped detector is well-suited for detecting fission fragments emitted in the forward direction with an angular distribution strongly forward-peaked in the laboratory frame due to the kinematic boost from inverse kinematics. This design achieves a detection efficiency that is eight times higher than that of the gas-filled fission fragment detectors used in a previous proof-of-principle ^{238}U(d,pF) experiment at ANL. An off-axis approach was chosen for the beam luminosity detector, as it is the optimal configuration to avoid interference with the trajectories of fission fragments. The simulations of this design demonstrated a significantly improved signal-to-background ratio compared to standard on-beam devices, due to the additional position information of the hits.

All the simulation results presented in this thesis have laid the foundation for designing and manufacturing the mechanical support structures for the various detectors. A key next step will be to assemble the mechanical components and integrate the entire experimental setup inside the solenoidal spectrometer, a task that will require collaborative effort. A crucial future step will be to carry out the experiment and evaluate whether the simulations accurately represent the actual experimental outcomes. The familiarity gained with the various detectors and the data acquisition system will be essential for performing the data analysis, extracting the fission barrier of ^{230}Ac, studying the emitted γ-rays during the fission process, and determining the mass distribution of the produced fission fragments. Ultimately, the goal will be to compare the experimental data with model predictions, providing insights into the fission process and its astrophysical implications.

The experiment proposal has been accepted by the ISOLDE Program Advisory Committee (INTC), and beam time has been requested for the summer of 2025. This will be the first experiment using a novel approach to investigate the fission of a short-lived isotope in inverse kinematics inside a solenoidal spectrometer, providing the first experimental determination of the fission barrier height of ^{230}Ac.

Appendix A

PACE4 fusion-evaporation simulations

In central collisions between nuclei at beam energies range below 15 MeV/u, the nuclei overlap significantly, leading to a large transfer of energy and angular momentum from their relative motion to internal degrees of freedom. This energy is distributed among many nucleons in the combined projectile-target system, with each nucleon gaining a moderate amount—generally insufficient for escape. However, these interactions produce an intermediate state known as the compound nucleus (CN), formed by the complete fusion of the colliding nuclei after absorbing the incident particle but before emitting any outgoing particles. Consequently, the mass and charge of the CN equal the sum of the original nuclei. Once energy and angular momentum equilibrate within the CN, it undergoes evaporation, losing excess energy by emitting light particles and gamma rays. The remaining nuclear fragment after this emission is called the evaporation residue (ER).

PACE4 (Projection Angular-momentum Coupled Evaporation) is a Monte Carlo-based statistical model used to simulate the evaporation of a compound nucleus. It can model the primary evaporation channels across different beam energies. The code computes the decay probabilities and widths for all nuclei involved in the decay chain [69]. This code has been employed to calculate the background expected from charged particles emitted in fusion-evaporation reactions between ^{229}Ac and ^{12}C in the target, for an incoming energy of 8 MeV/u.

The results from 10^6 (maximum number of events that can be simulated with PACE4) simulated events are presented below. The tables are organized as follows: Tab. A.1 reports the yields of the residual nuclei resulting from the compound nucleus decay, while Tab. A.2 provides the number per event and average energy of evaporated neutrons (n), protons (p), alpha particles, and gamma rays. Tabs. A.3 and A.4 present the energy and angular distributions in the Lab frame for the evaporated charged particles. The angular range detectable by the silicon array is highlighted in yellow. As it can be inferred from Tab. A.2, the number of fusion-evaporation events leading to the emission of light-charged particles represents less than 1 %. Each simulation requires less than 30 seconds to run.

Z	N	A		Events	%	Cross-section [mb]
95	139	234	Am	1	<0.001	0.00121
94	140	234	Pu	1	<0.001	0.00121
93	139	232	Np	4	<0.001	0.00486
92	140	232	U	1	<0.001	0.00121
91	139	230	Pa	1	<0.001	0.00121
Total fission				999992	99.9	1213.97
Total				1000000	100	1213.98

Table A.1: Yields of residual nuclei resulting from the decay of the compound nucleus formed in the ^{229}Ac at 8 MeV/u on ^{12}C reaction.

Ratio:	**n**	**p**	**alpha**	**gamma**
Total	1.42	0.002	0.004	0.0002
Average Energy [MeV]	3.4	12.0	22.5	7.3

Table A.2: Number per event and average energy of evaporated neutrons (n), protons (p), alpha particles, and gamma rays from the simulated ^{229}Ac at 8 MeV/u on ^{12}C reaction.

Energy [MeV]	**Angular range [deg]**					
	0 – 30	30 – 60	60 – 90	90 – 120	120 – 150	150 – 180
0 – 5	0	2	60	148	46	10
5 – 10	0	5	269	52	3	0
10 – 20	1	339	343	6	0	0
Above 20	536	688	20	0	0	0
Total	537	1034	692	206	49	10

Table A.3: Lab frame energy and angular distribution of the evaporated protons from the simulated ^{229}Ac at 8 MeV/u on ^{12}C reaction. The angular range detectable by the silicon array is highlighted in yellow.

A more complete overview of data in Table A.3 and Table A.4 are reported in Fig. A.1. These calculations suggest that the overwhelming majority of background events is not caused by fusion-evaporation reactions.

Energy [MeV]	**Angular range [deg]**					
	0 – 30	30 – 60	60 – 90	90 – 120	120 – 150	150 – 180
0 – 5	11	146	72	1	0	0
5 – 10	0	121	130	0	0	0
10 – 20	0	337	154	0	0	0
Above 20	1363	2153	22	0	0	0
Total	1374	2757	378	0	0	0

Table A.4: Lab frame and angular distribution of the evaporated α particles from the simulated ^{229}Ac at 8 MeV/u on ^{12}C reaction. The angular range detectable by the silicon array is highlighted in yellow.

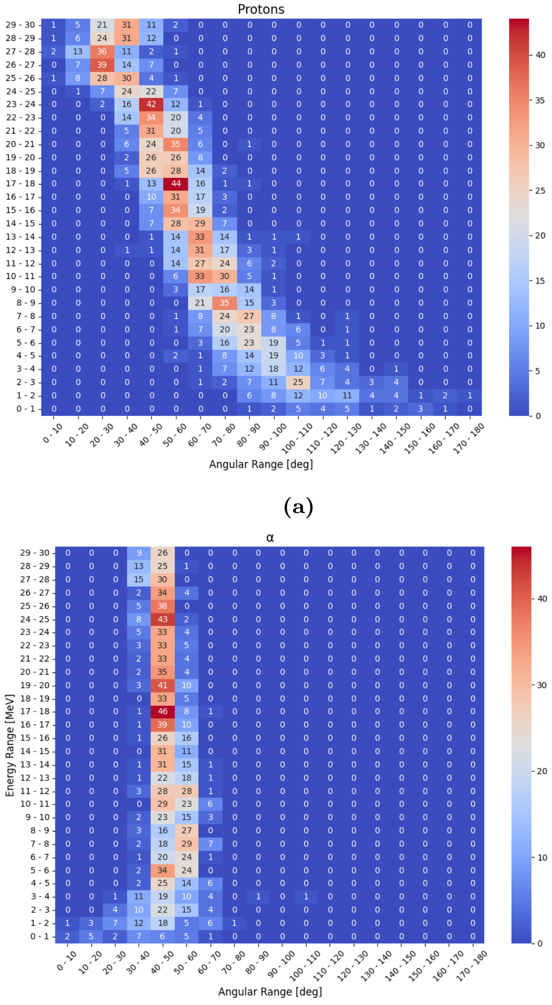

Protons

	0 - 10	10 - 20	20 - 30	30 - 40	40 - 50	50 - 60	60 - 70	70 - 80	80 - 90	90 - 100	100 - 110	110 - 120	120 - 130	130 - 140	140 - 150	150 - 160	160 - 170	170 - 180
29 - 30	1	5	21	31	11	2	0	0	0	0	0	0	0	0	0	0	0	0
28 - 29	1	6	24	31	12	0	0	0	0	0	0	0	0	0	0	0	0	0
27 - 28	2	13	36	11	2	1	0	0	0	0	0	0	0	0	0	0	0	0
26 - 27	0	7	39	14	7	0	0	0	0	0	0	0	0	0	0	0	0	0
25 - 26	1	8	28	30	4	1	0	0	0	0	0	0	0	0	0	0	0	0
24 - 25	0	1	7	24	22	7	0	0	0	0	0	0	0	0	0	0	0	0
23 - 24	0	0	2	16	42	12	1	0	0	0	0	0	0	0	0	0	0	0
22 - 23	0	0	0	14	34	20	4	0	0	0	0	0	0	0	0	0	0	0
21 - 22	0	0	0	5	31	20	5	0	0	0	0	0	0	0	0	0	0	0
20 - 21	0	0	0	6	24	35	6	0	1	0	0	0	0	0	0	0	0	0
19 - 20	0	0	0	2	26	26	8	0	0	0	0	0	0	0	0	0	0	0
18 - 19	0	0	0	5	26	28	14	2	0	0	0	0	0	0	0	0	0	0
17 - 18	0	0	0	1	13	44	16	1	1	0	0	0	0	0	0	0	0	0
16 - 17	0	0	0	0	10	31	17	3	0	0	0	0	0	0	0	0	0	0
15 - 16	0	0	0	0	7	34	19	2	0	0	0	0	0	0	0	0	0	0
14 - 15	0	0	0	0	7	28	29	7	0	0	0	0	0	0	0	0	0	0
13 - 14	0	0	0	0	1	14	33	14	1	1	1	0	0	0	0	0	0	0
12 - 13	0	0	0	1	1	14	31	17	3	1	0	0	0	0	0	0	0	0
11 - 12	0	0	0	0	0	14	27	24	6	2	0	0	0	0	0	0	0	0
10 - 11	0	0	0	0	0	6	33	30	5	1	0	0	0	0	0	0	0	0
9 - 10	0	0	0	0	0	3	17	16	14	1	0	0	0	0	0	0	0	0
8 - 9	0	0	0	0	0	0	21	35	15	3	0	0	0	0	0	0	0	0
7 - 8	0	0	0	0	0	1	8	24	27	8	1	0	1	0	0	0	0	0
6 - 7	0	0	0	0	0	1	7	20	23	8	6	0	1	0	0	0	0	0
5 - 6	0	0	0	0	0	0	3	16	23	19	5	1	1	0	0	0	0	0
4 - 5	0	0	0	0	0	2	1	8	14	19	10	3	1	0	0	0	0	0
3 - 4	0	0	0	0	0	0	1	7	12	18	12	6	4	0	1	0	0	0
2 - 3	0	0	0	0	0	0	1	2	7	11	25	7	4	3	4	0	0	0
1 - 2	0	0	0	0	0	0	0	0	6	8	12	10	11	4	4	1	2	1
0 - 1	0	0	0	0	0	0	0	0	1	2	5	4	5	1	2	3	1	0

(a)

α

	0 - 10	10 - 20	20 - 30	30 - 40	40 - 50	50 - 60	60 - 70	70 - 80	80 - 90	90 - 100	100 - 110	110 - 120	120 - 130	130 - 140	140 - 150	150 - 160	160 - 170	170 - 180
29 - 30	0	0	0	9	26	0	0	0	0	0	0	0	0	0	0	0	0	0
28 - 29	0	0	0	13	25	1	0	0	0	0	0	0	0	0	0	0	0	0
27 - 28	0	0	0	15	30	0	0	0	0	0	0	0	0	0	0	0	0	0
26 - 27	0	0	0	2	34	4	0	0	0	0	0	0	0	0	0	0	0	0
25 - 26	0	0	0	5	38	0	0	0	0	0	0	0	0	0	0	0	0	0
24 - 25	0	0	0	8	43	2	0	0	0	0	0	0	0	0	0	0	0	0
23 - 24	0	0	0	5	33	4	0	0	0	0	0	0	0	0	0	0	0	0
22 - 23	0	0	0	3	33	5	0	0	0	0	0	0	0	0	0	0	0	0
21 - 22	0	0	0	2	33	4	0	0	0	0	0	0	0	0	0	0	0	0
20 - 21	0	0	0	2	35	4	0	0	0	0	0	0	0	0	0	0	0	0
19 - 20	0	0	0	3	41	10	0	0	0	0	0	0	0	0	0	0	0	0
18 - 19	0	0	0	0	33	5	0	0	0	0	0	0	0	0	0	0	0	0
17 - 18	0	0	0	1	46	8	1	0	0	0	0	0	0	0	0	0	0	0
16 - 17	0	0	0	1	39	10	0	0	0	0	0	0	0	0	0	0	0	0
15 - 16	0	0	0	1	26	16	0	0	0	0	0	0	0	0	0	0	0	0
14 - 15	0	0	0	0	31	11	0	0	0	0	0	0	0	0	0	0	0	0
13 - 14	0	0	0	1	31	15	1	0	0	0	0	0	0	0	0	0	0	0
12 - 13	0	0	0	1	22	18	1	0	0	0	0	0	0	0	0	0	0	0
11 - 12	0	0	0	3	28	28	1	0	0	0	0	0	0	0	0	0	0	0
10 - 11	0	0	0	0	29	23	6	0	0	0	0	0	0	0	0	0	0	0
9 - 10	0	0	0	2	23	15	3	0	0	0	0	0	0	0	0	0	0	0
8 - 9	0	0	0	3	16	27	0	0	0	0	0	0	0	0	0	0	0	0
7 - 8	0	0	0	2	18	29	7	0	0	0	0	0	0	0	0	0	0	0
6 - 7	0	0	0	1	20	24	1	0	0	0	0	0	0	0	0	0	0	0
5 - 6	0	0	0	2	34	24	0	0	0	0	0	0	0	0	0	0	0	0
4 - 5	0	0	0	2	25	14	6	0	0	0	0	0	0	0	0	0	0	0
3 - 4	0	0	1	11	19	10	4	0	1	0	1	0	0	0	0	0	0	0
2 - 3	0	0	4	10	22	15	4	0	0	0	0	0	0	0	0	0	0	0
1 - 2	1	3	7	12	18	5	6	1	0	0	0	0	0	0	0	0	0	0
0 - 1	2	5	2	7	6	5	1	0	0	0	0	0	0	0	0	0	0	0

(b)

Figure A.1: Panel a) Heatmap illustrating the distribution of angular ranges versus energy for protons emitted during the evaporation of the compound nucleus (CN) formed by an ^{229}Ac beam at 8 MeV/u impinging on a ^{12}C target. Panel b) Heatmap illustrating the distribution of angular ranges versus energy for α particles from the same reaction.

Appendix B

Proton angular distributions

In this Appendix, an overview of the `PTOLEMY`-calculated cross-section for proton emission as a function of the scattering angle in both the center-of-mass frame and the laboratory reference frame is presented in Fig. B.1 and Fig. B.2, respectively. All single-particle orbitals populated in the compound nucleus are represented, and identified by the quantum numbers n, j, and l, which correspond to the principal quantum number, total angular momentum, and orbital angular momentum, respectively.

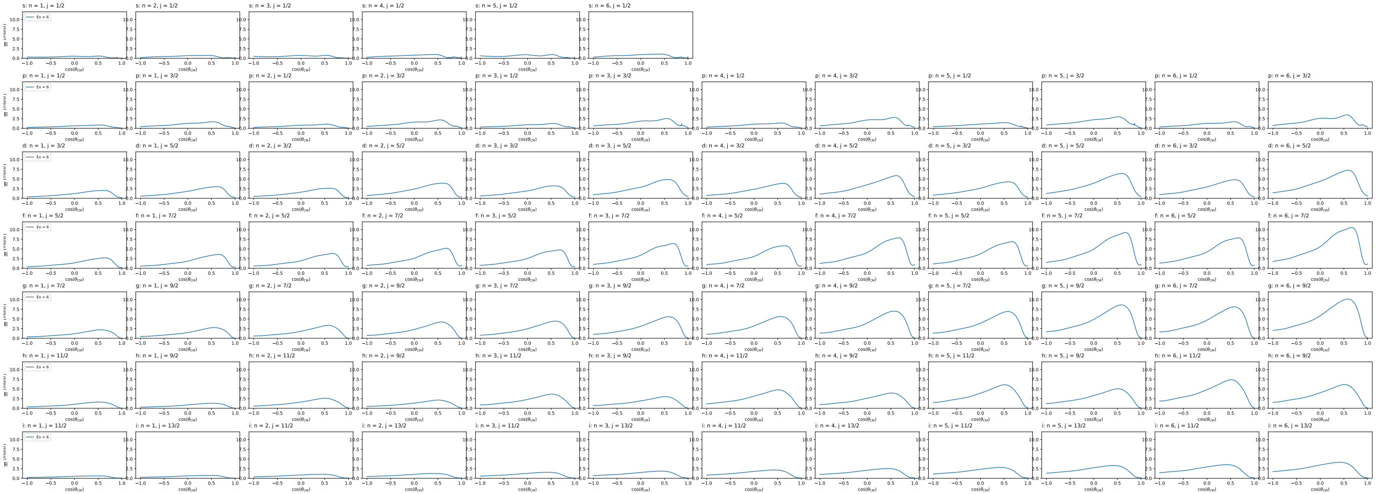

Figure B.1: Overview of `PTOLEMY`-calculated cross-sections for proton emission as a function of the scattering angle in the center-of-mass frame, following the ^{229}Ac(d,p) reaction at 8 MeV/u, for different single-particle orbitals populated in ^{230}Ac. Since the angular distribution in the CM frame is independent of excitation energy, only the case with an excitation energy of 6 MeV is shown.

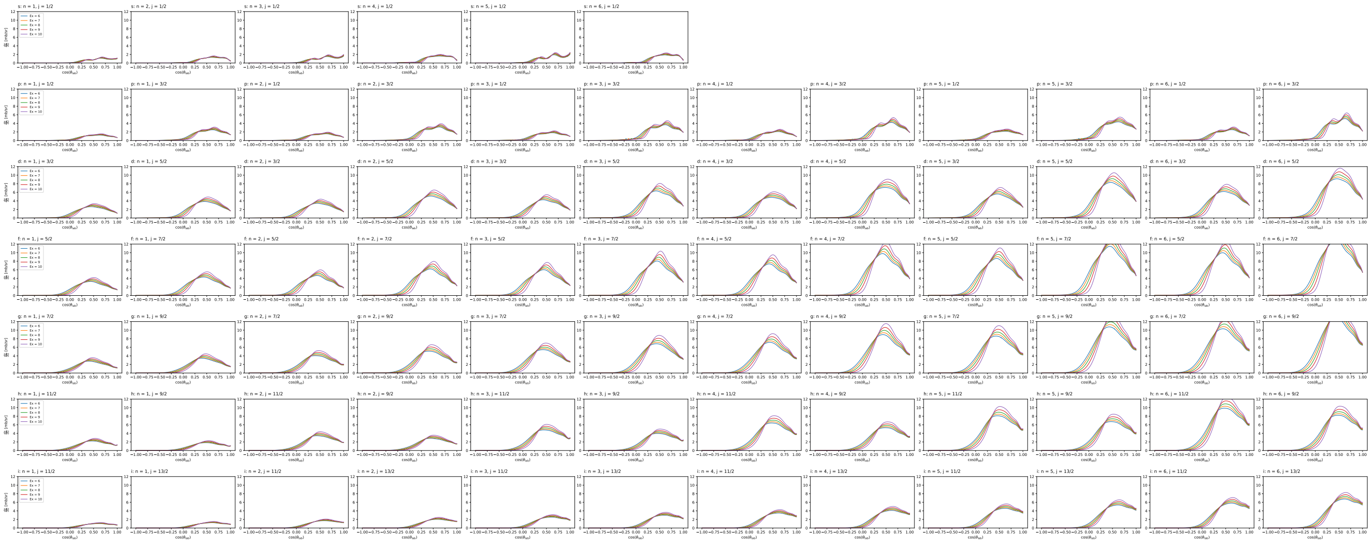

Figure B.2: Overview of `PTOLEMY`-calculated cross-sections for proton emission as a function of the scattering angle in the laboratory frame, following the ^{229}Ac(d,p) reaction at 8 MeV/u, for different single-particle orbitals populated in ^{230}Ac. Different excitation energies of the compound nucleus are considered for each orbital.

Bibliography

[1] J. Lippuner, (2024).

[2] S. A. Bennett, K. Garrett, D. K. Sharp, S. J. Freeman, A. G. Smith, T. J. Wright, B. P. Kay, T. L. Tang, I. A. Tolstukhin, Y. Ayyad, J. Chen, P. J. Davies, A. Dolan, L. P. Gaffney, A. Heinz, C. R. Hoffman, C. Müller-Gatermann, R. D. Page, and G. L. Wilson, "Direct Determination of Fission-Barrier Heights Using Light-Ion Transfer in Inverse Kinematics", Phys. Rev. Lett. **130** (2023).

[3] E. Jochen, N. Birge, M. Kortelainen, W. Nazarewicz, E. Olsen, A. M. Perhac, and M. Stoitsov, "The limits of the nuclear landscape", Nature **486**, 509–512 (2012).

[4] J. A. Johnson, "Populating the periodic table: Nucleosynthesis of the elements", Science **363**, 474–478 (2019).

[5] Editors of Encyclopaedia Britannica, *nuclear binding energy*, Encyclopedia Britannica, (2023, April 10) `https://www.britannica.com/science/nuclear-binding-energy`.

[6] E. M. Burbidge, G. R. Burbidge, W. A. Fowler, and F. Hoyle, "Synthesis of the Elements in Stars", Rev. Mod. Phys. **29**, 547–650 (1957).

[7] A. G. W. Cameron, "Stellar Evolution, Nuclear Astrophysics, and Nucleogenesis", Tech. Rep. CRL-41 (Atomic Energy of Canada) (1957).

[8] Particle Data Group, *Review of particle physics*, (2024) `https://pdg.lbl.gov`.

[9] C. Sneden, J. J. Cowan, J. E. Lawler, I. I. Ivans, S. Burles, T. C. Beers, F. Primas, V. Hill, J. W. Truran, G. M. Fuller, B. Pfeiffer, and K.-L. Kratz, "The Extremely Metal-Poor, Neutron-Capture-rich Star CS 22892-052: A Comprehensive Abundance Analysis.", The Astrophysical Journal **591**, 936–953 (2003).

[10] C. J. Horowitz, A. Arcones, B. Côté, I. Dillmann, W. Nazarewicz, I. U. Roederer, H. Schatz, A. Aprahamian, D. Atanasov, A. Bauswein, T. C. Beers, J. Bliss, M. Brodeur, J. A. Clark, A. Frebel, F. Foucart, C. J. Hansen, O. Just, A. Kankainen, G. C. McLaughlin, J. M. Kelly, S. N. Liddick, D. M. Lee, J. Lippuner, D. Martin, J. Mendoza-Temis, B. D. Metzger, M. R. Mumpower, G. Perdikakis, J. Pereira, B. W. O'Shea, R. Reifarth, A. M. Rogers, D. M. Siegel, A. Spyrou, R. Surman, X. Tang, T. Uesaka, and M. Wang, "r-process nucleosynthesis: connecting rare-isotope beam facilities with the cosmos", J. Phys. G: Nucl. Part. Phys. **46**, 083001, (2019).

[11] B. P. Abbott, et al. (LIGO Scientific Collaboration, and V. Collaboration), "Observation of Gravitational Waves from a Binary Black Hole Merger", Physical Review Letters **116**, 061102 (2016).

[12] D. Watson, C. J. Hansen, J. Selsing, A. Koch, D. B. Malesani, A. C. Andersen, J. P. U. Fynbo, A. Arcones, A. Bauswein, S. Covino, A. Grado, K. E. Heintz, L. Hunt, C. Kouveliotou, G. Leloudas, A. J. Levan, P. Mazzali, and E. Pian, "Identification of strontium in the merger of two neutron stars", Nature **574**, 497–500 (2019).

[13] O. Hahn and F. Strassmann, "Über den nachweis und das verhalten der bei der bestrahlung des urans mittels neutronen entstehenden erdalkalimetalle", Reine Und Technisch Angewandte Chemie **27**, 11–15 (1939).

[14] N. Bohr and J. A. Wheeler, "The Mechanism of Nuclear Fission", Phys. Rev. **56**, 426–450 (1939).

[15] A. N. Andreyev, K. Nishio, and K.-H. Schmidt, "Nuclear fission: a review of experimental advances and phenomenology", Rep. Prog. Phys. **81** (2018).

[16] M. Brack and P. Quentin, "The Strutinsky method and its foundation from the Hartree-Fock-Bogoliubov approximation at finite temperature", Nuclear Physics A **361**, 35–82 (1981).

[17] A. Obertelli and H. Sagawa, *Modern Nuclear Physics*, UNITEXT for Physics (Springer, 2021).

[18] W. Younes and W. D. Loveland, *An Introduction to Nuclear Fission*, Graduate Texts in Physics (Springer, 2021).

[19] J. Cramer and H. Britt, "Neutron Fission Cross Sections for ^{231}Th, ^{233}Th, ^{235}U, ^{237}U, ^{239}U, ^{241}Pu, and ^{243}Pu from 0.5 to 2.25 MeV using (t, pf) Reactions", Nucl. Sci. Eng. **41**, 177–187 (1970).

[20] G. Kessedjan, B. Jurado, M. Aiche, G. Barreau, A. Bidaud, S. Czajkowski, D. Dassié, B. Haas, L. Mathieu, L. Audouin, N. Capellan, L. Tassan-Got, J. N. Wilson, E. Berthoumieux, F. Gunsing, C. Theisen, O. Serot, E. Bauge, I. Ahmad, J. Greene, and R. Janssens, "Neutron-induced fission cross sections of short-lived actinides with the surrogate reaction method", Phys. Lett. B **692**, 297–301 (2010).

[21] E. Kugler, "The ISOLDE facility", Hyp. Int. **129**, 23–42 (2000).

[22] The ISOLDE Collaboration, *The ISOLDE Facility*, (2024) `https://isolde.cern/isolde-facility`.

[23] E. Lopienska, *The CERN accelerator complex, layout in 2022*, CERN-GRAPHICS-2022-001, (2022) `https://cds.cern.ch/record/2800984`.

[24] E. J. A. Bouquerel, "Atomic Beam Merging and Suppression of Alkali Contaminants in Multi Body High Power Targets: Design and Test of Target and Ion Source Prototypes at ISOLDE", PhD thesis (Université Paris XI Orsay, 2009).

[25] E. Kugler, D. Fiander, B. Jonson, H. Haas, A. Przewloka, H. L. Ravn, D. J. Simon, and K. Zimmer, "The new CERN ISOLDE on-line mass-separator facility at the PS-Booster", Nucl. Instrum. Methods Phys. Res. Sect. B **70**, 41–49 (1992).

[26] The ISOLDE Collaboration, *Targets and Separators*, (2024) `https://isolde.cern/targets-and-separators`.

[27] C. Porzio, *Private communication.*

[28] P. Van Duppen and K. Riisager, "Physics with REX-ISOLDE: from experiment to facility", J. Phys. G: Nuck. Part. Phys. **38** (2011).

[29] D. Habs, O. Kester, G. Bollen, L. Liljeby, K. G. Rensfelt, D. Schwalm, R. von Han, G. Walter, P. Van Duppen, and REX-ISOLDE collaboration, "The REX-ISOLDE project", Nucl. Phys. A. **616**, 29–38 (1997).

[30] L. Williams, A. Bouzoud, N. Delruelle, J. C. Gayde, Y. Leclercq, M. Pasini, J. P. Tock, and G. Vandoni, "Design of the High Beta Cryomodule for the HIE-ISOLDE Upgrade at CERN.", CERN-ATS-2011-247 (2011).

[31] M. J. G. Borge and K. Riisager, "HIE-ISOLDE, the project and the physics opportunities", Eur. Phys. J. A. **52** (2016).

[32] M. Marie-Jeanne, "Investigation of the performances of an ECR charge breeder at ISOLDE: a study of the 1+ n+ scenario for the next generation ISOL facilities", Ecole Doctorale de Physique, PhD thesis (Universitè Joseph Fourier - Grenoble I, Grenoble, 2010).

[33] Y. Kadi, Y. Blumenfeld, W. Venturini Delsolaro, M. A. Fraser, M. Huyse, A. Papageorgiou Koufidou, J. A. Rodriguez, and F. Wenander, "Post-accelerated beams at ISOLDE", J. Phys. G: Nucl. Part. Phys. **44** (2017).

[34] B. P. Kay, M. Alcorta, B. B. Back, S. I. Baker, S. Bedoor, T. Bloxham, J. A. Clark, C. M. Deibel, S. J. Freeman, C. R. Hoffman, A. M. Howard, J. C. Lighthall, S. T. Marley, A. J. Mitchell, K. E. Rehm, J. P. Schiffer, D. K. Sharp, D. V. Shetty, J. S. Thomas, A. H. Wuosmaa, and S. Zhu, "HELIOS - progress and possibilities", Journal of Physics: Conference Series **381** (2012).

[35] S. J. Freeman, "Transfer Reactions with Solenoidal Spectrometers", Acta Physica Polonica B **16** (2023).

[36] J. P. Schiffer, "Proceedings of the Workshop on Experimental Equipment for an Advanced ISOL Facility", in Lawrence Berkeley National Laboratory, Vol. LBNL-42138, edited by I. Y. Lee (1998), pp. 667–678.

[37] A. H. Wuosmaa, T. Al Tahtamouni, and J. P. Schiffer, "A solenoidal transport device for transfer reactions in inverse kinematics", Nucl. Phys. A. **746**, 267–271 (2004).

[38] A. H. Wuosmaa, J. P. Schiffer, B. B. Back, C. J. Lister, and K. E. Rehm, "A solenoidal spectrometer for reactions in inverse kinematics", Nucl. Instr. and Meth. A. **580**, 1290–1300 (2007).

[39] A. Kawęcka and M. V. Managlia, "Solenoidal spectrometers: HELIOS and ISS. Study of Nuclear Reactions in Inverse Kinematics", Unpublished, 2022.

[40] J. N. Wilson, D. Thisse, M. Lebois, N. Jovančević, D. Gjestvang, R. Canavan, M. Rudigier, D. Étasse, R.-B. Gerst, L. Gaudefroy, E. Adamska, P. Adsley, A. Algora, M. Babo, K. Belvedere, J. Benito, G. Benzoni, A. Blazhev, A. Boso, S. Bottoni, M. Bunce, R. Chakma, N. Cieplicka-Oryńczak, S. Courtin, M. L. Cortés, P. Davies, C. Delafosse, M. Fallot, B. Fornal, L. Fraile, A. Gottardo, V. Guadilla, G. Häfner, K. Hauschild, M. Heine, C. Henrich, I. Homm, F. Ibrahim, W. Iskra, P. Ivanov, S. Jazrawi, A. Korgul, P. Koseoglou, T. Kröll, T. Kurtukian-Nieto, L. L. Meur, S. Leoni, J. Ljungvall, A. Lopez-Martens, R. Lozeva, I. Matea, K. Miernik, J. Nemer, S. Oberstedt, W. Paulsen, M. Piersa, Y. Popovitch, C. Porzio, L. Qi, D. Ralet, P. H. Regan, K. Rezynkina, V. Sánchez-Tembleque, S. Siem, C. Schmitt, P.-A. Söderström, C. Sürder, G. Tocabens, V. Vedia, D. Verney, N. Warr, B. Wasilewska, J. Wiederhold, M. Yavahchova, F. Zeiser, and S. Ziliani, "Angular momentum generation in nuclear fission", Nature **590**, 566–570 (2021).

[41] H. T. Törnqvist, *Private communication.*

[42] The ISOLDE Collaboration, *Si-detector array*, (2024) `https://isolde-solenoidal-spectrometer.web.cern.ch/setup/si-detector-array`.

[43] Micron Semiconductor Ltd., *S3*, (2024) `https://www.micronsemiconductor.co.uk/product/s3/`.

[44] G. F. Knoll, *Radiation detection and measurement*, 4th ed. (John Wiley & Sons, 2010).

[45] O. Poleshchuk, R. Raabe, S. Ceruti, A. Ceulemans, H. D. Witte, T. Marchi, A. Mentana, J. Refsgaard, and J. Yang, “The SpecMAT active target”, Nucl. Instrum. Methods Phy. Res. Sect. A **1015** (2021).

[46] B. P. Kay, *Private communication.*

[47] D+T Microelectrónica, A.I.E., (2024) `https://www.dtm.es/`.

[48] ORTEC, *Si charged particle radiation detectors for research applications*, (2020) `https://www.ortec-online.com/products/radiation-detectors/silicon-charged-particle-radiation-detectors/si-charged-particle-radiation-detectors-for-research-applications`.

[49] P. T. MacGregor, “Single-Particle Structure of ^{29}Mg on the Approach to the $N = 20$ Island of Inversion”, PhD thesis (University of Manchester, 2021).

[50] K.-H. Schmidt, B. Jurado, C. Amouroux, and C. Schmitt, “General Description of Fission Observables: GEF Model Code”, Nucl. Data Sheets **131**, 107–221 (2016).

[51] M. Kowal and J. Skalski, “The Fission Barrier of Heaviest Nuclei from a Macroscopic-Microscopic Perspective”, in *Handbook of nuclear physics* (Springer Nature Singapore, Singapore, 2023), pp. 945–982.

[52] A. V. Karpov, W. J. Swiatecki, and K.-H. Schmidt, “On the topographical properties of fission barriers”, J. Phys. G: Nucl. Part. Phys. **35** (2008).

[53] S. Ebata, S. Okumura, C. Ishizuka, and S. Chiba, “Charge polarization calculated with a microscopic model for the fission fragments of U-236”, EPJ Web of Conferences **284** (2023).

[54] H. Nifenecker, “A dynamical treatment of isobaric widths in fission: an example of frozen quantal fluctuations”, J. Physique Lett. **41** (1980).

[55] K.-H. Schmidt and B. Jurado, “Final excitation energy of fission fragments”, Phys. Rev. C. **83** (2011).

[56] B. Jurado and K.-H. Schmidt, “Influence of complete energy sorting on the characteristics of the odd–even effect in fission-fragment element distributions”, J. Phys. G: Nucl. Part. Phys. **42** (2015).

[57] M. Au, *Private communication.*

[58] A. Kawęcka, M. V. Managlia, A. Heinz, H. T. Johansson, H. Törnqvist, D. K. Sharp, A. G. Smith, T. Wright, M. Au, F. Browne, P. A. Butler, A. Camaiani, A. Ceulemans, D. J. Clarke, A. J. Dolan, S. J. Freeman, L. P. Gaffney, S. A. Giuliani, B. R. Jones, B. Jonson, B. P. Kay, J. Klimo, M. Labiche, I. Lazarus, P. T. MacGregor, B. Marsh, T. Nilsson, J. Ojala, B. Olaizola, R. D. Page, G. Martínez-Pinedo, and O. Poles, *Fission of ^{230}Ac*, Proposal to the ISOLDE and Neutron Time-of-Flight Committee (Following HIE-ISOLDE Letter of Intent I-224) I-224 (European Organization for Nuclear Research, 2023).

[59] Y. Shuanggui, Y. Weifan, X. Yanbing, P. Qiangyan, X. Bing, H. Jianjun, W. Dong, L. Yingjun, M. Taotao, and Y. Zhenguo, “Search for β-delayed fission of the heavy neutron-rich isotope ^{230}Ac”, The European Physical Journal A - Hadrons and Nucle **10**, 1–3 (2001).

[60] E.-M. Eckert, A. Kühmichel, J. Pochodzalla, K. D. Hildenbrand, U. Lynen, W. F. J. Müller, H. J. Rabe, H. Sann, H. Stelzer, W. Trautmann, R. Trockel, R. Wada, C. Cerruti, P. Lhénoret, R. Lucas, C. Mazur, C. Ng, M. Ribrag, E. Tomasi, A. Demeyer, and D. Guinet, “Transient times of fission in $^{40}\mathrm{Ar} +^{232}$ Th peripheral collisions”, Phys. Rev. Lett. **64**, 2483–2486 (1990).

[61] H. T. Johansson, *Ggland - Command-Line Simulation Wrapper*, (2013) `https://fy.chalmers.se/~f96hajo/ggland/ggland_doc.pdf`.

[62] CERN Application Software Group, *GEANT3: detector description and simulation tool*, CERN-W5013, Accessed: 2024-11-22, CERN (Geneva, Switzerland, 1994).

[63] S. Agostinelli, J. Allison, K. Amako, J. Apostolakis, H. Araujo, P. Arce, M. Asai, D. Axen, S. Banerjee, G. Barrand, F. Behner, L. Bellagamba, J. Boudreau, L. Broglia, A. Brunengo, H. Burkhardt, S. Chauvie, J. Chuma, R. Chytracek, G. Cooperman, G. Cosmo, P. Degtyarenko, A. Dell’Acqua, G. Depaola, D. Dietrich, R. Enami, A. Feliciello, C. Ferguson, H. Fesefeldt, G. Folger, F. Foppiano, A. Forti, S. Garelli, S. Giani, R. Giannitrapani, D. Gibin, J. Gómez Cadenas, I. González, G. Gracia Abril, G. Greeniaus, W. Greiner, V. Grichine, A. Grossheim, S. Guatelli, P. Gumplinger, R. Hamatsu, K. Hashimoto, H. Hasui, A. Heikkinen, A. Howard, V. Ivanchenko, A. Johnson, F. Jones, J. Kallenbach, N. Kanaya, M. Kawabata, Y. Kawabata, M. Kawaguti, S. Kelner, P. Kent, A. Kimura, T. Kodama, R. Kokoulin, M. Kossov, H. Kurashige, E. Lamanna, T. Lampén, V. Lara, V. Lefebure, F. Lei, M. Liendl, W. Lockman, F. Longo, S. Magni, M. Maire, E. Medernach, K. Minamimoto, P. Mora de Freitas, Y. Morita, K. Murakami, M. Nagamatu, R. Nartallo, P. Nieminen, T. Nishimura, K. Ohtsubo, M. Okamura, S. O’Neale, Y. Oohata, K. Paech, J. Perl, A. Pfeiffer, M. Pia, F. Ranjard, A. Rybin, S. Sadilov, E. Di Salvo, G.

Santin, T. Sasaki, N. Savvas, Y. Sawada, S. Scherer, S. Sei, V. Sirotenko, D. Smith, N. Starkov, H. Stoecker, J. Sulkimo, M. Takahata, S. Tanaka, E. Tcherniaev, E. S. Tehrani, M. Tropeano, P. Truscott, H. Uno, L. Urban, P. Urban, M. Verderi, A. Walkden, W. Wander, H. Weber, J. Wellisch, T. Wenaus, D. Williams, D. Wright, T. Yamada, H. Yoshida, and D. Zschiesche, “GEANT4: A Simulation Toolkit”, Nuclear Instruments and Methods in Physics Research A **506**, 250–303 (2003).

[64] M. H. Macfarlane and S. C. Pieper, “Ptolemy: a program for heavy-ion direct-reaction calculations”, unpublished.

[65] J. C. Lighthall, B. B. Back, S. I. Baker, S. J. Freeman, H. Y. Lee, B. P. Kay, S. T. Marley, K. E. Rehm, J. E. Rohrer, J. P. Schiffer, D. V. Shetty, A. W. Vann, J. R. Winkelbauer, and A. H. Wuosmaa, “Commissioning of the HELIOS spectrometer”, Nucl. Instrum. and Methods in Phys. Res. Sec. A **622**, 66–106 (2010).

[66] T. Wright, D. K. Sharp, M. Au, S. A. Bennett, P. A. Butler, A. Camaiani, S. J. Freeman, L. P. Gaffney, K. Garrett, S. A. Giuliani, A. Heinz, H. T. Johansson, B. Jonson, B. P. Kay, J. Klimo, M. Kowalska, M. Labiche, I. Lazarus, B. Marsh, T. Nilsson, B. Olaizola, R. D. Page, G. Martínez-Pinedo, R. Raabe, B. Reich, A. Rodriguez, S. Rothe, A. G. Smith, and A. Youssef, *Letter of Intent to the ISOLDE and Neutron Time-of-Flight Committee: Fission properties probed via measurements of transfer-induced fission with actinide beams in inverse kinematics using the ISOLDE Solenoidal Spectrometer*, Letter of Intent, 2021.

[67] A. J. Koning and S. Hilaire, “FRESCO: A Code for the Analysis of Nucleon and Photon Induced Reactions”, Computer Physics Communications **167**, 104–115 (2004).

[68] D. C. Radford and C. J. Chiara, *LISE++: A New Version of the LISE Code*, (2016) `https://lise.frib.msu.edu/lise.html`.

[69] A. Gavron, “Statistical model calculations in heavy ion reactions”, Physical Review C **21**, 230–236 (1980).